1988

Progress Report No. 24

Biomedical Computer Laboratory

PROGRESS REPORT

No. 24

1 July 1987 - 30 June 1988

Biomedical Computer Laboratory

Institute for Biomedical Computing

Washington University

700 South Euclid Ave.

St. Louis, Missouri 63110

BIOMEDICAL COMPUTER LABORATORY

INSTITUTE FOR BIOMEDICAL COMPUTING

WASHINGTON UNIVERSITY

PROGRESS REPORT NO. 24

JULY 1, 1987 - JUNE 30, 1988

TABLE OF CONTENTS

I. INTRODUCTION

This progress report from the Biomedical Computer Laboratory (BCL) summarizes activities during the period from July 1, 1987 through June 30, 1988. The Biomedical Computer Laboratory collaborates with research investigators throughout the Washington University School of Medicine and its affiliated hospitals in the application of advanced computer techniques to problems in biology and medicine. This often requires work in areas stretching from basic biomedical sciences through mathematical models to equipment design. Our orientation is interdisciplinary with the recognition that effective communication for workers with differing backgrounds comes only through extended collaboration and mutual respect.

The vigorous development and evolution of specialized hardware and software systems for use in the solution of research and clinical problems has continued to be the central focus of BCL activities. Several systems now in clinical use have seen a progression from exploratory pilot studies, to major developmental project, to local clinical trial, to clinical trials in multiple locations, to public availability through commercial manufacture. Perseverance in this sometimes tedious chain of development has found reward in the effective fielding of specialized computer systems to the medical community.

One class of computer applications requires strong coupling of the computer to its environment for digital signal processing. These applications typically involve the use of commercially available minicomputers and microprocessors in conjunction with specialized hardware designed and built locally. We have pursued many such applications by bringing signals from hospital wards and research laboratories to BCL by means of either analog or digital tape recordings or telephone lines and, more frequently, by taking the computers to the investigator's laboratory or the patient's bedside. More recently, an emphasis at BCL has been on the development of a flexible digital communication capability for linking data sources and information destinations with research-oriented computational resources at BCL as well as at collaborators' sites.

Of particular importance to current and future BCL projects is the development, in a closely related sister lab (Computer Systems Laboratory, or CSL), of a capability for the design and fabrication of custom very-large-scale integrated (VLSI) circuits. The realization of such circuits through collaboration with CSL is already opening up new opportunities for solving problems intractable with conventional computing devices. The CSL has as its goal the development of innovative approaches to computing that will have important implications for medicine and biology in the future.

For those classes of applications dominated by information processing requirements, available arrangements have matured from telephone lines linking our minicomputers to the large IBM Systems at the Washington University Computing Facilities, through development and support of a minicomputer based MUMPS system, to the establishment of independent groups such as the Medical Computing Facility and the Medical Computing Service Group which serve the local medical complex. Diverse needs continue to be met by these various options as well as by an increasing number of independent computing facilities within medical school departments.

Still another class of applications requires extensive use of large-scale computational services. Many investigators are assisted in their research through the use of generalized numerical, non-numerical, and statistical routines. Such work is sometimes carried out by staff members of BCL, but primarily by members of the Division of Biostatistics under the direction of Dr. Dabeeru C. Rao, and the University Computing Facilities whose director is Robert J. Benson.

Over the years, the BCL has enjoyed collaborations with most departmental divisions within the medical school but has also found support and enrichment through close ties with other facilities throughout the University. These arrangements are of benefit both to the BCL and to graduate students who find projects and employment among the activities in the laboratory. The Department of Computer Science is under the direction of Dr. Jerome R. Cox, Jr., past Director of the BCL. Strong ties with the Department of Electrical Engineering are sustained through the Engineering School's Biomedical Engineering Program and common interests in digital signal processing techniques.

Four years ago, Washington University established an interschool Institute for Biomedical Computing. The new Institute encompasses the Biomedical Computer Laboratory, the Computer Systems Laboratory, and a new Medical Informatics Group in an organizational setting designed to recognize and foster the joint interests in biomedical computing of the School of Medicine and the School of Engineering and Applied Science. The purpose of the reorganization is to recognize that the development and application of advanced computing and engineering technology to problems in biomedical science are essential components of the research and teaching activities of Washington University. Accordingly, attention has been given to the development of a stable organizational structure that will 1) provide a means by which the primary academic affiliations of its faculty can be in an organizational setting with an adequately broad commitment to research and teaching in biomedical computing; 2) establish a formal administrative connection to the School of Engineering and Applied Science that will facilitate the involvement of its students and faculty in research and instructional activities in biomedical computing; 3) establish mechanisms for administration, funding, and review of appointments, promotion, and tenure for the academic staff of this activity; 4) foster organizational and procedural coherence between the Biomedical Computer Laboratory and the Computer Systems Laboratory by placing them within a common administrative structure; 5) create a focal point for interdisciplinary teaching and student research, both in the School of Medicine and the School of Engineering and Applied Science, in areas that do not fit comfortably into existing departments; and 6) encourage a scholarly environment for the activities of the two computer laboratories that will promote and encourage teaching, research, and publication as vehicles for personal development and academic contribution.

In addition to current BCL and CSL space on the Medical School campus, space for part of the activities of the Institute has been provided on the Engineering School campus by completion of a fifth-floor addition to Lopata Hall in December of 1983. This new space (about 6000 square feet), called the Edward L. Bowles Laboratory, is immediately adjacent to the Departments of Computer Science and Electrical Engineering.

The Institute for Biomedical Computing (IBC) has replaced the former Washington University Computer Laboratories (WUCL) which was a less formal federation of BCL and CSL plus working groups within the Departments of Computer Science and Electrical Engineering. Dr. Charles E. Molnar, Director of the Computer Systems Laboratory, and Dr. Lewis J. Thomas, Jr., Director of the Biomedical Computer Laboratory, are respectively Director and Associate Director of the Institute. Both BCL and CSL continue to retain their identities and internal organizations. Accordingly, this Progress Report addresses activities centered primarily within BCL.

Planning and policy development of the Institute are overseen by a Governing Board, the membership of which is drawn from both Schools. The present composition of the Governing Board is:

J. R. Cox, Jr., Chairman, Department of Computer Science
R. G. Evens, Head, Department of Radiology
G. D. Fischbach, Head, Department of Anatomy and Neurobiology
M. K. King, Dean, School of Medicine
D. M. Kipnis, Chairman, Department of Internal Medicine
E. S. Macias, Chairman, Department of Chemistry and Associate Provost, Science and Technology
J. M. McKelvey, Dean, School of Engineering and Applied Science
C. E. Molnar, Director, Institute for Biomedical Computing
P. Needleman, Chairman, Department of Pharmacology
B. E. Spielman, Chairman, Department of Electrical Engineering
L. J. Thomas, Jr., Associate Director, Institute for Biomedical Computing

To aid in long-range planning of the health-related activities of the Institute, a National Advisory Panel is convened periodically. Particular attention is given to the confluence of important needs in biology and medicine with the technical advances capable of meeting these needs. Successful development may suggest implementation on a larger, perhaps national scale. The present composition of the National Advisory Panel is:

Harrison H. Barrett, Ph.D., Professor of Optical Science and Radiology, University of Arizona, Tucson, AZ

Howard L. Bleich, M.D., Associate Professor, Beth Israel Hospital, Harvard Medical School, Boston, MA

Wesley A. Clark, A.B. (Professor), Clark, Rockoff & Associates, New York, NY

Frederick S. Fay, Ph.D., Professor of Physiology, University of Massachusetts Medical School, Worcester, MA

Frank E. Heart, M.S.E.E., Vice President and Director, Computer Systems Division, Bolt, Beranek & Newman, Cambridge, MA

David M. Kipnis, Professor and Chairman, Department of Internal Medicine, Washington University, St. Louis, MO

William D. Phillips, Ph.D. (retired), Department of Chemistry, Washington University, St. Louis, MO

Robert F. Sproull, Ph.D., Sutherland, Sproull & Associates, Menlo Park, CA

C. Frank Starmer, Ph.D., Professor of Computer Science and Associate Professor of Medicine, Duke University Medical Center, Durham, NC

II. SOURCES OF SUPPORT

During the period covered by this report the primary source of support for the Biomedical Computer Laboratory was from two grants from the National Institutes of Health, Division of Research Resources:

RR 01380 A Resource for Biomedical Computing and

RR 01362 Tissue Characterization via Ultrasonic Imaging.

Collaboration with other investigators often involved work already supported by other grants and contracts:

Public Health Service

CA 41574 Accurate Photon Dose Calculations by Radiotherapy,

CA 42993 Plastic Scintillator as a Dosimeter in Radiotherapy,

CM 47715 Evaluation of High Energy Electron External Beam Treatment Planning,

EY 06582 Peripheral Tests of Color Vision in the Early Diagnosis,

GM 28232 Physical Mapping of Yeast Chromosomal DNA,

HL 07275 Cardiovascular System: Function, Regulation and Pharmacology,

HL 13851 Cyclotron Produced Isotopes in Biology and Medicine,

HL 17646 Study of Ischemic Heart Disease,

HL 25944 Time-of-Flight Positron Tomography for Cardiac Imaging,

HL 28995 Adrenergic Factors and Arrhythmogenic Metabolites,

HL 28998 Tissue Characterization with Ultrasound,

HL 31531 Coronary Vascular Response to Injury: Role in Infarction,

HL 36274 Isoforms of Creating Kinase after Myocardial Infarction,

HL 36773 Mechanisms of Arrhythmogenesis Following Infarction,

HL 40302 Compensating for Anisotropy in Myocardial Ultrasound,

NS 06833 An Interdisciplinary Stroke Program,

NS 23007 Statistical Coding of Complex Stimuli in Auditory Nerve,

RR 01379 Research in VLSI Systems for Biomedical Applications,

RR 03522 Biomedical Network,

National Science Foundation Grants

ECE-85-52518 Presidential Young Investigator Award,

ECS-82-15181 Study of Time-of-Flight Tomography, and

ECS-84-07910 Estimation and Decision for Optical Communication.

Research support was also received from the following industrial collaborators:

AW Corporation, St. Louis, MO and

Digital Equipment Corporation, Maynard, MA.

III. PERSONNEL

EMPLOYEES

Personnel employed by the Biomedical Computer Laboratory during the period covered by this report were:

Director

Lewis J. Thomas, Jr., M.D., and Associate Director of the Institute for Biomedical Computing, and Associate Professor of Biomedical Computing, Anesthesiology, Physiology, and Biomedical Engineering

Associate Director

G. James Blaine III, D.Sc., and Associate Professor of Biomedical Computing in the Institute for Biomedical Computing, Associate Professor of Computer Science in Radiology, and Affiliate Associate Professor of Computer Science

Assistant Director

Russell E. Hermes, M.S., and Affiliate Assistant Professor of Electrical Engineering

Business Manager

Virginia M. Bixon, B.S.

Senior Research Staff

Jerome R. Cox, Jr., Sc.D., Professor of Biomedical Computing in the Institute for Biomedical Computing, and Chairman and Professor of Computer Science, and Professor of Biomedical Engineering in Physiology

Harold W. Shipton, C.Eng., Professor of Biomedical Engineering in the Institute for Biomedical Computing, and Acting Chairman and Professor of Electrical Engineering, and Chairman and Professor of Biomedical Engineering

Donald L. Snyder, Ph.D., Professor of Biomedical Computing in the Institute for Biomedical Computing, and Professor of Electrical Engineering

Research Staff

R. Martin Arthur, Ph.D., Professor of Biomedical Computing in the Institute for Biomedical Computing, and Professor of Electrical Engineering

David E. Beecher, M.S., Research Assistant, and Lecturer in Computer Science, and Research Assistant in Radiology

Kenneth W. Clark, M.S., Research Associate

Heather A. Drury, B.S., Research Assistant

Daniel R. Fuhrmann, Ph.D., Research Associate, and Assistant Professor of Electrical Engineering

Kenneth B. Larson, Ph.D., Research Professor of Biomedical Computing in the Institute for Biomedical Computing, and Research Professor of Neurology (Biomedical Computing)
Joanne Markham, M.S., Research Assistant, and Research Assistant Professor in Medicine
James G. McNally, Ph.D., Assistant Professor of Biomedical Computing in the Institute for Biomedical Computing, Assistant Professor of Cell Biology and Physiology
Michael I. Miller, Ph.D., Associate Professor of Biomedical Computing in the Institute for Biomedical Computing, and Associate Professor of Electrical Engineering
Gregory A. Mohr, Ph.D., Research Associate, and Research Associate in Physics
Stephen M. Moore, M.S., Research Assistant
David G. Politte, M.S., Research Assistant
Frederick U. Rosenberger, D.Sc., Associate Professor of Biomedical Computing in the Institute for Biomedical Computing, and Associate Professor of Electrical Engineering
Kenneth B. Schechtman, Ph.D., Research Assistant, and Assistant Professor of Biostatistics
Raimond L. Winslow, Ph.D., Assistant Professor of Biomedical Computing in the Institute for Biomedical Computing, and Research Assistant Professor of Ophthalmology

Graduate Research Assistants

Steven R. Broadstone, M.S.
Michael A. Brown, M.S.
Mark R. Holland, M.A.
Neophytos Karamanos, M.S.
Mark R. Kaufmann, M.A.
David R. Maffitt, M.S.
Kevin E. Mark, B.S.
Chrysanthe Preza, B.S.
Gwangsoo Rhee, M.S.
Badrinath Roysam, M.S.
Evren Senol, B.S.
Kurt R. Smith, M.S.

Engineering Assistant

Stanley R. Phillips, A.A.S.

Electronic Technician

Deborah A. Schwab

Administrative Coordinator

Shirley A. Gonzalez-Rubio

Secretaries

Rebecca J. Bozesky
Polly E. Raith

The following members from other departments and divisions have joint appointments with the Biomedical Computer Laboratory to facilitate collaboration and enhance interdisciplinary research:

H. Dieter Ambos, Research Assistant Professor of Medicine (Cardiology)
William M. Hart, Jr., M.D., Ph.D., Professor of Ophthalmology
Rexford L. Hill III, M.S., Associate Professor of Computer Applications in Radiology
James G. Miller, Ph.D., Professor of Physics, and Associate Director for Biomedical Physics, Laboratory for Ultrasonics, and Research Professor of Medicine
John W. Wong, Ph.D., Assistant Professor in the Institute for Biomedical Computing, and in Radiation Physics in Radiology

In addition, the following people worked at the laboratory for brief periods:

Gary E. Christensen, B.S.
Brian S. Edmonston
Gaurav K. Garg
Jason G. Gutenschwager
Mark A. Hassen, M.S.
Andrew T. Loth
Tony Mazraani
Frank W. Simcox, B.S.
Gregory M. Tormo
David M. Wade
Qiang Wu, M.S.

RESEARCH COLLABORATORS

During the period covered by this report the following investigators from other laboratories, departments, or institutions, collaborated with BCL staff members on problems of joint interest:

D. R. Abendschein, Ph.D., Medicine
D. I. Altman, M.D., Neurology
T. R. Baird, Medicine
B. Barzilai, M.D., Medicine
S. R. Bergmann, M.D., Ph.D., Medicine
J. J. Billadello, M.D., Medicine
W. R. Binns, Ph.D., Physics
M. A. Brown, M.B.B.S., Medicine
T. J. Chaney, M.S., Computer Systems Laboratory
P. B. Corr, Ph.D., Medicine and Pharmacology
J. W. Epstein, Physics
D. C. Ficke, B.S., Radiology
H. L. Fontanet, M.D., Medicine
P. T. Fox, M.D., Neurology and Radiology
E. M. Geltman, M.D., Medicine
R. L. Grubb, Jr., M.D., Neurological Surgery
W. B. Harms, B.S., Radiology
P. Herrero, M.S., Medicine
P. Herscovitch, M.D., Neurology and Radiology

D. G. Hirsh, B.A., Office of the Network Coordinator
S. Igielnik, Ph.D., Medical Computing Facilities
M. H. Israel, Ph.D., Physics
A. S. Jaffe, M.D., Medicine
G. C. Johns, B.S., Computer Systems Laboratory
R. G. Jost, M.D., Radiology
C. M. Kilo, M.D., Medicine
J. Klarmann, Ph.D., Physics
M. P. Land, B.S., Pathology
E. T. Macke, M.S., Computer Systems Laboratory
J. W. Matthews, D.Sc., Computer Systems Laboratory
T. R. Miller, Radiology
M. A. Mintun, M.D., Radiology
C. E. Molnar, Sc.D., Computer Systems Laboratory
R. E. Morley, Jr., D.Sc., Electrical Engineering
R. Nesher, M.D., Ophthalmology
M. V. Olson, Ph.D., Genetics
R. E. Olson, Computer Systems Laboratory
J. M. Peirick, M.S., Medicine
C. A. Perez, M.D., Radiology
J. E. Perez, M.D., Medicine
J. S. Perlmutter, M.D., Neurology
S. M. Pogwizd, M.D., Medicine
W. J. Powers, M.D., Neurology and Radiology
J. A. Purdy, Ph.D., Radiology
M. E. Raichle, M.D., Neurology and Radiology
A. P. Rueter, B.S., Radiology
J. E. Saffitz, M.D., Ph.D., Pathology and Medicine
T. J. Schulz, M.S., Electrical Engineering
L. M. Seacord, M.D., Medicine
B. A. Siegel, M.D., Radiology
B. E. Sobel, M.D., Medicine
A. W. Strauss, M.D., Pediatrics
S. P. Sutera, Ph.D., Mechanical Engineering
M. M. Ter-Pogossian, Ph.D., Radiology
R. G. Tilton, Ph.D., Pathology
G. L. Trick, Ph.D., Ophthalmology
J. S. Turner, Ph.D., Computer Science
Z. Vered, Medicine
M. N. Walsh, M.D., Medicine
C. J. Weinheimer, B.S., Medicine
M. J. Welch, Ph.D., Radiology
J. R. Williamson, M.D., Pathology
K. A. Yamada, Ph.D., Medicine
P. Y. Yan, B.S., Computer Systems Laboratory
X. Ying, D.Sc., Radiology
C. W. Yu, M.S., Radiology
J. B. Zimmerman, D.Sc., Radiology and Computer Science

Medical College of Ohio, Toledo, Ohio

S. S. Hancock, M.S.

University of Pennsylvania, Philadelphia, Pennsylvania

J. M. Ollinger, D.Sc.

IV. PHYSICAL RESOURCES

The Biomedical Computer Laboratory (BCL), adjacent to the Washington University School of Medicine's main building complex, occupies 12,000 square feet (net) of floor space at 700 South Euclid Avenue in St. Louis. The Institute for Biomedical Computing (IBC), comprised of BCL and the Computer Systems Laboratory (CSL), occupies another 6000 square feet of floor space (Edward L. Bowles Laboratory) of the fifth floor of Lopata Hall immediately adjacent to the Departments of Computer Science and Electrical Engineering on the University's other campus, some two-and-a-half miles to the west of the Medical School campus. BCL staff members and systems frequently occupy other areas within the University at the sites of collaborative project activities.

BCL's electronics shop was moved this year within the 700 South Euclid building. The former shop space was renovated for an Image Presentation, Analysis, and Quantification (IPAQ) Lab. Within the IPAQ Lab are most of the Resource's workstations and a conference facility.

While involved in addressing diverse biomedical problems for which digital computing techniques seemed promising and appropriate, the BCL has acquired and applied the necessary instrumentation and computing resources for collaborative research projects in biological modeling and algorithm development for quantitative imaging. Current computer resources include: two Digital Equipment Corporation (DEC) MicroVAX-II's, three DEC VAXstations, four MASSCOMP machines (a 5400, two 5500's, and a 55020 workstation), an IBM PC/AT, and an Apple MacIntosh. On indefinite loan is an IBM RT PC. Major instrumentation includes a Datacopy reflectance camera for image acquisition.

Within the Resource, terminal access to computer systems is provided by TERRANET, a BCL-developed local area network. Laboratory computer systems are connected by an Ethernet local area network. Inter-network communication between other departmental networks is provided via connections to the Mallinckrodt Institute of Radiology PACS network and the Biomedical Research network installed throughout both Washington University Campuses. The networks provide resource personnel access to a broad spectrum of computing equipment, imaging modalities, and other services such as electronic mail.

Other physical resources include an IBC reference room, a well-stocked electronics shop, a modest inventory of electronic and computer test equipment, microprocessor development systems, analog and digital recording instruments, and photographic supplies and equipment.

V. RESEARCH PROJECTS

Introduction

The research program of the Biomedical Computer Laboratory (BCL) is currently organized into six major project areas with the staff grouped into teams whose interests are focused correspondingly. Because of the Laboratory's emphasis on quantitative imaging, that category has been divided into three areas, each dealing with a different imaging modality (positron-emission tomography, ultrasonic tissue characterization, and optical-sectioning microscopy). A total of 38 distinct project activities are grouped into the six project areas briefly summarized below. More complete summaries are given at the beginning of each of the project-report subsections.

Information extraction from quantitative biomedical images continues to increase in prominence within the BCL program. Accordingly, organization of such activities into three categories (by imaging modality) is continued this year. For positron-emission tomography (PET), work in support of applications to heart and brain imaging as well as system improvements have continued on several fronts, but the main thrust of BCL activities has been in research on algorithms. Emphasis has been on application of the maximum-likelihood (ML) method for improving image quality and for achieving better estimates of physiological parameters through studies of dynamic distributions of tracers. Fundamental limitations in the use of the maximum-likelihood method for image reconstruction have been identified. Ways to overcome those limitations have been shown to reduce greatly the artifacts that have plagued those applying the EM algorithm to image reconstruction. Also, we have shown that application of the ML method for time-of-flight PET achieves reductions in the variances of the estimates of 3 to 5 fold compared to the confidence-weighted method, in brain-phantom studies.

The work in ultrasonic tissue characterization has emphasized the interpretation of backscattered ultrasonic energy to achieve quantitative estimates of tissue properties, including anisotropy and the state of contraction of cardiac and skeletal muscle, while parallel efforts have been directed toward design of a system to employ adaptive beamforming for backscatter measurements. This project became focused primarily on cardiovascular applications and so, since May 1988, it is being carried out and supported (by NHLBI) independently of the BCL program.

Optical-Sectioning Microscopy is a new research area for BCL. The objective is to use advanced image-estimation methods to extract improved plane-by-plane information from three-dimensional specimens by reducing the blurring effects of adjacent planes. Image estimation methods similar to those applied to positron-emission tomography are being explored as promising candidates for achieving more accurate optical sectioning than do other methods currently in use elsewhere. Scanning confocal microscopy is also under study for comparison to the above, and for possible improvement by application of the new image-estimation algorithms.

Ischemic heart disease and ECG analysis continues to be a major category of research activity, but the development of new algorithms for ECG processing has been discontinued, although some attention continues on exportation of the latest version of our "Argus" algorithm. The separate support mentioned last year for completing a clinical-event database for evaluating ambulatory ECG-monitoring systems was awarded but rejected because it was too little and too late. In the area of ischemic heart disease, more prominent are modeling, signal processing, and data analysis work in collaboration with the division of Cardiovascular Medicine as part of their broad program addressed to ischemic heart disease.

Systems for Specialized Biomedical Studies embraces a variety of projects that are less broad in scope either because they are in an earlier stage of development or because the nature of the work is necessarily more specialized. The biomedical-imaging theme is well represented in this section, especially in the area of electron-microscopic autoradiography and automated image segmentation. Work on data acquisition and analysis for DNA restriction mapping has achieved very high quality digital images directly from fluorescent electrophoretic gels and new algorithms show promise for improved extraction of DNA fragment-size data from the images.

Projects under Resource Development Activities are directed toward improving the Laboratory's capabilities for addressing the needs of multiple research studies involving various facets of biomedical imaging. To that end, a now dominant and integrating activity is the development of a distributed facility for image presentation, analysis and quantification (IPAQ). Components of the IPAQ project include (1) the enhancement of our computational capabilities to support the development of computationally demanding algorithms for information extraction from multi-dimensional measurement data, (2) the establishment of a coherent software environment which incorporates a set of internally consistent software tools, image data formats and display methodologies, (3) the extension of our digital communication capabilities to include the sites of collaborators' data sources and information destinations, and (4) the exportation of specialized, tailored subsystems and/or satellite workstations which may incorporate custom-designed, state-of-the-art parallel-processing systems in order to achieve practical realizations of especially demanding computations.

A. Quantitative Imaging: Positron-Emission Tomography

Stimulated by the clinical impact of the EMI transmission tomographic scanner in 1973, experimental studies were initiated in collaboration with the Division of Radiation Sciences to evaluate positron coincidence-detection as a method for emission reconstruction tomography. This collaborative activity resulted in a prototype scanner called PETT (Positron-Emission Transaxial Tomograph). Extensive studies in patients and animals were conducted with the PETT III scanner in collaboration with the divisions of Neurology and Cardiology. A subsequent scanner, PETT IV, utilized concepts developed with its predecessor but incorporated a novel technique for the simultaneous collection of four tomographic slices from a single set of detectors. Until its decommissioning four years ago, PETT IV was located in the Coronary Care Unit for use in the SCOR project for the quantification of regions of myocardial ischemia and infarction. Subsequent scanners have been developed that permit more rapid data collection and improved spatial resolution. One of these, PETT V, was used in experimental studies in dogs. PETT VI became operational during the summer of 1980 and employs fast detectors and an entirely circular motion. This tomograph was used in experimental studies in dogs (A-1) and in brain blood-flow studies (A-4). Developments in crystal technology and high-speed electronics now permit the propagation time of each of the two photons created in an annihilation to be measured. Theoretical and experimental studies of tomography systems that utilize this additional information continued, and the software and hardware needed to realize the predicted benefits have been developed. Super PETT I, the first operational system utilizing time-of-flight information, has been in routine use in the Coronary Care Unit for over three years now (A-1 to A-3). This tomograph was also used for the collection of experimental data used for the evaluation of reconstruction algorithms (A-5). A second generation time-of-flight tomograph, Super PETT II, for head and body scans has been developed and has now been moved to the Division of Radiation Sciences. Studies to improve data acquisition and reconstruction algorithms for Super PETT I and Super PETT II continued during the year (A-5 to A-8). This work includes the study of fundamental limitations in the use of the maximum-likelihood technique for image reconstruction and in sound ways to overcome these limitations (A-5). The study of novel processing architectures for producing image reconstructions in clinically useful times continued (A-8). A new study was initiated of a positron-emission tomograph having a spherical geometry for imaging radionuclides (A-9). Lastly, a parameterized approach for maximum-likelihood reconstruction was studied (A-10).

A-1. PETT Experimental Studies

Personnel: S. R. Bergmann, M.D., Ph.D., Medicine
M. A. Brown, M.B.B.S., Medicine
P. Herrero, M.S., Medicine
J. Markham, BCL
B. E. Sobel, M.D., Medicine
M. J. Welch, Ph.D., Radiology

Support: RR 01380
HL 13851
HL 17646

The overall aim of this project is to implement and evaluate procedures required to translate into intact animals and humans the results obtained with selected positron-emitting tracers used to characterize myocardial metabolism and perfusion in isolated hearts and in anesthetized, open-chest dog studies performed with an isolated probe system. Utilizing positron-emission tomography with PETT VI, the distribution of tracers and the time-course of their uptake and clearance from myocardium can be quantified. Studies are intimately related to interpretation of tomographs obtained in clinical studies using Super PETT I (A-2).

We previously demonstrated that the myocardial turnover rate constant of ^{11}C-acetate from isolated perfused hearts provided an index of myocardial oxygen consumption. To evaluate the validity of these measurements in vivo, we measured the turnover rate constant in eight anesthetized dogs at rest and again after myocardial work had either been increased by sympathetic stimulation or decreased by beta-blockade and hypotension; and in twelve dogs at rest and again after myocardial substrate utilization had been altered by intravenous infusion of glucose or lipid. Correlations between the turnover rate constants and myocardial oxygen consumption over the range from 1.38-10.57 mmol/g/min (measured directly) and with rate pressure products from 4984-34680 mm Hg × beat/min were close ($r = 0.88$ for both relationships). Despite increases of arterial glucose or fatty-acid concentrations of more than five-fold and concomitantly induced changes in myocardial substrate utilization, the close relationship between the turnover rate constant and directly measured myocardial oxygen consumption persisted. Thus, estimates of myocardial oxygen consumption with ^{11}C-acetate appeared to remain valid over a wide range of flow and metabolic states and despite altered patterns of myocardial substrate utilization. Thus, the turnover rate constant after intravenous administration of radiolabeled acetate appears to provide a useful, noninvasive estimate of regional myocardial oxygen consumption.

To demonstrate the utility of the use of ^{11}C-acetate in myocardium, we evaluated the dependence of recovery of stunned myocardium on restoration of oxidative metabolism. Myocardium subjected to transient ischemia followed by reperfusion exhibits functional recovery only slowly. Criteria predictive of ultimate recovery are ill-defined. Accordingly, we evaluated six dogs with reperfusion for four weeks after one hour of ischemia - intervals selected to elicit minimal infarction but substantial

myocardial stunning. Myocardial blood flow and oxygen consumption were evaluated sequentially using positron-emission tomography with $H_2{}^{15}O$ and ^{11}C-acetate; and regional wall thickening was assessed with quantitative two-dimensional echocardiography. Myocardial blood flow was diminished during ischemia but recovered to normal by one hour of reperfusion. In contrast, MVO_2 in reperfused regions only recovered to greater than 90% of normal by one week. Systolic wall thickening remained severely impaired early after reperfusion and recovered only in zones exhibiting restoration of MVO_2. By three weeks, systolic wall thickening had recovered completely. Thus, recovery of MVO_2 portends the recovery of regional ventricular performance after myocardial reperfusion.

In the past year, we have made significant progress in overcoming the physical limitations of PET. We previously demonstrated that myocardial blood flow (MBF) could be quantitated with $H_2{}^{15}O$ and direct tissue analysis. However, measurement of MBF in absolute terms with PET has been limited because of cardiac motion and by partial-volume and spillover effects when imaging an object less than two times the full width at half maximum resolution of the tomographic instrument. In conjunction with Project A-3 (Corrections for PET Cardiac Studies) we developed a parameter-estimation procedure in which spillover and partial-volume effect corrections were derived mathematically. In eleven dogs evaluated at rest and after flow had been diminished by coronary occlusion or enhanced with dipyridamole, correlation with MBF measured with microspheres over the flow range from 0.35-5.04 ml/g/min was close ($r = 0.95$, $n = 28$ observations). Thus, it appears MBF can be assessed noninvasively with $H_2{}^{15}O$ without the need for independent measurements of wall thickness or cavity dimensions.

A critical diagnostic need in clinical cardiology is the ability to identify jeopardized, but viable myocardium. Fluoromisonidazole is a compound that appears to bind to hypoxic but non-necrotic cells. We hypothesized that it might be useful as a marker of reversibly injured myocardial tissue, and characterized the myocardial handling of ^{18}F-fluoromisonidazole in isolated perfused rabbit hearts. Residual activity in control hearts averaged 25 ± 5% of peak activity and increased to 62 ± 7% with ischemia and 61 ± 11% with hypoxia (control flow but perfusate pO_2 < 50 mm Hg, $p < 0.01$ for each compared with control). We then evaluated the myocardial uptake of ^{18}F-fluoromisonidazole noninvasively with PET in dogs subjected to coronary thrombosis. Regions of jeopardized myocardium were defined as those with diminished flow measured with $H_2{}^{15}O$. In five dogs, ^{18}F-fluoromisonidazole was administered intravenously within three hours of occlusion. Sixty minutes after injection, the ratio of uptake in ischemic compared with normal myocardium was 1.4 ± 0.2 (standard deviation) reflected by a "hot spot". In contrast, when ^{18}F-fluoromisonidazole was administered greater than twenty-four hours after occlusion ($n = 7$) the ratio was 0.8 ± 0.2 ($p < 0.01$ compared with early administration). Thus, it appears that this radionuclide may be a positive marker of ischemic but potentially salvageable myocardium and may be useful in identifying myocardium that may benefit from therapeutic intervention.

The major goal in the coming year is to evaluate whether recovery of function after reperfusion with ischemia of longer durations also correlates with recovery of oxidative metabolism detectable noninvasively

with ^{11}C-acetate. In addition, we will continue our studies of myocardial perfusion with further refinements for partial-volume and spillover effects. Finally, further assessment of the utility of ^{18}F-fluoromisonidazole in the setting of acute myocardial ischemia and reperfusion will be evaluated.

A-2. Super PETT I Cardiac Studies

Personnel: E. M. Geltman, M.D., Medicine
H. D. Ambos, Medicine
T. R. Baird, Medicine
A. S. Jaffe, M.D., Medicine
J. Markham, BCL
B. E. Sobel, M.D., Medicine
M. M. Ter-Pogossian, Ph.D., Radiology
M. N. Walsh, M.D., Medicine
C. J. Weinheimer, B.S., Medicine
M. J. Welch, Ph.D., Radiology

Support: RR 01380
HL 13851
HL 17646

This project is designed to characterize regional myocardial metabolism and perfusion quantitatively with positron-emission tomography (PET) in normal subjects and patients with coronary artery disease at rest and in response to stress induced with vasodilators or dynamic exercise. It is designed also to assess the efficacy of reperfusion induced by thrombolysis, balloon angioplasty, surgical revascularization, and combinations of the three reflected by myocardial perfusion and metabolic activity.

During this past year, studies have focused on two general areas: validation and implementation of quantitative assessment of myocardial perfusion with $H_2{}^{15}O$ and positron emission tomography, and the evaluation of myocardial oxidative metabolism with ^{11}C-acetate. Estimates of relative myocardial blood flow made with previously validated PET estimates of relative regional perfusion with the use of $H_2{}^{15}O$ were performed before and after single-vessel percutaneous transluminal coronary angioplasty (PTCA). Mathematical models applied to PET data have been developed in experiments in animals (A-1, A-3) for the absolute quantification of myocardial perfusion on an ml/g/min basis. These models and techniques have been validated in cardiac phantoms and experimental animals and extended to human subjects. The results indicate that positron emission tomography with $H_2{}^{15}O$ permits absolute quantification of myocardial perfusion in normal subjects and patients and that PET demonstrates diminished resting perfusion distal to clinical coronary stenoses in patients.

We have shown previously that clearance of ^{11}C-acetate from myocardium correlates closely with oxygen consumption in hearts of experimental animals. To assess its value in patients, we studied five normal volunteers without cardiac disease and four patients with myocardial infarction by dynamic PET after intravenous administration of 0.4 mCi/kg of ^{11}C-acetate. Myocardial images were of excellent quality. In normal subjects, the tracer was distributed homogeneously. In patients with infarction, distinct defects of uptake of ^{11}C-acetate were noted. The coefficient of variation of $t_{1/2}$ of distant and peri-infarct zones was greater in patients (25 $\pm$ 3%) than in controls ($p < .001$). Thus, heterogeneity of residual oxidative metabolism in patients with infarction is readily detectable by PET with ^{11}C-acetate - a tracer potentially useful for evaluation of efficacy of interventions designed to salvage myocardium.

Studies in progress are designed to further validate and implement the techniques for absolute quantification of $H_2{}^{15}O$ in normal subjects and patients with specific forms of heart disease, such as syndrome X, hypertensive heart disease, and hypertrophic cardiomyopathy, in which myocardial perfusion reserve may be impaired. Clinical studies are planned to further assess the regional kinetics of ^{11}C-acetate in normal subjects and patients with coronary artery disease, including patients with chronic anginal syndromes and with acute myocardial infarction treated conventionally or with thrombolytic therapy. In addition, the patterns of alteration in regional kinetics of ^{11}C-acetate in normal subjects and patients with chronic coronary artery disease will be studied before and after pharmacologic stress induced with dobutamine. Initial studies suggest that myocardial clearance of ^{11}C-acetate is markedly accelerated in normal subjects after dobutamine infusion in proportion to augmentation of the double product.

A-3. Corrections for PET Cardiac Studies

Personnel: J. Markham, BCL
S. R. Bergmann, M.D., Ph.D., Medicine
P. Herrero, M.S., Medicine

Support: RR 01380
HL 17646

Previous studies have demonstrated that the one-compartment Kety model can be utilized for noninvasive measurement of myocardial blood flow with positron-emission tomography following injection of $H_2{}^{15}O$ if radioactivity in the blood and myocardium are known. However, measurements of tracer concentration in the left-ventricular blood pool and in myocardial tissue with PET reflect the errors due to partial volume and spillover effects as well as cardiac and respiratory motion.

Using a cardiac phantom, we validated corrections for the effects of partial volume and spillover with a simulation technique based on the convolution of the reconstructed tomographic point-spread function with the measured dimensions of the phantom (PR 23, A-3). Simulated image profiles were derived based on the assumptions that the point-spread function in one dimension is Gaussian and that the activity in the blood pool and tissue are each uniformly distributed. Comparison of the simulated image with the reconstructed image of the phantom showed an excellent correlation.

Correction factors for the effects of partial volume and spillover were then computed from the simulated profiles. Validation of this method in eight dogs showed a good correlation between blood flow estimated with microspheres and the PET method [1]. Error analysis of the procedure indicated, however, that estimated flow values were very sensitive to errors in the dimensions of the blood chamber and wall thickness.

Because of the difficulty of measuring the dimensions of the heart in vivo, the equation used to estimate flow with the Kety-Schmidt model was modified to include the two correction fractions as parameters to be estimated. The fraction of myocardial activity recorded in the observed tissue counts and the fraction of activity originating from the blood pool and observed as myocardial activity are multiplied by the theoretical tissue curve, computed from the Kety-Schmidt equation, and the observed blood pool curve, respectively; the two terms are then summed to represent the observed tissue activity. Using this model, myocardial blood flow measured from PET images correlated closely to flow determined from microspheres in six dogs when flow was normal or elevated due to intravenously administered diapyridamole. Estimates obtained for low-flow regions were unreliable, probably because of the noise associated with low-count data.

Future efforts will be directed toward improving estimates of flow from ischemic regions. Methods for reducing the noise in the time-activity curves will be investigated along with improved procedures for estimation of flow from PET scans.

1. Herrero, P., Markham, J., Myears, D. W., Weinheimer, C. J., and Bergmann, S. R., "Measurement of Myocardial Blood Flow with Positron Emission Tomography: Correction for Count Spillover and Partial Volume Effects," in Mathematical Modelling in Science and Technology, E. Y. Rodin and X. J. Avual, eds., Sixth International Conference Proceedings, Great Britain, Pergamon Press, 11:807-812, 1988.

A-4. In Vivo Measurements of Regional Blood Flow and Metabolism in the Brain

Personnel: M. E. Raichle, M.D., Neurology and Radiology
D. I. Altman, M.D., Neurology
D. C. Ficke, B.S., Radiology
P. T. Fox, M.D., Neurology and Radiology
R. L. Grubb, Jr., M.D., Neurological Surgery
K. B. Larson, BCL
J. Markham, BCL
M. A. Mintun, M.D., Radiology
J. S. Perlmutter, M.D., Neurology
W. J. Powers, M.D., Neurology and Radiology
M. M. Ter-Pogossian, Ph.D., Radiology
M. J. Welch, Ph.D., Radiology

Support: RR 01380
HL 13851
HL 25944
NS 06833
ECS 8215181
Washington University

Because of the previously noted (PR 21, D-3; PR 22, D-4; PR 23, A-4) deficiencies of compartmental models for estimating cerebral blood flow with positron-emission tomography (PET) using radioactive water as a tracer, we have been led to the formulation and testing of distributed-parameter models for this purpose. The distributed-parameter models we have investigated take into account longitudinal gradients of tracer concentration along the capillaries but assume that transverse gradients are zero. The resulting conservation conditions take the form of sets of partial differential equations in the concentrations, with axial distance and time as independent variables and with capillary and cellular permeabilities, surface areas, volumes, and thermodynamic-activity coefficients as parameters. We have obtained analytical solutions for the conservation equations in the form of unit-impulse and unit-step responses suitable for simulations of dynamic residue-detection data.

Encouraged by close agreement between our model predictions and external counting-rate data obtained in animal experiments [1] (PR 21, D-3; PR 22, D-4), we have continued with our investigations of the possibility of applying our distributed-parameter model for measurement of cerebral-blood flow (CBF) in patients (PR 23, A-4) using PET. We have explored the possibility of implementing our model for this purpose through use of a table-lookup procedure. A table of CBF values versus simulated PET counts is generated after each patient PET scan. Inputs for generation of the table are the arterial blood-activity sequence, the scan starting time, and the scan duration. All model parameters except CBF are set to average values. We are presently endeavoring to identify an appropriate parameter set for this purpose, taking into account the correlations we have previously observed between CBF and the permeability parameters of our model.

1. Larson, K. B., Markham, J., and Raichle, M. E., "Tracer-Kinetic Models for Measuring Cerebral Blood Flow Using Externally Detected Radiotracers," Journal of Cerebral Blood Flow and Metabolism, 7:443-463, 1987.

A-5. Evaluation of Noise- and Edge-Artifact Suppression Techniques Using Super PETT I Phantom Data

Personnel: D. G. Politte, BCL
K. W. Clark, BCL
J. Markham, BCL
M. A. Mintun, M.D., Radiology
S. M. Moore, BCL
D. L. Snyder, BCL
L. J. Thomas, Jr., BCL

Support: RR 01380

In this study we have reconstructed images from both simulated data and data collected from Super PETT I in order to evaluate the noise- and edge-artifact suppression techniques necessary for maximum-likelihood estimation (PR 23, A-5, A-6) [1], to compare simulated data to actual data, and to compare the quality of images produced by the confidence-weighting (CW) and maximum-likelihood (ML) algorithms. Each of the three phantoms shown in Figure 1 was filled with $H_2{}^{15}O$ and scanned with Super PETT I, operated in the high-resolution mode, for a sufficient length of time to collect at least 1,000,000 registered coincidence events, or counts. The simulated measurement error was chosen to match that of Super PETT I as closely as possible.

The quality of the reconstructed images depends on many factors, including the number of counts, the widths of the resolution kernel and sieve kernel used to suppress the edge and noise artifacts, and the number of iterations of the expectation-maximization algorithm used to compute the maximum-likelihood estimates. We systematically varied all of these parameters, but the results presented here are for the case in which each image is reconstructed from approximately 100,000 counts, the resolution and sieve kernels are each circularly symmetric Gaussian densities with full-width-at-half-maximums of 7.5 cm, and 200 iterations of the expectation-maximization algorithm were used. The real data were precorrected before reconstruction in the usual way using independent data from the transmission scan.

The large voids of the phantom shown in Figure 1a are useful for testing the suppression of the noise artifact because they contain uniform concentrations of radioactivity. The large voids are also useful for testing the suppression of the edge artifact because the regions are large enough to permit the formation of this artifact and because there are

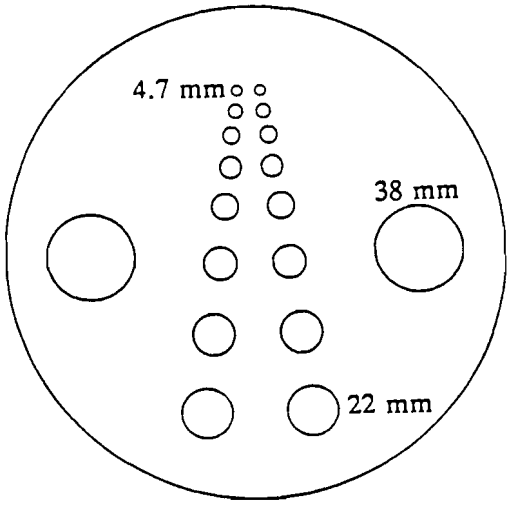

a) holes phantom

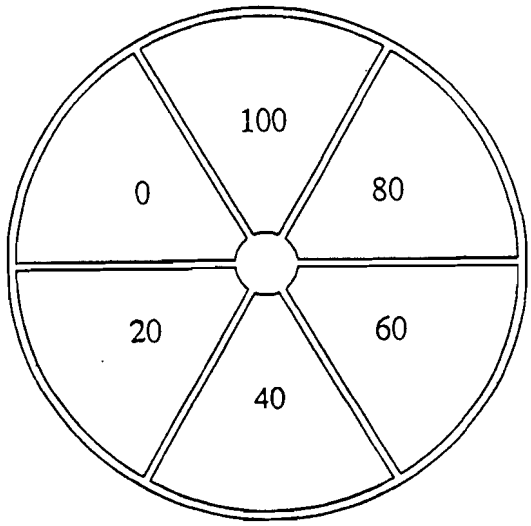

b) pie phantom

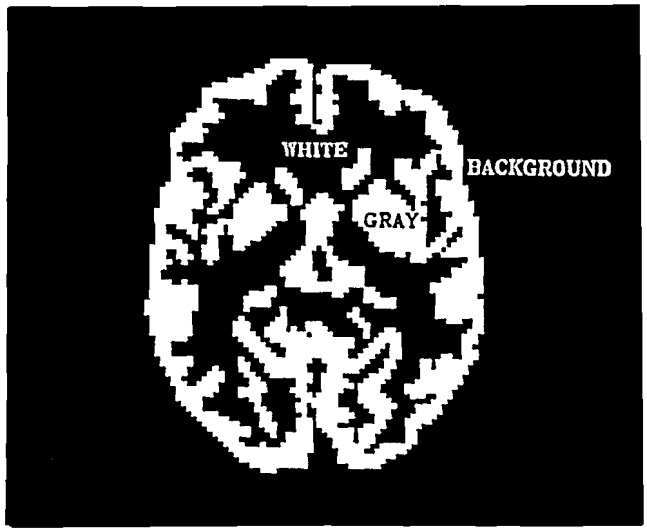

c) Hoffman brain-phantom

Figure 1. The three phantoms shown above were used to evaluate image-reconstruction algorithms and artifact-suppression techniques for PET. a) The holes phantom consists of 18 circular voids in a lucite cylinder connected by a common reservoir. The overall diameter is 221.6 cm; diameters of three sets of voids are indicated on the diagram. b) The pie phantom, 19.8 cm in diameter, consists of six equally-sized water-tight chambers which were filled with radioactivity concentrations of 100, 80, 60, 40, 20, and 0 relative units, as indicated. c) The Hoffman brain-phantom portrays the 4 to 1 ratio of blood flow in the gray and white matter of the human brain. There is no radioactivity in the exterior background region.

sudden drops in the concentration of radioactivity at the boundaries. The small voids are useful for testing the resolution of the reconstructed images. Our qualitative assessment of many images reconstructed with many combinations of resolution and sieve kernels is that proper choices of these kernels successfully suppress both artifacts while maintaining resolution at least as good as that of the images reconstructed with the confidence-weighting algorithm.

The pie phantom shown in Figure 1b consists of six equally-sized compartments with relative radioactivity concentrations of 100, 80, 60, 40, 20, and 0 units. Ideally, the middle of each compartment should be reconstructed as a nearly flat intensity. In order to quantify the deviation about the correct flat intensity, the sample variance of the reconstructed image values was computed for the set of pixels inside of each of the six compartments, excluding a one-centimeter buffer adjacent to the boundaries. The variance is plotted against the average counts per pixel in Figure 2, for both the real and simulated data. We conclude that the confidence-weighting algorithm reconstructs images with much higher variance, especially in compartments of the pie with relatively low radioactivity. Furthermore, the ratio of the variance of the images reconstructed with the confidence-weighting and maximum-likelihood algorithms increases when actual PET data are used.

The Hoffman brain-phantom shown in Figure 1c portrays the 4 to 1 ratio of blood flow in the gray- and white-matter regions of the brain (with no activity in the exterior background region). A study was performed in which 25 statistically independent simulated data sets were calculated and each was reconstructed using both the confidence-weighting and maximum-likelihood algorithms. The sample variance was calculated on a pixel-by-pixel basis for the 25 reconstructed images and then averaged separately over each of the three regions. The ratios of Var_{CW}/Var_{ML} are shown in Table 1. Note that there is a substantial reduction in variance when constrained maximum-likelihood estimation is used, and that, as with the pie phantom, the reduction is greatest in regions with low radioactivity. The improvement in the variance has important implications on the accuracy of numerical parameters which can be extracted from PET image data.

We have begun to incorporate corrections for random coincidences and attenuation directly into the iterations of the expectation-maximization algorithm, instead of using the usual method of precorrection. Preliminary results show that the new correction method is necessary to avoid bias in the images, and a further reduction in the variance is also achieved.

1. Snyder, D. L., Miller, M. I., Thomas, Jr., L. J., and Politte, D. G., "Noise and Edge Artifacts in Maximum-Likelihood Reconstructions for Emission Tomography," IEEE Transactions on Medical Imaging, MI-6(3):228-238, September 1987.

2. Politte, D. G. and Snyder, D. L., "The Use of Constraints to Eliminate Artifacts in Maximum-Likelihood Image Estimation for Emission Tomography," IEEE Transactions on Nuclear Science, 35(1):608-610, 1988.

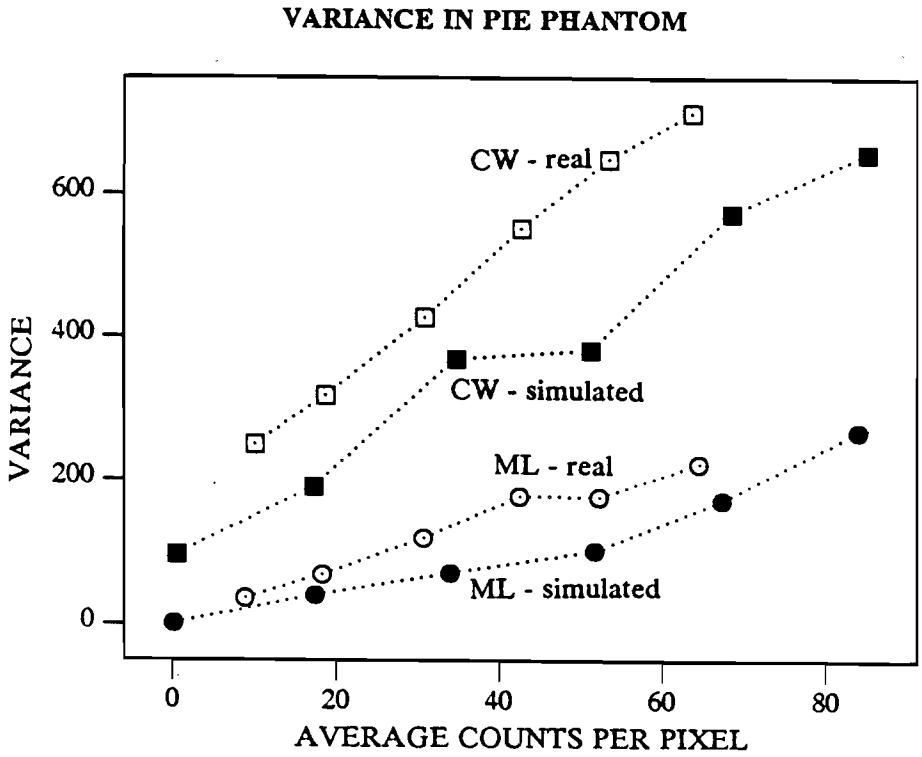

Figure 2. The sample variances of the image values, computed separately for the pixels inside each compartment of the pie phantom, are plotted above. The simulated and real data, each containing approximately 100,000 counts, were reconstructed with both the confidence-weighting (CW) and maximum-likelihood (ML) algorithms. Only pixels interior to and farther than one centimeter from the boundary of a given compartment were included in the calculations.

VARIANCE IN BRAIN PHANTOM	
Region	Var_{CW}/Var_{ML}
Background	34
White Matter	4.7
Gray Matter	3.2

Table 1. The ratios of the average variances of images reconstructed with the confidence-weighting and the constrained maximum-likelihood algorithms are shown in the table above. The sample variance was computed on a pixel-by-pixel basis from 25 images reconstructed from statistically independent data. The average variances were then calculated separately for each region of the brain. Each image was reconstructed from approximately 100,000 counts.

A-6. Investigation of Methods for Speeding Maximum-Likelihood Image Reconstruction with the EM Algorithm

Personnel: D. G. Politte, BCL
K. W. Clark, BCL
S. M. Moore, BCL and Medicine
D. L. Snyder, BCL

Support: RR 01380

Several strategies are being pursued to speed the computation of maximum-likelihood image reconstructions with the expectation-maximization (EM) algorithm. These include applying massively parallel processors (A-8, E-8). In this section we review efforts devoted to speeding the computations on a conventional computer.

Our efforts have concentrated on an implementation of the EM algorithm in which many of the computations are done in a coordinate system which is rotated relative to the coordinate system of the image. We partition the data according to the quantized angle of the photon flight line. The processing for each iteration for each angle involves the following steps: rotate the previous image array into the new coordinate system, convolve this result with a two-dimensional kernel (which has far fewer samples than the image), divide this result into the data, convolve this result with the same two-dimensional kernel used before, rotate the resulting image array back to the coordinate system of the image, and finally, accumulate this result into an array. After this procedure is repeated for each angle then the next iteration is begun, if necessary.

The two-dimensional convolution step is efficiently implemented in the rotated coordinate system because the kernel is an asymmetric Gaussian which is separable in the rotated system; the two-dimensional convolution is implemented as two one-dimensional convolutions, one along each axis. In the future, incorporating corrections for random coincidences and attenuation internal to the iterations of the EM algorithm will be simplified when the computations are done in the rotated coordinate system.

The latest version of software has incorporated data structures called masks [1] which are used to efficiently limit the regions of arrays over which computations are performed to be as small as possible. This is possible because first, the data arrays are sparse, and second, the Gaussian convolution kernels approach zero rapidly for spatial coordinates far from their centers; we truncate them to zero for large arguments. The rotation, convolution, and division steps are calculated for only those image pixels or data bins for which the computation will effect the final answer.

Typical reconstructions of simulated data or data from Super PETT I take from two to ten minutes per iteration on the MASSCOMP 55020 processor, depending on the sparseness of the data.

1. Politte, D. G., "Constrained Maximum-Likelihood Image Estimation for Time-of-Flight PET via the EM Algorithm Implemented in a Rotated Coordinate System," BCL Working Note No. 82, June 1988.

A-7. Evaluation of the Weighting Algorithm for Dynamic Tracer Studies

Personnel: J. Markham, BCL
J. M. Ollinger, D.Sc., University of Pennsylvania
D. G. Politte, BCL
D. L. Snyder, BCL
L. J. Thomas, Jr., BCL

Support: RR 01380

A new method for maximum-likelihood estimation of parameters in dynamic tracer studies utilizing PET data was developed and tested for simulated data (PR 22, D-11) [1-2]. This method, called the weighting algorithm, consists of an initial step in which histograms of high temporal resolution are generated directly from list-mode data utilizing a few reconstructed images, followed by a parameter estimation procedure which iteratively computes maximum-likelihood estimates for exponential parameters of interest from the histogram. During the past year the algorithm was modified to process Super PETT I list-mode data with time-of-flight information and evaluated with data from a phantom scan (PR 23, A-8).

Circular voids of various sizes in a Lucite phantom were filled with a mixture of two radioactive tracers (^{15}O and ^{13}N) with known half-lives of decay, 124 and 599 seconds, respectively. The phantom was scanned by Super PETT I for 20 minutes and the list-mode data, consisting of over three million detected events, were then sorted by angle with time markers inserted every second. Four regions of the phantom, all containing the same concentration of isotopes, were selected as regions of interest for analysis. The two half-lives of decay were estimated for these four regions by the weighting algorithm and by the conventional method and compared to the known values. Images were reconstructed by the confidence-weighting algorithm because of the excessive amount of time required to reconstruct images with the expectation-maximization (EM) algorithm (A-5, A-6).

Thirty images were reconstructed by the confidence-weighting algorithm with each image representing about 100,000 detected events. For the weighting algorithm, the reconstructed images were used to generate weighting factors which were applied to the list-mode data for generation of histograms of 60 data values. For comparison, estimates were also obtained by the conventional method in which a nonlinear least-squares method was used to estimate parameters from time-activity curves generated by summing counts in the regions of interest in the 30 reconstructed

images. Estimates for the half-lives of decay computed by the weighting algorithm were not consistently more accurate than those computed by the conventional method. The average of the four estimates of the half-life of ^{15}O was 119 $\pm$ 13 seconds (standard deviation) for the weighting algorithm and 110 $\pm$ 3 seconds for the conventional method; for ^{13}N the average estimates were 640 $\pm$ 79 seconds for the weighting algorithm and 602 $\pm$ 26 seconds for the conventional method.

The weighting algorithm assumes that the list-mode data and the histograms can be modeled by Poisson processes. This assumption may not be valid for confidence-weighted images because of the corrections for attenuation, nonuniform sampling and random coincidences which are performed on the data before reconstruction. In addition, the confidence-weighting algorithm does not maintain non-negativity in the reconstructed images; negative numbers in the images are set to zero by the weighting algorithm. These factors may introduce errors in the computed histograms that are not described by a Poisson process and that are reflected by errors in the parameter estimates. Studies will be repeated using images reconstructed by the EM algorithm with internal corrections (A-5), when the algorithm is complete.

1. Ollinger, J. M., "Algorithms for Parameter Estimation in Dynamic Tracer Studies Using Positron-Emission Tomography," Doctoral Dissertation, Washington University, BCL Monograph No. 476, September 1986.

2. Ollinger, J. M., "Estimation Algorithms for Dynamic Tracer Studies Using Positron-Emission Tomography," IEEE Transactions on Medical Imaging, MI-6(2):115-125, June 1987.

A-8. Mapping the EM Algorithm onto Parallel Architectures

Personnel: K. R. Smith, BCL
T. J. Chaney, M.S., Computer Systems Laboratory
G. C. Johns, B.S., Computer Systems Laboratory
E. T. Macke, M.S., Computer Systems Laboratory
M. I. Miller, BCL and Electrical Engineering
C. E. Molnar, D.Sc., Computer Systems Laboratory
R. E. Morley, Jr., D.Sc., Electrical Engineering
R. E. Olson, Computer Systems Laboratory
F. U. Rosenberger, BCL and Computer Systems Laboratory
B. Roysam, BCL
P. Y. Yan, B.S., Computer Systems Laboratory

Support: RR 01380
RR 01379
ECE-8552518

We have made significant strides during the past year in identifying potential architectures for implementing the expectation-maximization (EM) image-reconstruction algorithm for positron-emission tomography (PET). Recall that the EM algorithm is a very computation-intensive image-reconstruction algorithm which is mathematically represented as:

$$\lambda^{k+1}(x) = \lambda^{k}(x)\frac{1}{N_\theta}\sum_{i=1}^{N_\theta}\int \frac{p_{\theta_i}(u|x)M_{\theta_i}(du)}{\int p_{\theta_i}(u|z)\lambda^{k}(z)\,dz}\,.$$

Based on the preliminary study [1], two algorithm partitioning methods were identified for the EM algorithm. These are the partition-by-angle and partition-by-pixel methods. Based on these two partitioning methods, the performance of the EM algorithm has been simulated or implemented on a number of different parallel architectures. The performance results are shown in Table 1 for a reconstruction problem with parameters appropriate to the Super PETT I tomograph.

Considering these performance results, we have initiated research which is designed to realize the implementation of the EM algorithm on two distinct parallel architectures. Due to performance results (see Table 1) we have chosen as our target architectures the Basic Image Manipulation Modules (BIMM) and the NCR Geometric Array Parallel Processor (GAPP).

The BIMM architecture is currently being developed in the Institute for Biomedical Computing. The programming design criteria for this parallel architecture is a partition-by-angle mapping of the EM algorithm

which attains full computational efficiency from the BIMM architecture by utilizing the extremely fast coordinate transformations inherent to the BIMM design.

Table 1. EM Algorithm Performance on Selected Architectures

Processor	Classification	Computation Time (Iteration)	Communication Time (Iteration)	Total Time (Iteration)	Convergence Time *
NCR GAPP	Systolic Array Processor	-	-	0.5 secs	1.66 mins
BIMM	Custom Image Processor	-	-	3 secs	10 mins
InMOS Transputer	Mesh MIMD Parallel Processor	6.25 secs	2.8 secs	9 secs	30 mins
Multiple TMS320C30 DSPs	Custom MIMD Parallel Processor	14.4 secs	1.7 secs	16.1 secs	54 mins
NCUBE	Hypercube MIMD Parallel Processor	12.5 secs	4.5 secs	17 secs	56 mins
Cray XMP24	Supercomputer	-	-	2.8 mins	9.5 hrs
Mercury ZIP	Pipeline Array Processor	-	-	11 mins	36.6 hrs
MassComp 55020	Fast, Sequential Processor	-	-	14 mins	46.6 hrs

* Assumes 200 iterations.

The GAPP has a massively parallel architecture which has been the focus of intense computational studies by our collaborators in Electrical Engineering. The massively parallel characteristics of the architecture enable a natural partition-by-pixel implementation of the EM algorithm. The programming design criteria for the GAPP architecture centers around thousands of simple processing elements connected in a mesh topology. By restructuring the EM algorithm for local data passage and simple processing steps [2], we have successfully mapped the EM algorithm onto a prototype GAPP architecture with a resulting performance which is quite impressive.

By partitioning the EM algorithm in two fundamentally different ways on two distinct architectures, we will provide a robust framework for studying and analyzing implementation issues associated with eventual clinical application of the EM algorithm. The implementation of the BIMM and the GAPP architectures is the first major step toward the use of the EM algorithm in a clinical environment.

The application of the GAPP to image reconstruction for emission tomography is described in (E-8). We describe below an effort to overcome the undesirable noise artifact inherent to unconstrained maximum-likelihood estimation for reconstructions implemented on the GAPP, an alternative approach to that in (A-5).

Noise-Artifact Suppression Implemented on the GAPP

Unconstrained nonparametric maximum-likelihood estimators are fundamentally inconsistent in that they produce reconstructions with a "noise artifact." We have derived constrained maximum-likelihood estimators by incorporating a rotationally-invariant version of Good's roughness penalty into the likelihood functional [3]. This leads to a set of nonlinear differential equations, the solution of which is the artifact-free reconstruction. We have mapped the nonlinear partial differential equations onto a grid via finite differences, and have shown that the resulting computations possess massive parallelism as well as locality in the data-passage. This allows for an efficient implementation on a 48-by-48 mesh-connected array of GAPP processors. We have demonstrated the smooth reconstruction of the intensity functions of Poisson point processes in two dimensions.

Basic Image Manipulation Modules

Basic Image Manipulation Modules (BIMM) are being developed to provide manipulation and display for multidimensional sampled data sets of up to 128 megabytes and four dimensions. The initial objective is a system to interactively display any planar section from four-dimensional data with resampling by bilinear interpolation in four dimensions or trilinear interpolation in two dimensions. The basic design will incorporate fixed-point calculations and provision is being made to add an additional processor for floating-point operations. The system block diagram is shown in Figure 1 and is composed of a coordinate generator, memory, processor, frame buffer, and host computer. The initial memory capacity will be 32-million 16-bit samples and will be expandable to 128-million samples when 4-megabyte dynamic random access memories (RAMs) become available. The memory is composed of 16 concurrently accessible cells with 250 nanosecond cycle time allowing 64 samples to be accessed per microsecond. The memory is organized so that the 16 samples in the neighborhood of any coordinate can be accessed concurrently and passed to the processor. A set of four busses with four-way time multiplexing is used to connect the memory cells to the processor and is designed so that the sample with a specific geometric relation to the coordinate is always transmitted on the same bus and cycle, regardless of the particular cell in which it is stored, so that the processor always receives the samples in the same order and position.

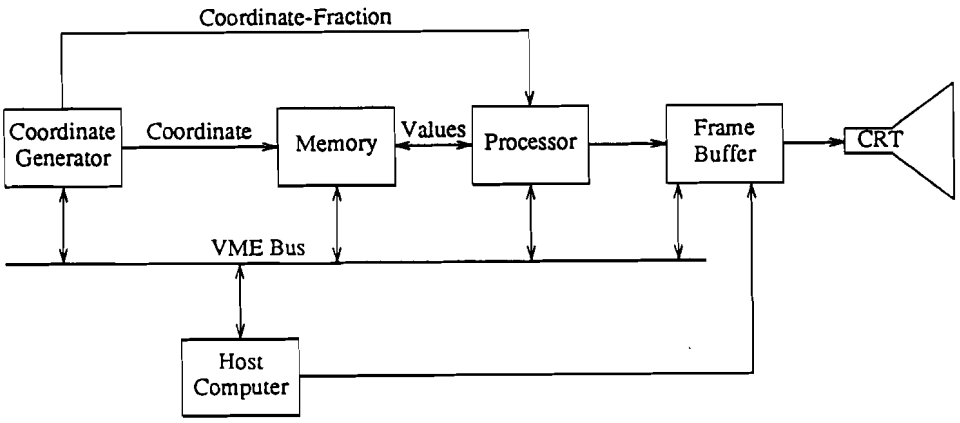

Figure 1. Image Manipulation Module block diagram.

The processor contains multipliers and coefficient memories to calculate the following function which can be used for resampling or convolution:

$$\mathrm{FOR}(u_j \mathrm{IN}\ U)\ v_j = f(u_j, S),$$

where u_j and v_j are elements of two equal-length sequences of coordinates U and V, and the function f is given by

$$f(u_j, S) = \sum_{i=0}^{N-1} S_{A(u_j,i)} K(u_j, i),$$

where S is a set of samples in the sample space defined for integer coordinate values, A is a function that selects sample values that have specific geometric positions with respect to the point specified by u_j, and K is a set of coefficients chosen for the particular function. Figure 2 shows an example of this operation for two dimensions and linear interpolation. Both the function calculation and the mapping can be carried out with up to four dimensions.

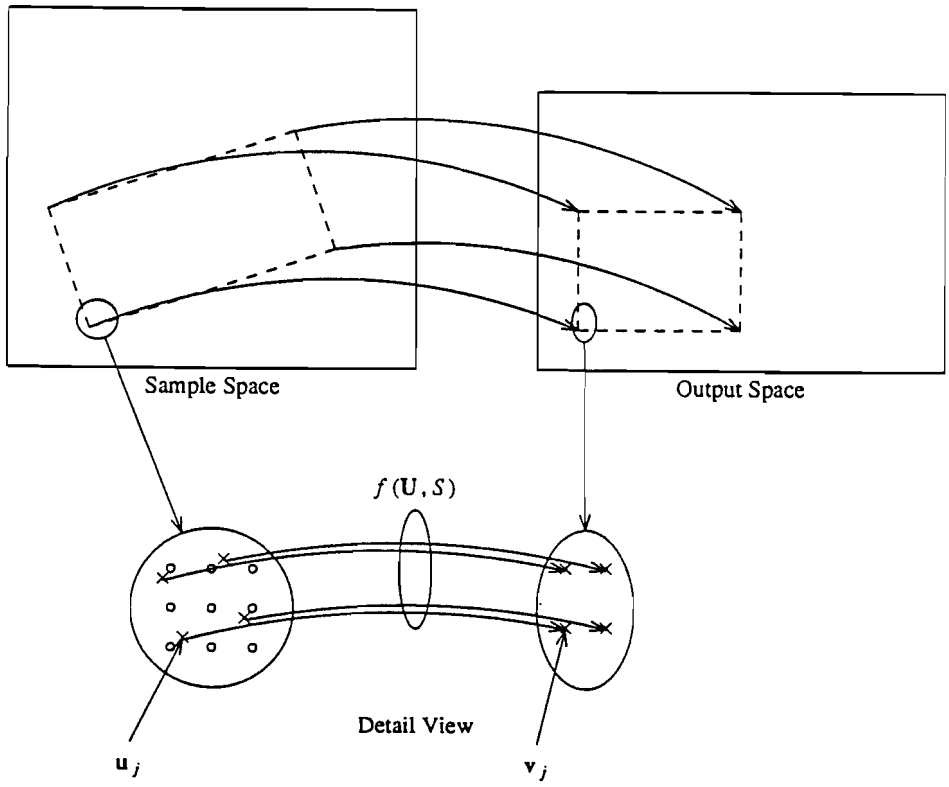

Figure 2. Coordinate mapping example.

A 4-kilobyte first-in-first-out (FIFO) buffer within the processor will store values for return to the memory for further processing or the values can be passed to the frame buffer for display. A new point can be resampled every 250 nanoseconds. The coordinate generator has sequencing and control logic to generate sequences of coordinates in up to four dimensions for addressing the memory in which the samples are stored and provides the fractional part of coordinates to the processor for selection of coefficients for interpolation or indices to select kernel coefficients for convolution.

The major addition required for PET reconstruction using the EM algorithm is floating-point computation. The coordinate generation and memory mapping is designed so that two samples with adjacent x coordinates can be combined to form a single 32-bit floating-point value. Eight 32-bit, instead of sixteen 16-bit values will then be available per 250 nanosecond cycle.

The timing estimates shown in Table 2 are for reconstruction of images from the body scanner Super PETT II, which has more quantized angles and larger arrays than Super PETT I. The estimates are based on memory

access of eight 32-bit values per 250 nanosecond cycle, expansion of convolution kernels to multiples of 8 values since the data values are accessed in groups of 8, both the processing operation and the return of results to BIMM memory, pipelined floating-point operations with the Analog Devices ADSP-3212/ADSP-3222 multiplier and arithmetic logic unit (ALU), and a FIFO in the processor so the overhead for switching from reading to writing memory will be negligible. The pipeline mode of operation in the ADSP-3222 ALU complicates the accumulation of successive values, but an algorithm has been worked out utilizing the internal registers of the ADSP-3222 to perform the accumulation for any even number of values.

Table 2. Time per Iteration with BIMM (milliseconds)	
Time for 320 angles	21980.16
Sum 400 × 400 correction array	15.00
Convolve 400 × 400 with KW kernel	45.00
Convolve 400 × 400 with KL kernel	85.00
Total time per iteration	22125.16
Time per iteration (seconds)	22.13
Time per slice (200 iterations) (minutes)	73.75
Time per 7 slices (hours)	8.60

The times shown in Table 2 do not include the initial setup, loading of data values, and harvesting of results but these will be negligible with respect to the computation time of about one hour per slice.

The memory requirements shown in Table 3 also are for reconstruction of images from the body scanner Super PETT II. They are well within the initial system capability of 16 million 32-bit samples using one-megabyte RAMs, even with expansion to store the arrays on even address boundaries for programming convenience. This ability to store the entire data requirements for a slice in the BIMM memory is important since transfers to and from the host via the VME bus are comparatively slow (about two orders of magnitude slower than the BIMM bus) and efficiencies gained by the organization and power of the BIMM calculations and memory will not be sacrificed to the requirements of frequent data transfers between the host and BIMM.

Table 3. Memory Requirements for BIMM		
Image Array	400 × 400	160,000
Angle Data	320 × 32 × 216	2,211,840
Correction Arrays	2 × 320 × 32 × 216	4,423,680
TOTAL		6,795,520

1. Smith, K. R., "Mapping the EM Algorithm for Time-of-Flight Positron Emission Tomography onto Parallel Architectures," BCL Monograph No. 484, Washington University, July 1987.

2. Barret, R. C., McCarthy, A. W., Miller, M. I., and Morley, Jr., R. E., "Gaussian Convolutions on a Massively Parallel Processor," Proceedings of the Twenty-First Annual Conference on Information Sciences and Systems, The Johns Hopkins University, Baltimore, MD, pp. 373-374, March 1987.

3. Roysam, B., Schrauner, J. A., and Miller, M. I., "Bayesian Imaging Using Good's Roughness Measure - Implementation on a Massively Parallel Processor." Proceedings of the IEEE International Conference on Acoustics, Speech, and Signal Processing, New York, 2:932, April 1988.

A-9. Preliminary Studies for a Spherical PET Instrument

Personnel: K. R. Smith, BCL
G. J. Blaine, BCL
D. G. Politte, BCL
D. L. Snyder, BCL
L. J. Thomas, Jr., BCL
J. W. Wong, BCL and Radiology

Support: RR 01380
CA 41574

Research interest in a spherical positron-emission tomograph (SPET) instrument was initiated in August of 1986. Interest evolved due to potential advantages which would be inherent in a SPET instrument. These advantages include full three-dimensional viewing, smaller resolution, improved signal-to-noise ratio, and lower dosage levels. Our preliminary research involved the study and analysis of the following topics:

1) detector geometry,
2) sampling density,
3) a three-dimensional expectation-maximization (EM) reconstruction algorithm, and
4) scatter-correction methods.

In the past year we have drawn the preliminary study to a conclusion, in the sense that each of the above research topics has been thoroughly investigated and a unified reconstruction theory has been developed and simulated. Specifically, each stage of the SPET reconstruction process has been simulated with very encouraging results. The first stage of the simulation required an accurate computer model of the SPET instrument based on the detector geometry. Relying on geodesic mathematics and a computed three-dimensional sampling density, a suitable

detector geometry was simulated which represents an actual model of a potential SPET instrument. The second stage of the simulation used this model in an effort to test and analyze the three-dimensional reconstruction algorithm and also various scatter-correction techniques. The results of this two-stage study were encouraging on two counts: 1) the three-dimensional algorithm reconstructs images in a robust manner, and 2) with appropriate correction algorithms, image degradation due to scatter should not prohibit the development of a SPET instrument for regions of interest as large as twenty centimeters.

Our findings and results from the literature suggested a scatter-correction technique which consists of simply including the scatter effects in the measurement-error kernel of the EM reconstruction algorithm. This development promotes a unified three-dimensional reconstruction algorithm for SPET. We have incorporated this reconstruction algorithm in a set of studies designed to simulate the actual data collection involved in the SPET scanner. Using Monte Carlo techniques, the positron emission, photon flight (scatter and attenuation included), and photon detection processes were simulated. Our three-dimensional algorithm was then used to reconstruct the simulated phantom. The results indicate promise for the development of an actual SPET instrument.

The future of this research relies heavily on improvements in detector technology. Specifically, the feasibility of building a SPET instrument requires a modestly priced crystal/photomultiplier unit with high resolution, reasonable energy discrimination characteristics, and a small, flexible packing density.

A-10. A New Approach to ML Image Reconstruction Based on a Parameterized ML Solution

Personnel: D. L. Snyder, BCL and Electrical Engineering
T. J. Schulz, M.S., Electrical Engineering

Support: RR 01380
ECS 8407910

The approach we have used for estimating the spatial concentration of a radiotracer with the method of maximum-likelihood estimation treats the problem as a nonparametric, or infinite-dimensional, one. This approach uses no knowledge of the form of the maximum-likelihood estimate. On the other hand, it has been shown by others in the literature (in one dimension) that when there are no measurement errors and when a Gaussian-kernel sieve is used to stabilize the estimate, the maximum-likelihood estimate is in the finite-parameterized form of a weighted sum of displaced Gaussian densities, where the weighting and displacement constants are undetermined. We have extended this result for the case when there are Gaussian-distributed measurement errors, as with PET reconstructions, and

Gaussian-kernel sieves and Gaussian-resolution kernels are used for stabilization. A study is now underway to compare the estimated activity distribution obtained when the finite-dimensional, parameterized form of the estimate is used to that when this form is not used.

B. Quantitative Imaging: Ultrasonic Tissue Characterization

One of the obstacles to the application of tissue characterization to the myocardium is the effect of phase-cancellation. Phase cancellation occurs across the face of a finite piezoelectric element when the incoming waves have been distorted in such a way that both a "peak" and a "valley" are present at the face of the transducer at the same instant, and thus partially cancel each other. The result is a reduced signal, when there actually was a larger acoustic field present. The phase fronts of the scattered or reflected acoustic waves can become distorted by passing through any irregularly shaped or inhomogeneous medium. This distortion can very easily occur as acoustic radiation propagates through the chest wall, is scattered or reflected, and returns to the transducer. Because tissue characterization relies upon the quantitative characteristics of the received signal, errors may be introduced into the values if phase cancellation is present. This is especially true when a goal is to compensate for the anisotropic nature of media such as myocardium. The relative alignment of the muscle fibers results in stronger backscattered signals when insonified perpendicular to the fibers than when insonified along their axes. In order to approach the goals of myocardial tissue characterization, including the quantitative estimation of the physical state of the tissue from ultrasonic parameters, reliable measurements must be made of backscattered ultrasonic fields. Accordingly, this Laboratory has investigated some differences between the phase-sensitive and phase-insensitive processing of signals from a two-dimensional pseudo-array of small, point-like piezoelectric receivers, as described below.

Another goal of myocardial tissue characterization is the discrimination between normal myocardium and muscle impaired as a result of ischemia. A parameter that is useful for the characterization of a localized region of tissue is the so-called cyclic variation of backscatter over the heart cycle. It has been observed that the cyclic variation is blunted and delayed in time relative to the QRS complex of the ECG in zones of ischemia, as compared with regions of normal tissue. We report on an algorithm for quantitatively estimating the magnitude and delay of a given cyclic variation signal.

B-1. Phase-Sensitive and Phase-Insensitive Quantitative Tissue Characterization Using a Two-Dimensional Pseudo-Array

Personnel: M. R. Holland, BCL
M. R. Kaufmann, BCL
J. G. Miller, BCL

Support: RR 01362
HL 40302

Introduction

In this section we report on the progress being made with the use of a two-dimensional pseudo-array arrangement to measure the energy contained in a "backscattered" ultrasonic field. The hypothesis underlying this work is that more reliable estimates of the energy contained in the backscattered field should result in improved estimates of parameters such as frequency dependent backscatter. Because piezoelectric transducers and transducer arrays are susceptible to phase-cancellation effects, resulting measurements may underestimate the amount of energy contained in a backscattered field. The goal of this research is to compare phase-sensitive and phase-insensitive processing of experimental data. Experimental results are compared for the same scattered field due to a distribution of glass-bead scatterers embedded in gelatin measured with or without intervening phase-distorting media and using several methods of focusing. Ultrasonic parameters investigated include the average power, the difference between phase-insensitively and phase-sensitively derived power spectra, and the slope of the apparent "backscatter" transfer function as a function of frequency. This research represents a further step toward the larger goal of experimentally determining the trade-off between resolution and quantitative measurements of backscatter resulting from the choice of phase-sensitive or phase-insensitive imaging.

Methods

The experimental arrangement used to measure the scattered ultrasonic field was similar to that used previously in this laboratory [1-3]. It consists of a 0.5-inch diameter, 5 MHz center-frequency, piezoelectric transmitting transducer focused at the surface of a glass-bead phantom. A two-dimensional pseudo-array receiver arrangement is achieved by translating a planar 5-MHz center-frequency transducer apodized to 1 mm in diameter (with a Styrofoam plate) in a 13 × 13 grid pattern with 1-mm separation between adjacent grid positions. The receiving pseudo-array was centered at a scattering angle of 160° ("backscatter") with respect to the direction of the incident ultrasonic beam. Determination of various ultrasonic parameters which describe the "backscattered" ultrasonic field were made off-line using phase-sensitive and phase-insensitive analyses (described below) of the rf waveforms obtained at each position of the receiver array. The glass-bead scattering phantom used consisted of a distribution of solid glass beads ranging from 63 to 158 μm in diameter embedded in gelatin. (This scattering phantom does not necessarily mimic the ultrasonic properties of specific tissue.)

The effects of introducing phase-distorting media in front of the receiving array on the phase-insensitively and phase-sensitively derived parameters were investigated. The phase-distorting media used in this investigation consisted of a polyethylene wedge or grooved plate. The polyethylene wedge was a 38.1 mm by 38.1 mm square with a thickness of 5.44 mm at one edge and tapering linearly to a thickness of 1.27 mm at the opposite edge. The polyethylene grooved plate was a 38.1 mm by 38.1 mm square plate whose thickness was 3.15 mm except for two grooves of 3.18 mm in width milled at the center of the plate. The depth of one of the grooves was 0.46 mm and that of the other was 0.79 mm. Each of the phase-distorting plates, placed, in turn, directly in front of the two-dimensional pseudo-array approximately 3 mm in front of the apodized receiving transducer. Care was taken to align the plates parallel to the plane of the two-dimensional pseudo-array.

Several focusing schemes were applied to the ultrasonic data acquired by the two-dimensional pseudo-array. The focusing schemes employed were: no focusing, geometric point focusing, and "correlation focusing." For no focusing, no time shifts were applied to the recorded rf waveforms obtained at each position in the pseudo-array. Thus, the unfocused data represents what a planar two-dimensional receiver array would measure. Geometric point focusing the array was achieved by applying the appropriate time delays to each of the rf waveforms recorded at each position of the pseudo-array. These time delays were determined by calculating the time-of-flight for each position in the array to a point located a distance of 101.6 mm (distance between pseudo-array and phantom) from the center position of the array along a line perpendicular to the plane of the array. A third method of focusing the receiving array was that of "correlation focusing." The "correlation focusing" method employed is similar to the adaptive beam-forming techniques used by K. V. Gurumurthy and R. M. Arthur [4]. In this method, the time shifts applied to the rf waveforms recorded at each position of the pseudo-array were calculated by determining the correlation coefficients obtained for a range of shifts applied to the rf waveform at a given array position when correlated with the rf waveform recorded at the center array position. The time shift which produces the largest correlation coefficient was then used as the "correlation focusing" time shift for a given array position.

Both phase-sensitive and phase-insensitive analyses were applied to the rf data collected with the two-dimensional pseudo-array. For phase-sensitive analysis of the data the individual rf waveforms recorded at each of the array positions were focused as desired, summed together, and averaged, thus producing an average rf waveform for the array. The average waveform was then processed further by determining the average power or the power spectrum inside a time-gated region. Phase-insensitive analysis was achieved by applying the desired focusing to the rf waveform obtained at a given array position and then determining the average power or power spectrum in a time gated region of the (focused) rf trace recorded at that particular array position. The average power or power spectrum for each of the array locations was summed and averaged to give the respective phase-insensitive values for the array as a whole.

In the results reported below, the "backscattered" field investigated was that field contained in a 4.0 μsec gate which included the front surface and the region immediately behind the front surface of the glass-bead phantom. The signal loss effects of the polyethylene phase-distortion plates were removed by compensating for the measured losses through polyethylene. The "backscattered" ultrasonic field was measured for 10 statistically independent sites in the glass-bead phantom. For each ultrasonic parameter subsequently determined, the results from each independent phantom site were averaged and the mean value and its corresponding standard error were reported.

Results

The results of the measurements of the average power, the difference between phase-insensitively and phase-sensitively derived power spectra, and the slope of the apparent "backscatter" transfer function are described below for the several combinations of focusing schemes and intervening phase-distorting media.

Average Power:

The values of the average power contained in the scattered ultrasonic field, determined phase-sensitively and phase-insensitively for the various phase-distorting intervening media, and focusing schemes are displayed in Figure 1, panels a) b) and c). Figure 1a) shows the phase-insensitively and phase-sensitively determined values of the average power for the three focusing schemes when there was no phase-distorting plate between the scattering phantom and the receiving pseudo-array. The error bars show standard errors. The phase-insensitively determined values are larger in magnitude than the phase-sensitively determined values and do not appear to be significantly dependent on focusing scheme used. Conversely, the phase-sensitively determined values appear to be very dependent on the focusing scheme used. As illustrated in Figure 1a), the difference between the phase-insensitively and phase-sensitively determined values is the greatest for the unfocused case (14.0 dB) and is smaller for the point-focus (5.6 dB) and "correlation focused" (4.6 dB) cases.

Figure 1b) shows the phase-insensitively and phase-sensitively determined values of the average power for the three focusing schemes when the wedge-shaped phase-distortion plate was between the scattering phantom and the receiving pseudo-array. (Compensation for the effects of the signal loss due to the attenuation and insertion loss of the polyethylene wedge phase-distortion plate was carried out prior to the generation of Figure 1b).) This figure shows similar features to those described above. The phase-insensitively determined values do not depend strongly on the focusing technique employed whereas the phase-sensitively determined values do. The phase-insensitive values are larger in magnitude than those for phase-sensitive detection, with a 13.0 dB difference for unfocused, 12.6 dB difference for point-focused, and 4.4 dB difference for "correlation focused." Contrasting this figure with Figure 1a) reveals that the magnitude of the point-focused phase-sensitively determined value is not as

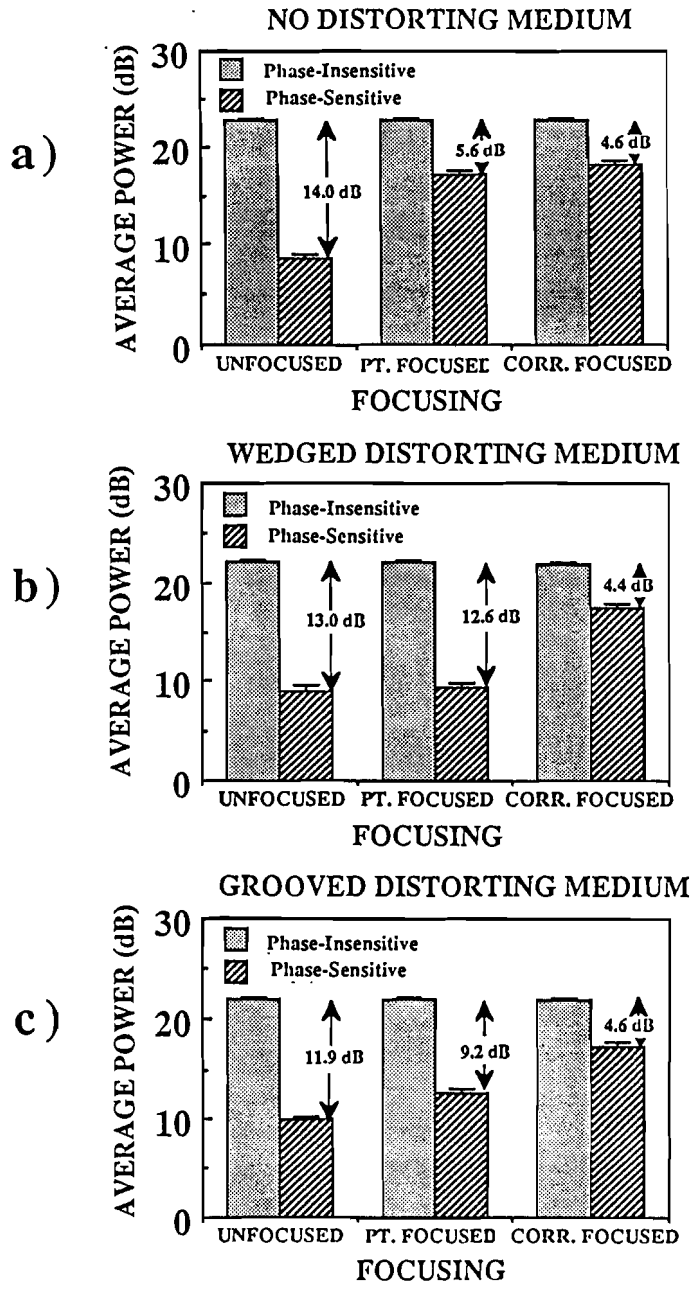

Figure 1. Average power in a 4.0 μsec gate.

large as that in the case of no phase-distorting intervening medium. This may be due to the fact that the phase-distorting wedge distorts the phase-fronts of the scattered field but the focusing employed is that for an undistorted field emanating from a point 101.6 mm away. Thus the focusing shifts employed to the rf data do not focus the data properly and phase-cancellation effects are still present.

The values of the phase-insensitively and phase-sensitively determined average power for the case of the intervening grooved polyethylene phase-distortion plate are shown in Figure 1c). (Here again the signal-loss effects of the phase-distortion plate have been removed as described previously.) The phase-insensitively derived values are larger in magnitude than the phase-sensitively derived values for all focusing techniques employed, and the phase-insensitively determined values do not depend strongly on focusing technique used whereas the phase-sensitively derived values do. The differences between the phase-insensitively derived values and the phase-sensitively derived values show a dependence upon focusing scheme used, much in the same manner as that discussed for the wedge phase-distortion plate above. The differences in this case are 11.9 dB for the unfocused case, 9.2 dB for the point-focused case, and 4.6 dB for the "correlation focused" case.

A comparison of the phase-insensitively and phase-sensitively determined values of the average power illustrated in Figures 1 a), b), and c) for all combinations of phase-distorting media and focusing schemes yields the following conclusions. First, the phase-insensitively determined values of the average power do not depend upon the focusing scheme used or intervening phase-distorting media, whereas, in general, the phase-sensitively determined values do. Second, comparing only the phase-sensitively "correlation focused" derived values, we see that although they are smaller in magnitude than the corresponding phase-insensitively derived values, they do not appear to depend strongly upon the intervening phase-distorting media as do the point-focused, phase-sensitively derived values.

Differences in Power Spectra:

Typical phase-insensitively and phase-sensitively derived power spectra of the "backscattered" ultrasonic field over the useful bandwidth of 3 to 7 MHz are shown in Figure 2. These power spectra correspond to the "backscattered" field measured with no intervening phase-distorting media and with no focusing applied. These spectra illustrate many features common to power spectra for all combinations of phase-distorting media and focusing scheme employed. The phase-insensitively derived power spectrum is larger in magnitude than the corresponding phase-sensitively derived power spectrum for all frequencies. In addition, the phase-insensitively derived spectrum varies more smoothly with frequency and has smaller site-to-site variations (error bars show standard errors) than the phase-sensitively derived spectrum.

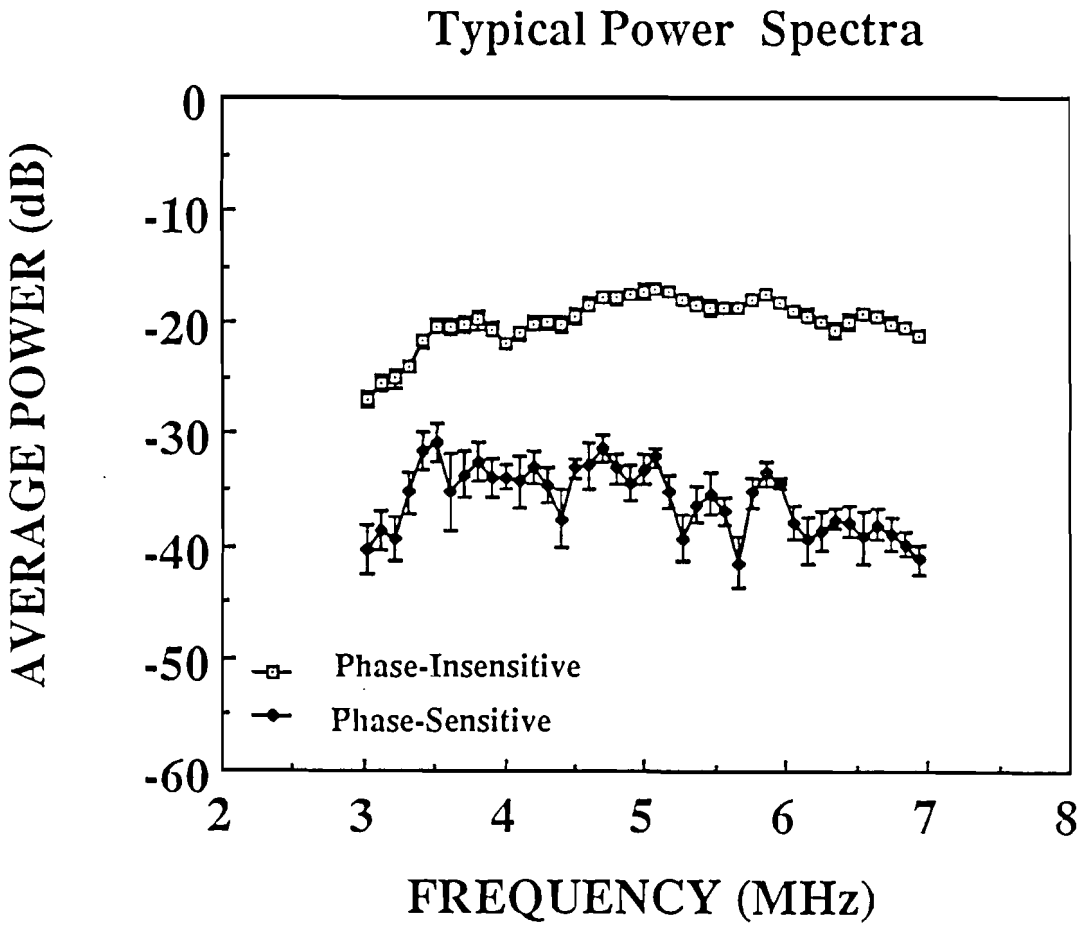

Figure 2. Typical phase-insensitively and phase-sensitively derived power spectra.

Figures 3, 4, and 5 illustrate the difference between the phase-insensitively derived power spectrum and the phase-sensitively derived power spectrum when different phase-distorting media are introduced between the glass-bead phantom and the receiver pseudo-array. Figure 3, panels a), b), and c) show the difference between the phase-insensitively and phase-sensitively derived power spectra for the unfocused, point focused, and "correlation focused" cases respectively when there was no intervening phase-distorting medium. In Figure 3a) the difference between the spectra appears to increase approximately monotonically as a function of frequency from a value of approximately 12 dB at the low frequencies to a value of approximately 20 dB at the higher frequencies. This may be due to the shorter wavelengths being more susceptible to phase-cancellation effects. Figure 3, panels b) and c) show an almost constant difference of approximately 6 dB between the spectra over the useful bandwidth.

Figure 4, panels a), b), and c) show the differences in power spectra when the wedge-shaped phase-distortion plate was placed between the scatterers and the pseudo-array for the cases of no focusing, point focusing, and "correlation focusing," respectively. (The effects of the signal-loss due to the wedge shaped polyethylene plate have been removed.) Figure 4, panels a) and b) show a frequency dependence for the difference between spectra similar to that observed in Figure 3a). Again this is presumably due to more phase-cancellation occurring at the higher frequencies (shorter wavelengths). Point focusing at 101.6 mm does not improve the result, presumably because the ultrasonic field is distorted relative to the way it was when there was no intervening phase-distorting medium (just as described above for Figure 1b)). The difference in spectra for the "correlation focused" case is similar to that shown in Figure 3c), where the difference is approximately constant over the useful bandwidth.

Figure 5, panels a), b), and c) show the differences in power spectra when the grooved phase-distortion plate was present with no focusing, point focusing, and "correlation focusing," respectively. The results shown in Figure 5a) are similar to those illustrated in Figures 3a), 4a), and 4b), i.e., the difference shows an approximately monotonic increase with frequency starting at approximately 12 dB for the low frequencies and increasing to approximately 20 dB at the higher frequencies. The difference illustrated in Figure 5b) shows that the values are approximately constant over the useful frequency range, but with a value (approximately 12 dB) greater than the frequency independent values found above (Figures 3b), 3c), and 4c)). The difference illustrated in Figure 5c) again shows the relatively frequency independent value of approximately 6 dB.

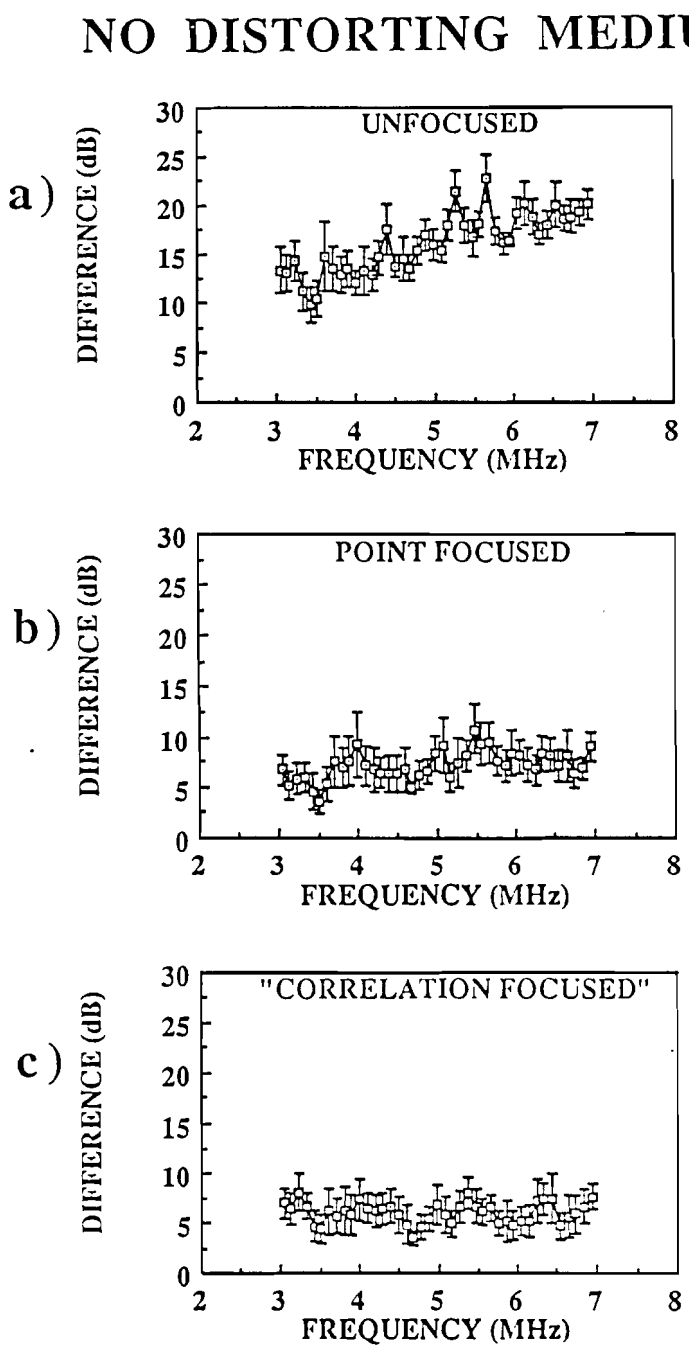

Figure 3. Difference between phase-insensitively and phase-sensitively derived power spectra with no intervening phase-distorting medium.

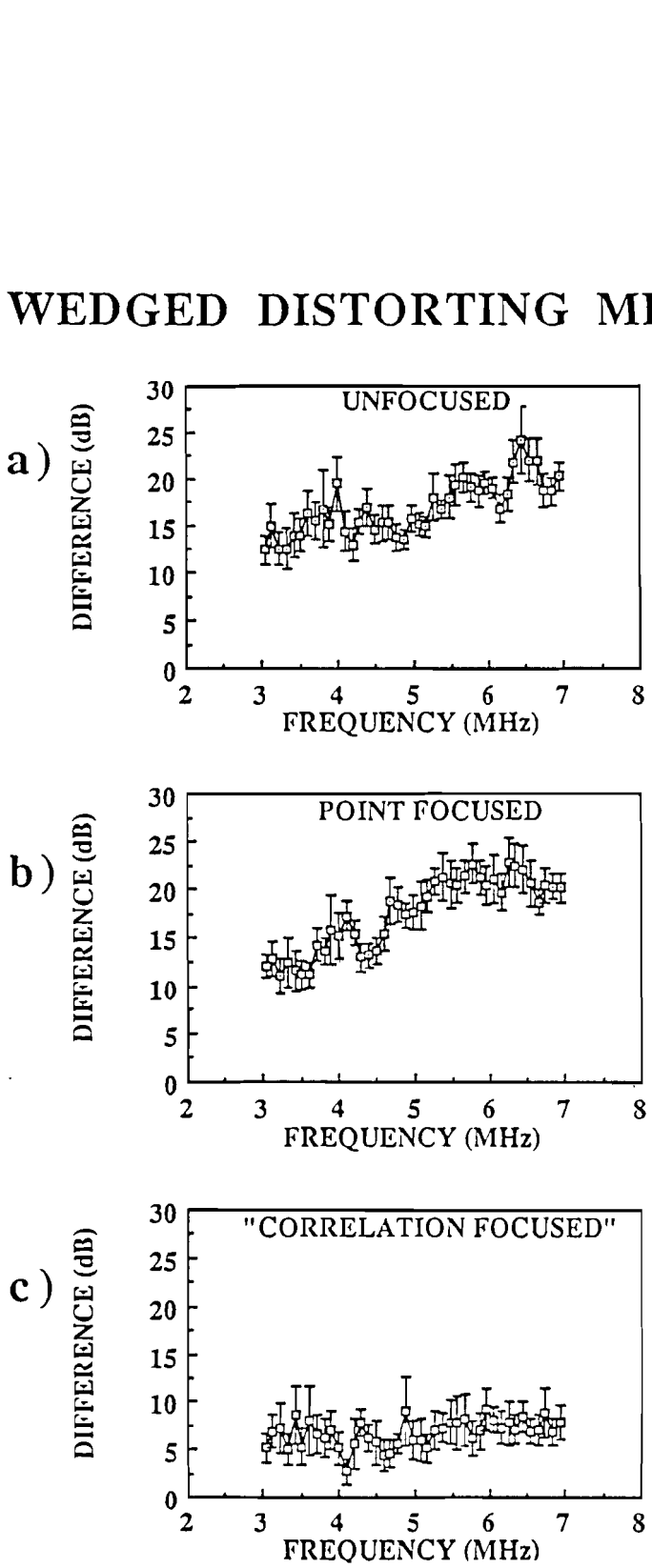

Figure 4. Difference between phase-insensitively and phase-sensitively derived power spectra with wedge plate phase-distorting medium.

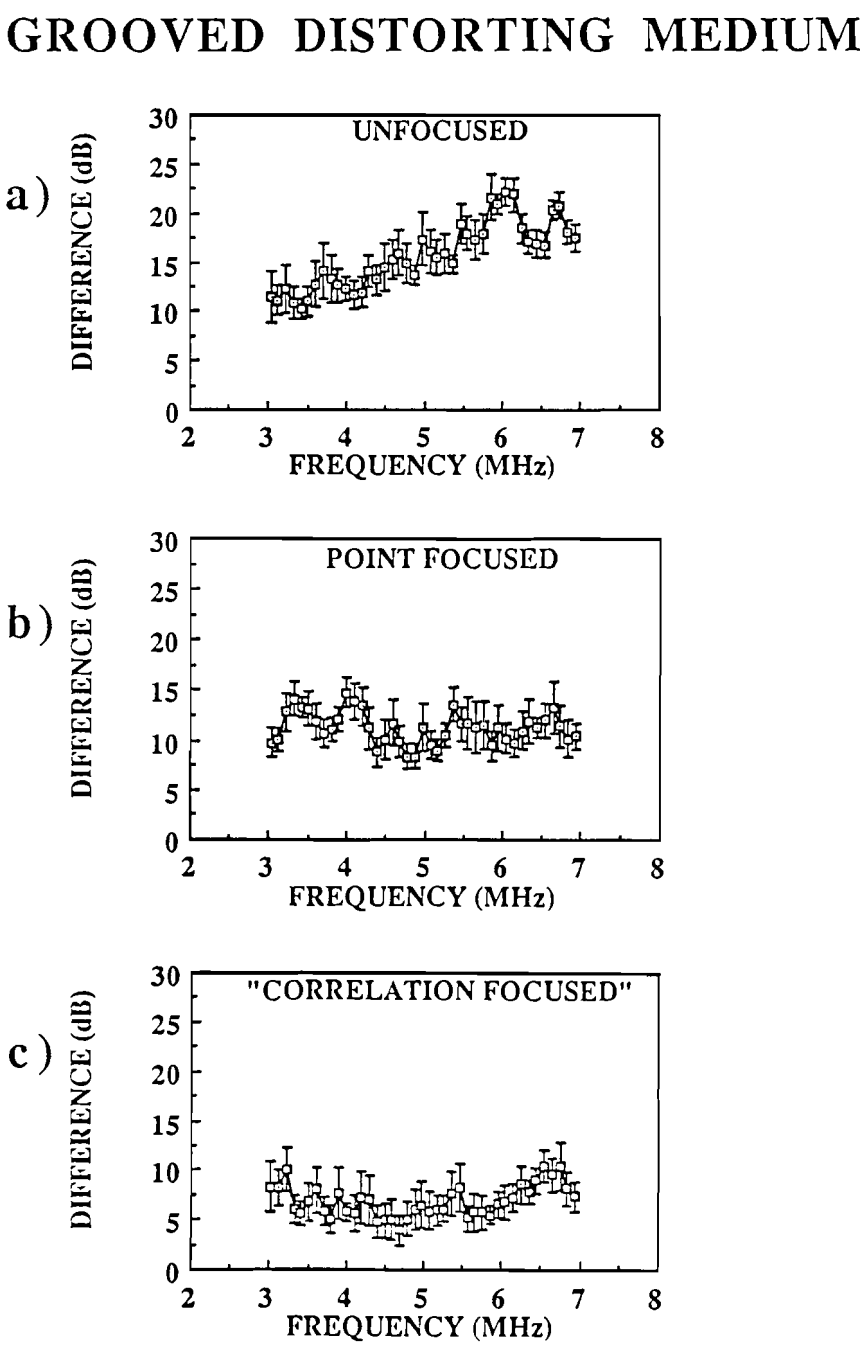

Figure 5. Difference between phase-insensitively and phase-sensitively derived power spectra with grooved plate phase-distoring medium.

Frequency Dependence of Apparent "Backscatter" Transfer Function:

The apparent "backscatter" transfer function is obtained by removing the system-dependent electromechanical responses from the measured power spectrum [5-7]. This is accomplished by subtracting (on a logarithmic scale) a calibration spectrum obtained from the specular echo off of a stainless-steel reflector from the power spectrum of the scattered field due to the glass-bead scatterers. The apparent "backscatter" transfer function contains effects due to the scattering medium, the attenuation of the medium, and the volume interrogated. The phase-insensitively and phase-sensitively derived apparent "backscatter" transfer functions discussed here were determined by subtracting the phase-insensitively or phase-sensitively derived calibration spectrum from the corresponding phase-insensitively or phase-sensitively derived power spectrum of the "backscattered" ultrasonic field. This procedure was carried out for the power spectra determined with all of the combinations of focusing schemes and phase-distorting media described above. The frequency dependence of the apparent "backscatter" transfer function was determined by determining the slope of a linear least-squares fit to the apparent "backscatter" transfer function versus log(frequency) data. The slope represents the frequency dependence cf the apparent "backscatter" transfer function.

Figure 6 shows typical apparent "backscatter" transfer functions derived phase-insensitively and phase-sensitively as a function of frequency. These particular phase-insensitively and phase-sensitively derived apparent "backscatter" transfer functions are those obtained from unfocused data with no phase-distorting media. In general the phase-insensitively derived apparent "backscatter" transfer function is more smoothly varying with frequency and has smaller error bars than the corresponding phase-sensitively derived apparent "backscatter" transfer function. Figure 7 illustrates the values of the frequency dependence, f^n, of the apparent "backscatter" transfer function when either phase-insensitive [panel a)] or phase-sensitive [panel b)] analysis is used. In Figure 7a) the frequency dependence of the phase-insensitively derived apparent "backscatter" transfer functions for all combinations of focusing schemes and intervening phase-distorting media are relatively constant. It can be seen in Figure 7b) that the measured frequency dependence of the phase-sensitively derived "backscatter" transfer function is very much dependent upon the focusing scheme employed or the phase-distorting medium used.

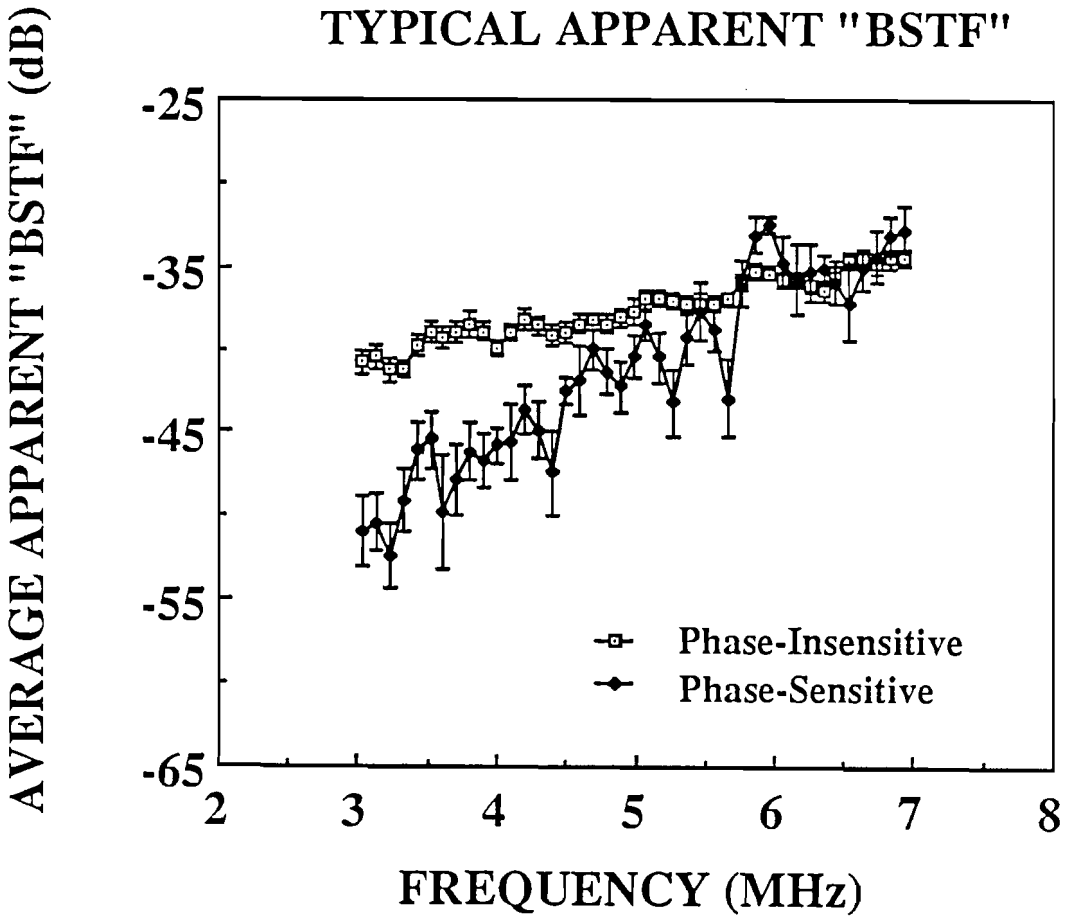

Figure 6. Typical phase-insensitively and phase-sensitively derived apparent "backscatter" transfer function ("BSTF").

a)

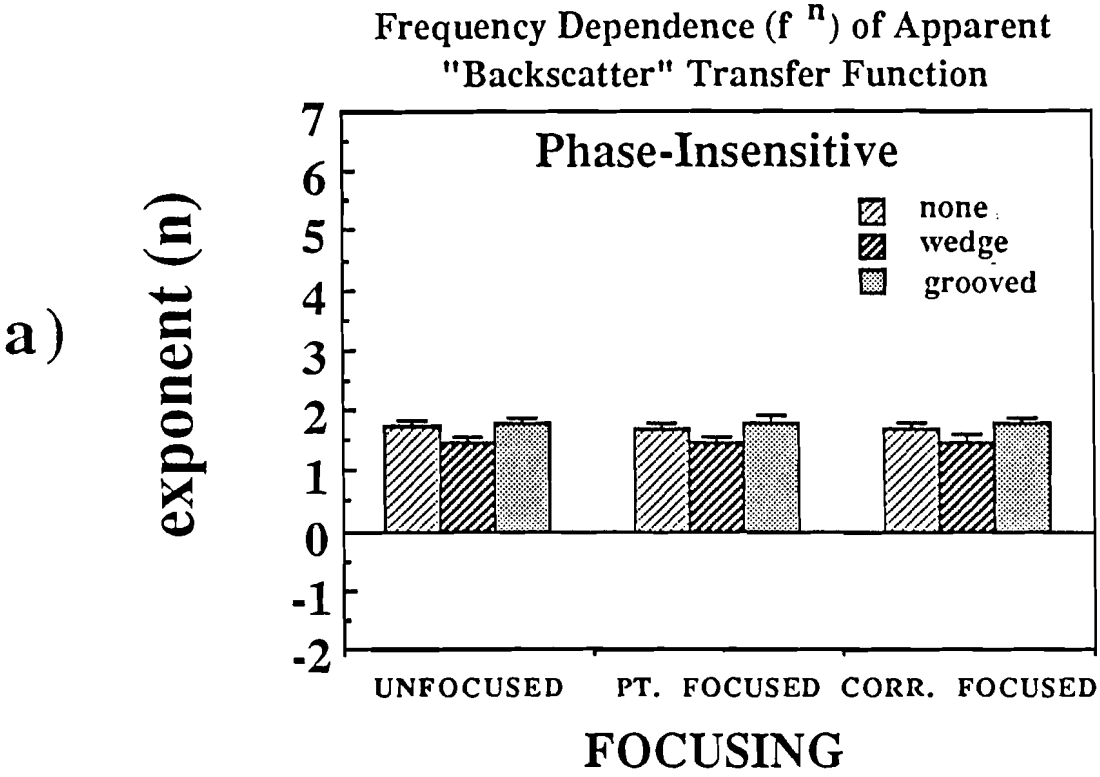

b)

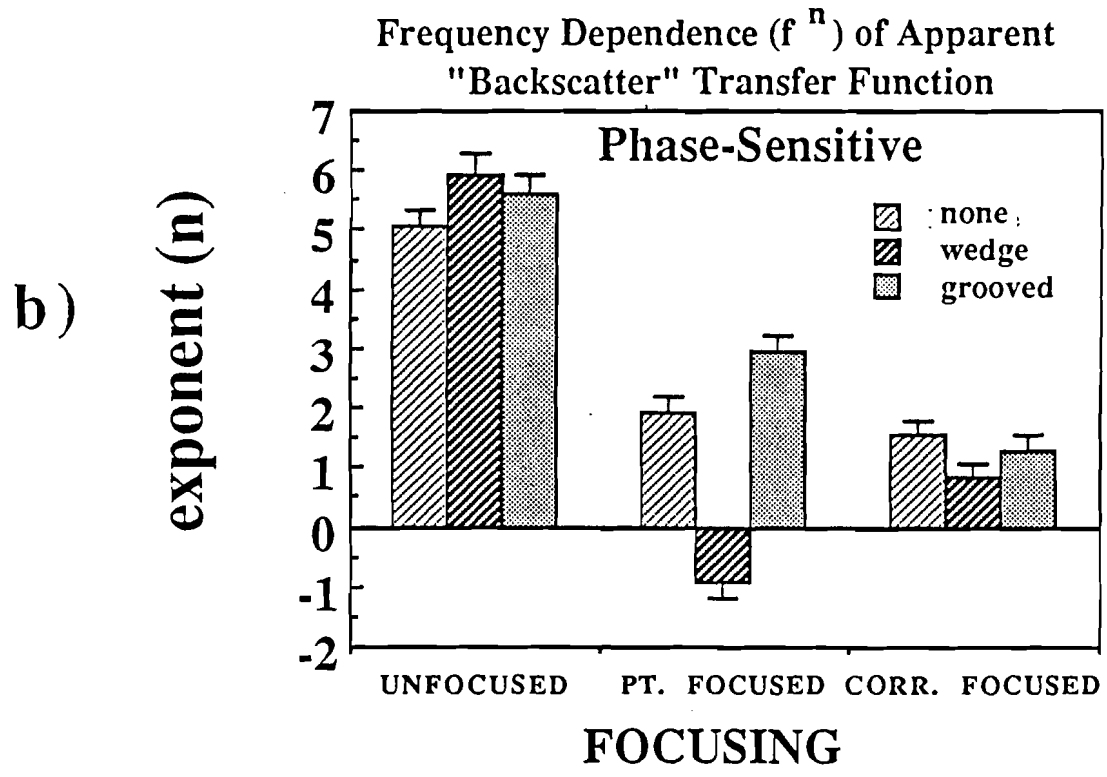

Figure 7. Frequency dependence, f^n, of the phase-insensitively and phase-sensitively derived "backscatter" transfer functions.

Summary:

The results presented above seem to indicate that the phase-insensitively derived values are not as strongly affected by the focusing scheme employed or intervening phase-distorting media used as the phase-sensitively derived values. Consequently, phase-insensitive detection may improve estimates of ultrasonic parameters to be used for diagnosis based on quantitative tissue characterization.

1. Johnston, P. H. and Miller, J. G., "A Comparison of Backscatter Measured by Phase-Sensitive and Phase-Insensitive Detection," Proceedings of the 1985 IEEE Ultrasonics Symposium, IEEE Catalog No. 85CH2209-5, pp. 827-831, 1985.

2. Johnston, P. H. and Miller, J. G., "Phase-Insensitive Detection for Measurement of Backscattered Ultrasound," IEEE Transactions Ultrasonics, Ferroelectrics, and Frequency Control, UFFC-33:713-721, 1986.

3. Johnston, P. H., "Phase-Insensitive Detection and the Method of Moments for Ultrasonic Tissue Characterization," Washington University, St. Louis, MO, August 1985 (Ph.D. Dissertation).

4. Gurumurthy, K. V., "Adaptive Pulse-Echo Imaging for Quantitative Tissue Characterization," Washington University, St. Louis, MO, August 1981 (Ph.D. Dissertation).

5. Sigelmann, R. A. and Reid, J. M., "Analysis and Measurement of Ultrasonic Backscattering from an Ensemble of Scatterers Excited by Sine-wave Bursts," Journal of the Acoustical Society of America, 53:1351, 1973.

6. O'Donnell, M. and Miller, J. G., "Quantitative Broadband Ultrasonic Backscatter: An Approach to Non-Destructive Evaluation in Acoustically Inhomogeneous Materials," Journal of Applied Physiology, 52:1056-1065, 1981.

7. Miller, J. G., Perez, J. E., Mottley, J. G., Madaras, E. I., Johnston, P. H., Blodgett, E. D., Thomas, III, L. J., and Sobel, B. E., "Myocardial Tissue Characterization: An Approach Based on Quantitative Backscatter and Attenuation," Proceedings of the 1983 IEEE Ultrasonic Symposium, IEEE Catalog No. 83CH1947-1, pp. 782-793, 1983.

B-2. A Practical Algorithm for the Automated Determination of the Magnitude and Time Delay ("Phase") of the Cyclic Variation of Ultrasonic Integrated Backscatter from Myocardium

Personnel: G. A. Mohr, BCL
B. Barzilai, M.D., Medicine
J. G. Miller, BCL
J. E. Perez, M.D., Medicine
B. E. Sobel, M.D., Medicine
Z. Vered, Medicine

Support: RR 01362
HL 17646
HL 40302

Introduction

We have previously reported that normal myocardium exhibits a cardiac cycle-dependent variation of integrated backscatter [1] that quantitatively reflects regional, intramural myocardial contractile function [2], and that changes in the cyclic variation of integrated backscatter reflect myocardial dysfunction in patients with idiopathic cardiomyopathies [3] and remote infarcts [4]. With the development [5] of an ultrasonic imaging system having real-time integrated backscatter capabilities, the eventual clinical utility of integrated backscatter measurements has become evident.

However, the complexity of the mechanisms responsible for the cyclic variation of integrated backscatter, the variability between subjects, and the experimental inaccuracies that are unavoidable in closed-chest measurements performed *in vivo* cause the measured integrated backscatter data to exhibit a variety of qualitative differences from an "ideal" shape. For example, the duration of the contraction portion of the curve is often noticeably less than the duration of the relaxation part. These differences, although they do not prevent identification of the characteristic cyclic variation, often make difficult the precise measurement of the variation.

Our group has previously used the peak-to-peak amplitude of a sine wave, found either by least-squares fitting in the time domain or equivalently as twice the amplitude of the first Fourier component [6], as an estimate of the magnitude of cyclic variation. Others have also recently reported [7] results of canine cyclic variation measurements in this fashion. In addition, we have found that the phase of these approximately sinusoidal variations (with respect to either the electrical or hemodynamic activity of the heart) [2] also characterizes the contractile performance of the myocardial tissue. These approaches work well for variations which are approximately sinusoidal, but for more general forms of the variation, they consistently underestimate the peak-to-trough magnitude of the variation, because any cyclic but non-sinusoidal variations are ignored. In our later clinical investigations [3,4], the features of the integrated backscatter data that

were relevant to the cyclic variation were identified manually in each graph by an experienced cardiologist before the peak-to-trough magnitude of the cyclic variation and the time delay between the QRS-complex of the electrocardiograph (ECG) and the nadir of the systolic "trough" were estimated.

Our closed-chest measurements of myocardial integrated backscatter have demonstrated a wide variety of variation shapes under different measurement conditions. Figure 1 shows integrated backscatter measurements from normal and abnormal zones of canine myocardium. Panel a) shows a representative result from a zone of normal myocardium. In contrast the cyclic variation is essentially absent from the measurement shown in panel b), obtained from a zone of tissue affected by acute coronary occlusion. Panel c), from a zone less severely affected by occlusion, demonstrates a blunted cyclic variation intermediate to those of panels a) and b). It also shows some of the difficulties that we have occasionally encountered, such as the presence of a significant amount of random noise and systematic variations of integrated backscatter that are not directly related to the heart cycle. The objective of this work was to develop an algorithm for the analysis of cyclic variation robust enough to provide reasonable estimates of the cyclic variation even in difficult cases.

Description of the Algorithm

We developed an approach that focuses only on the similarities between the cyclic variation of measured data and a simple, objective model. By maximizing the likenesses between the data and an idealized model of cyclic variation, the undesirable effects of systematic deviations from the model can be reduced. Our approach allows the use of an extremely simple model, with parameters that directly correspond to the straightforward measures of cyclic variation (magnitude and time delay) that we used in our clinical studies.

The analysis algorithm uses only the measured integrated backscatter data and three parameters determined independently from the ECG (a time origin corresponding to the first QRS-complex, the average systolic interval, T, (onset of R wave to termination of T wave) and the average period, T) as input. First, a model function of the cyclic variation appropriate for each data trace is formulated. The model function is assigned a lesser value for a time equal to T (corresponding to relatively less backscatter during contraction) and a greater value for the remainder of the heart cycle. This template is cyclicly repeated at the average cardiac period, with an arbitrary magnitude for the cyclic variation. The model function is then smoothed using a binomial coefficient [8] low-pass digital filter. The smoothed model is then offset to have zero mean over the cardiac period. For consistency, the data are also identically low-pass filtered. The data set is truncated at both ends, retaining only points from an integral number of periods. The last step in conditioning the data is to remove both the mean and any overall sloping trend that may be present by subtracting a best-fit straight line (determined using the standard least-squares technique) from the smoothed, truncated data. Figure 2 shows the results of these steps for an example data set and its corresponding model function. Filtering the data reduces the relative

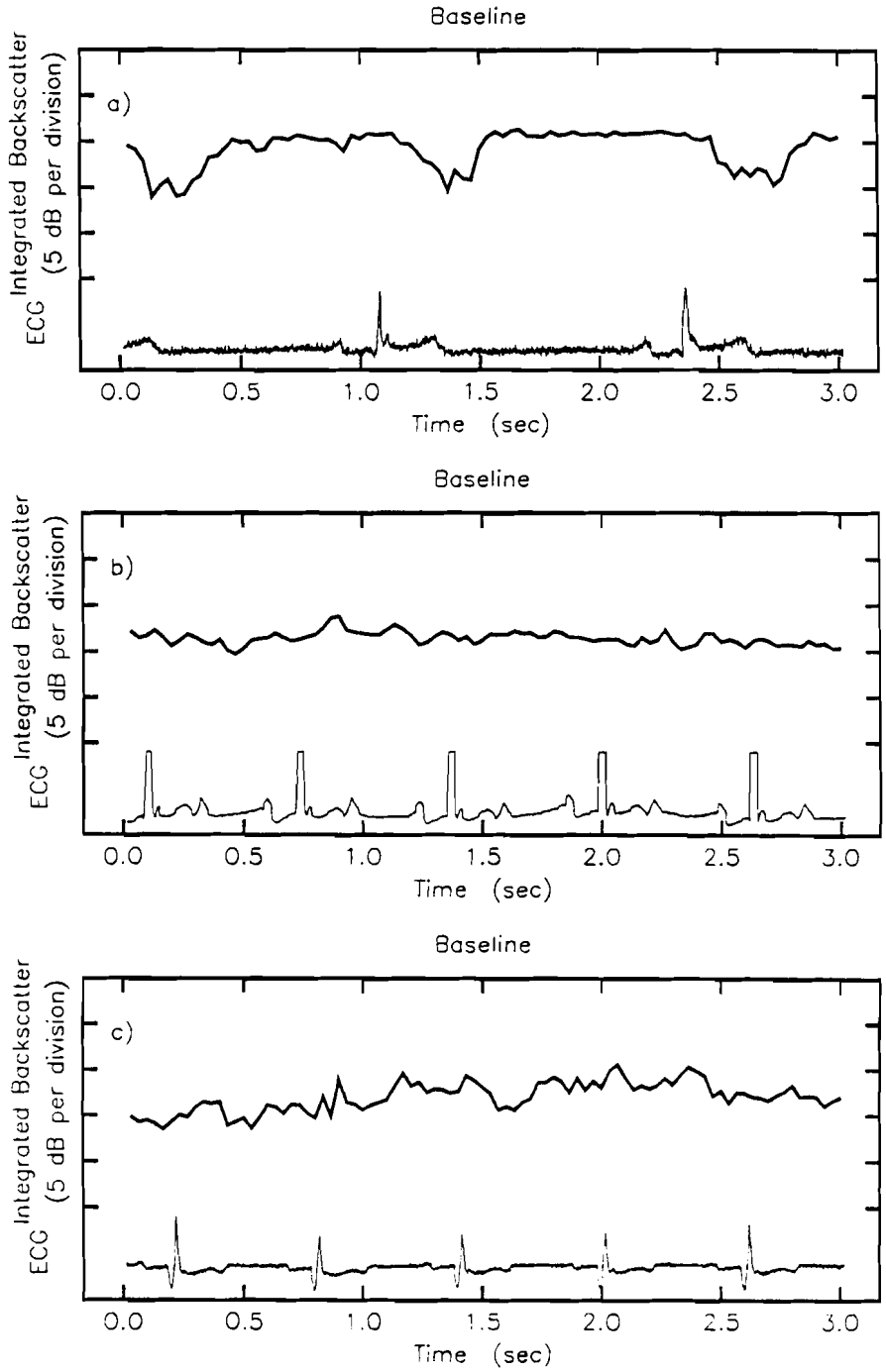

Figure 1. Measurements obtained from zones of canine myocardium obtained during a study of the effects of acute ischemia. Panel a) shows a typical measurement from a normal zone of myocardium. In panel b), from a zone affected by acute coronary occlusion, the cyclic variation has essentially vanished. Panel c), a measurement from a zone of tissue less severely affected by occlusion, demonstrates an appreciable cyclic variation, although the magnitude is blunted with respect to that of normal myocardium. The measurement in panel c) is also contaminated by a significant amount of noise and shows a long term trend probably caused by respiratory variations.

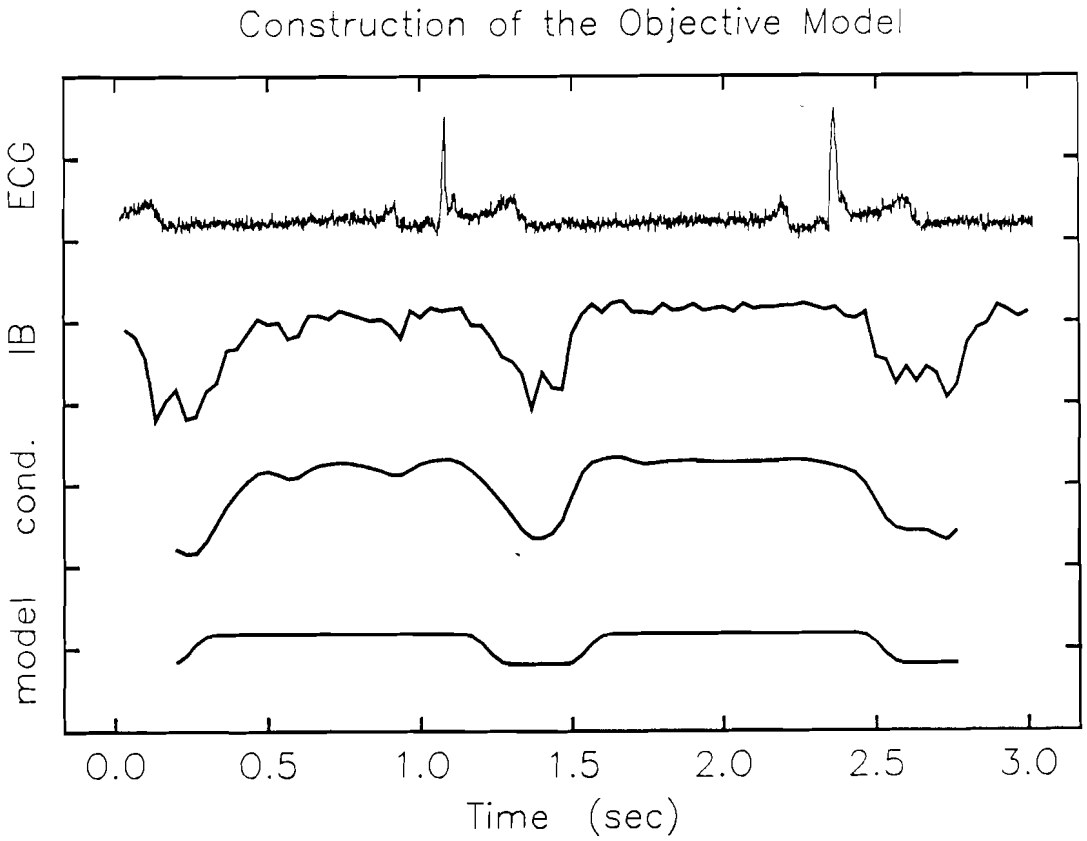

Figure 2. An example of the construction of the objective model. At the top is the ECG. Next are the original data and the conditioned data after smoothing, truncation, and removal of the overall trend. At bottom is the delayed model after temporal alignment of the model with the variations in the data.

amount of high-frequency noise, while truncation ensures that a discrete Fourier transform can represent the true behavior of both data and model in the frequency domain.

Because the local contraction may not be in phase with global systole, a delay time T is added between the time origin (the QRS-complex) and the onset of the contraction portion of the model. The best value for the delay is determined by maximizing, with respect to T, the similarity between the model M and the conditioned data D. This similarity is expressed as the (unnormalized) cross-correlation

$$\frac{1}{N} \sum_{i=0}^{N-1} M_i \, D_i,$$

where N is the number of conditioned data points.

The final model function includes the delay T which maximizes the cross-correlation, as shown in Figure 3. T is also used to estimate the delay of the cyclic variation, as

$$\text{delay} = T + 1/2T,$$

so that the reported estimate of delay corresponds to the interval between the QRS-complex and the nadir of the cyclic variation.

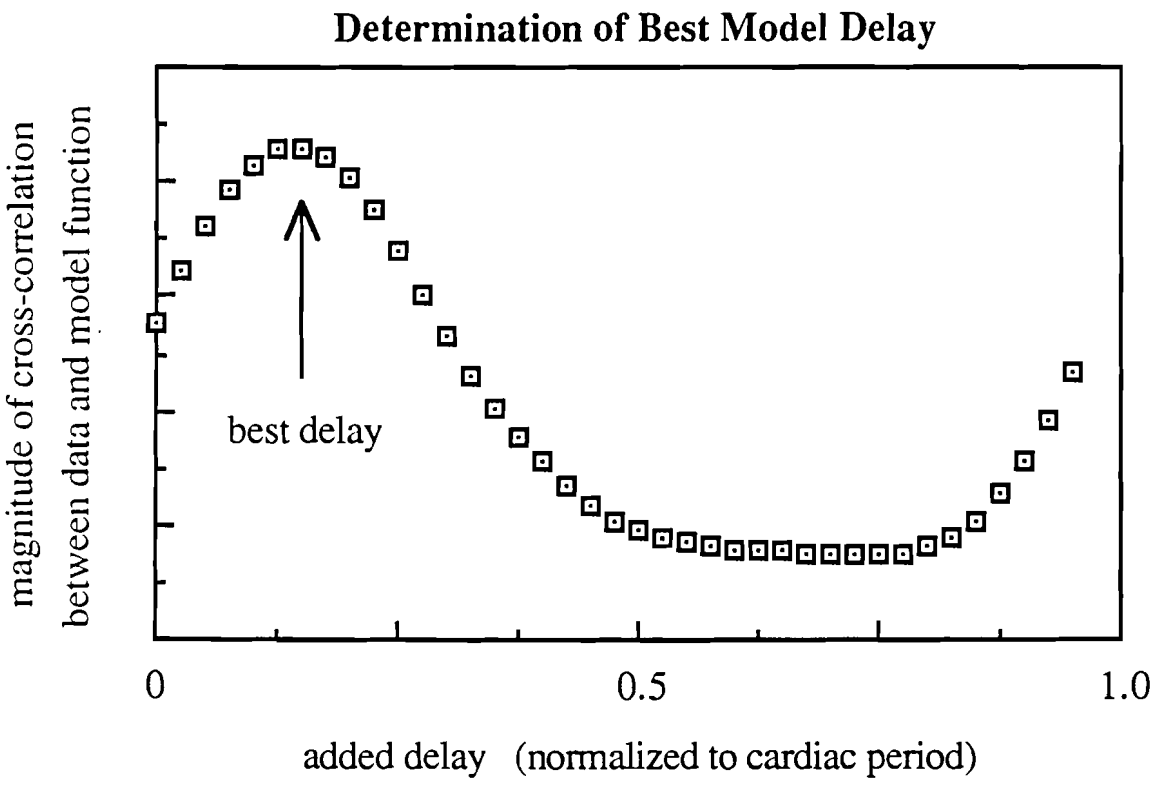

Figure 3. The similarity or cross-correlation between the conditioned data and the model is shown as a function of the delay between the QRS-complex of the ECG and the onset of the systolic interval of the model. The correlation is approximately periodic and shows a clear maximum at T_{best}, the optimal delay. T_{best} is used to calculate the delay estimate.

The magnitude of cyclic variation is then estimated using a selective power comparison technique. Because the model function exactly spans an integral number of periods, it carries power at only the frequencies f_k which are multiples of the fundamental frequency (which

corresponds to one heart cycle). For example, if three periods are present, the value of the Fourier transform and the corresponding power needs to be calculated only at the frequencies f_k with index positions k = 3,6,9, ... in the discrete transform. At the appropriate harmonic frequencies f_k, the power content P_k of the model and the conditioned data are found by summing the squares of the real and imaginary parts of the discrete Fourier transform. Any harmonic frequencies with poorly-behaved spectral power values are then excluded from further consideration. For the model, the requirement is sufficient power at the frequency in question (more than 1% of the power at the maximal model harmonic). For the data spectrum, any harmonics with power content greater than that of the fundamental are rejected. At each of the appropriate frequencies, the power of the data and model are compared by calculating the ratios $R_k = P_k(D)/P_k(M)$, where P_k denotes spectral power at frequency F_k, and dependencies on D and M refer to data and model. The overall power similarity ratio S is the average of the single frequency power ratios weighted by the corresponding power content of the data, calculated as

$$S = \frac{\sum_k R_k P_k(D)}{\sum_k P_k(D)}$$

where k includes only the well-behaved frequencies. The overall power similarity ratio S can be considered as a measure of the power gain involved in a transformation between data and model. The estimate of the magnitude of cyclic variation is thus simply

$$\text{magnitude} = \sqrt{S} \times \text{magnitude of model variation.}$$

The result of analyzing an example measurement is illustrated in Figure 4.

Results

To assess the ability of the algorithm to provide reasonable estimates of the cyclic variation on a variety of variation shapes, 246 integrated backscatter measurements obtained in an earlier study [9] with our real-time integrated backscatter imaging system from 10 closed-chest canine subjects were studied before, during, and after acute coronary occlusion. Originally the data were graphically analyzed by two observers (one of whom was an experienced cardiologist) who formed a consensus opinion on the shape of the cyclic variation and used movable cursors superimposed on a computer display of the data to estimate the average magnitude and delay of cyclic variation. The accompanying ECGs were also examined, and the necessary time events (Q and end-T points) recorded. Subsequently, the data were analyzed using the automated procedure, again yielding magnitude and delay estimates for each trace. To normalize for varying heart rates, all delays were expressed as unitless ratios of (delay/T).

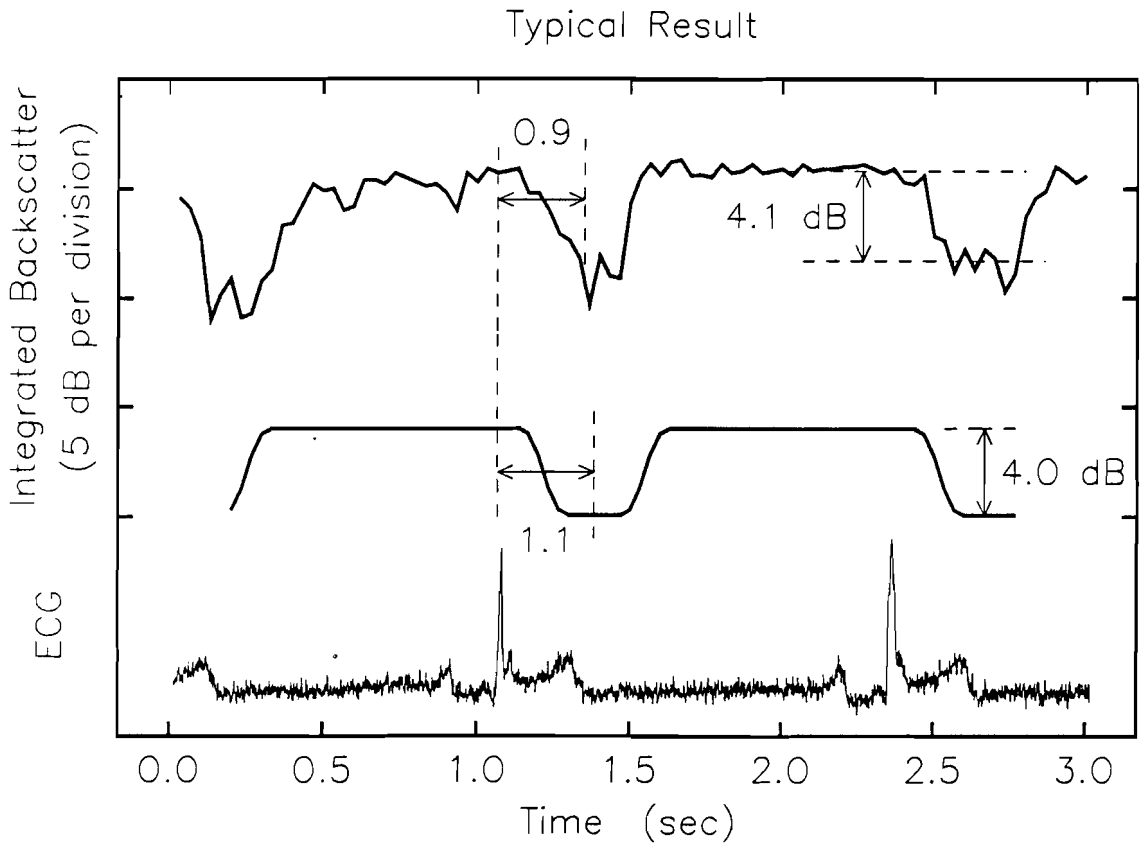

Figure 4. A comparison of data and final objective model. The unnormalized delay estimates were 294 ms (manual) and 367 ms (automated).

Figure 5 shows a comparison of the manually estimated delay of cyclic variation with the delay estimated by the automated procedure. In 242 of 246 cases, the model adequately represented the observed variation, and the delay of the objective model was in good agreement with the manually estimated delay of the observed variation. A linear fit of the form y = ax was performed for these delay estimate comparison data, giving

automated estimate = 1.07 manual estimate.

The best slope is near unity, and the correlation coefficient r = 0.94, for a wide range of delay values. The standard error of the slope estimate was ±0.01.

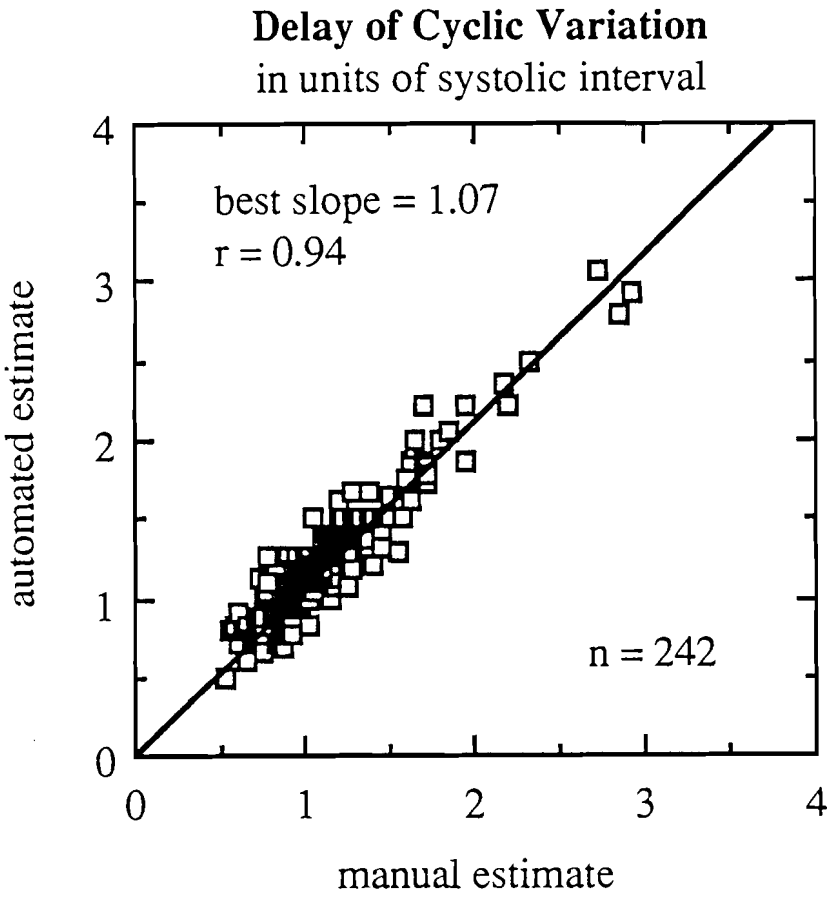

Figure 5. A comparison of the delay estimate expressed as the unitless ratio of delay to systolic interval obtained both manually and by the automated method. In 242 of 246 cases the model adequately represented the observed delay, and the agreement between the manual and automated procedures is excellent.

A comparison of the magnitude index and the manually estimated magnitude for all 246 cases is shown in Figure 6. The best-fit line is

automated estimate = 0.88 manual estimate.

Again, the best slope is near unity, with r = 0.88, for a wide range of magnitudes. The standard error of the slope estimate was again ±0.01. Although the magnitude comparison is not quite so striking as the delay comparison, we believe that this is an acceptable result, considering that in our experience the magnitude of cyclic variation is more difficult to estimate using the manual method than is the delay.

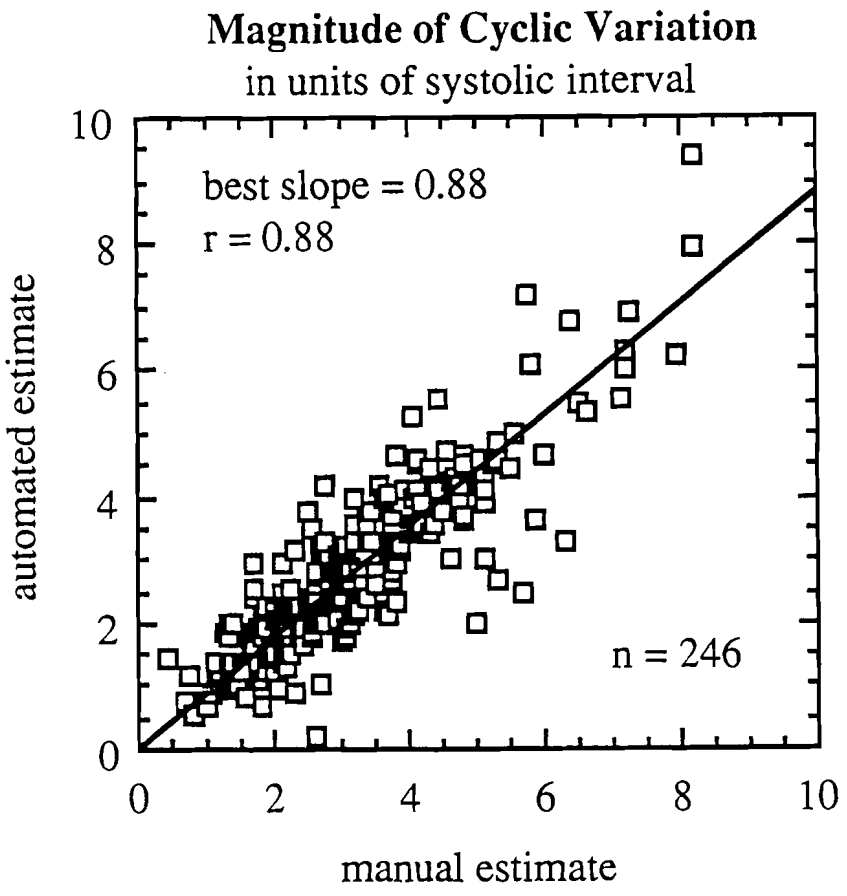

Figure 6. A comparison of the magnitude estimates obtained both manually and automatically for the same 246 measurements compared in Figure 5. For the most part, the two methods produce similar results despite the fact that the manual estimation of the magnitude is often difficult.

Discussion

Despite the variety of integrated backscatter variations that have been observed and the simplicity of the algorithm described here, the reliable analysis of cyclic variation by an automated algorithm appears feasible, given the promising results obtained so far. The algorithm produces in most cases reasonable estimates of the cyclic variation that can be interpreted in a straightforward manner. In addition, the algorithm is relatively simple, and requires only modest computing power for effective implementation. Although it is anticipated that in clinical use the resulting estimates of cyclic variation would be reviewed by a physician (perhaps by graphical comparison of the objective model and the integrated backscatter data), the availability of an automated analysis procedure might significantly affect the ease with which real-time integrated backscatter imaging could be used routinely, thus enhancing the potential clinical utility of ultrasonic cardiac tissue characterization as a non-invasive diagnostic tool.

1. Madaras, E. I., Barzilai, B., Perez, J. E., Sobel, B. E., and Miller, J. G., "Changes in Myocardial Backscatter Throughout the Cardiac Cycle," Ultrasonic Imaging, 5:229-239, 1983.

2. Wickline, S. A., Thomas, III, L. J., Miller, J. G., Sobel, B. E., and Perez, J. E., "The Dependence of Myocardial Ultrasonic Integrated Backscatter on Contractile Performance," Circulation, 72:183-192, 1985.

3. Vered, Z., Barzilai, B., Mohr, G. A., Thomas, III, L. J., Sobel, B. E., Shoup, T. A., Melton, H. E., Miller, J. G., and Perez, J. E., "Quantitative Ultrasonic Tissue Characterization with Real-Time Integrated Backscatter Imaging in Normal Human Subjects and in Patients with Dilated Cardiomyopathy," Circulation, 76:1067-1073, 1987.

4. Vered, Z., Mohr, G. A., Gessler, C., Wickline, S. A., Barzilai, B., Wear, K. A., Miller, J. G., and Perez, J. E., "Ultrasonic Integrated Backscatter Characterization of Remote Myocardial Infarction in Man," Circulation, 76:IV-44, 1987 (abstract).

5. Thomas, III, L. J., Barzilai, B., Wickline, S. A., Gessler, C. J., Sobel, B. E., Perez, J. E., and Miller, J. G., "Real-time Two-Dimensional Imaging Based on Quantitative Integrated Backscatter," Ultrasonic Imaging, 8:36, 1986 (abstract).

6. Mottley, J. G., Glueck, R. M., Perez, J. E., Sobel, B. E., and Miller,, J. G., "Regional Differences in the Cyclic Variation of Myocardial Backscatter that Parallel Regional Differences in Contractile Performance," Journal of the Acoustical Society of America, 76:1617-1623, 1984.

7. Sagar, K. B., Rhyne, T. L., Warltier, D. C., Pelc, L., and Wann, L. S., "Intramyocardial Variability in Integrated Backscatter: Effects of Coronary Occlusion and Reperfusion," Circulation, 75:436-442, 1987.

8. Marchand, P. and Marmet, L., "Binomial Smoothing Filter: A Way to Avoid Some Pitfalls of Least Squares Polynomial Smoothing," Review of Scientific Instrumentation, 54:1034, August 1983.

9. Vered, Z., Barzilai, B., Courtois, M., Mohr, G. A., Wear, K. A., Shoup, T. A., Melton, H. E., Ludbrook, P. A., Sobel, B. E., Miller, J. G., and Perez, J. E., "Detection of Myocardial Ischemia and Reperfusion in Intact Dogs with Real-Time Ultrasonic Backscatter Imaging," Journal of the American College of Cardiology, 11:5A, 1988 (abstract).

B-3. Estimation of Background Velocity

Personnel: R. M. Arthur, BCL and Electrical Engineering
S. R. Broadstone, BCL and Electrical Engineering

Support: RR 01362
Washington University

Imaging with a focused transducer array is clearly affected by the choice of background velocity used during that reconstruction. Berkhout and coworkers [1] showed that increasing the value of the assumed phase velocity produced a lateral extension of the focused image of a point. They demonstrated that a minimum-entropy measure of the data had a peak when the correct velocity was chosen on reconstruction. We studied variations in high-precision images of point-like scatterers that occur when the background velocity assumed on reconstruction from linear-array signals differed from the actual background velocity of the medium to investigate the average and variance of the images as measures for selecting correct background velocity.

Point-Spread Functions

The simulated response of each element of a given array was calculated at a point in a homogeneous, non-attenuating medium with a background velocity of 1500 m/s assuming element motion was uniform using the method of Lockwood and Willette [2]. Backscattered signals were calculated at each receiver in response to all transmitters by convolving its response with itself and all other responses, yielding the complete dataset.

We formed images for three drive functions at the face of each transmitting transducer, as shown in Figure 1. In addition to an impulse we inferred a drive function by measuring the pulse response of a single

element of a 32-element array of 1.1 x 13 mm transducers separated by 1.4 mm, at a range of 50 mm. Pulse amplitude and duration were about 60 volts and 140 ns, respectively. The pulse was shaped so that pulse energy was nearly constant in the 2-7 MHz band. We deconvolved the measured response using the calculated impulse response for a uniform piston of the same size. The 3-cycle sine wave with a half-sine envelope is a simple function that approximates the inferred drive. To match the actual array, a center frequency of 3.5 MHz was used in this waveform.

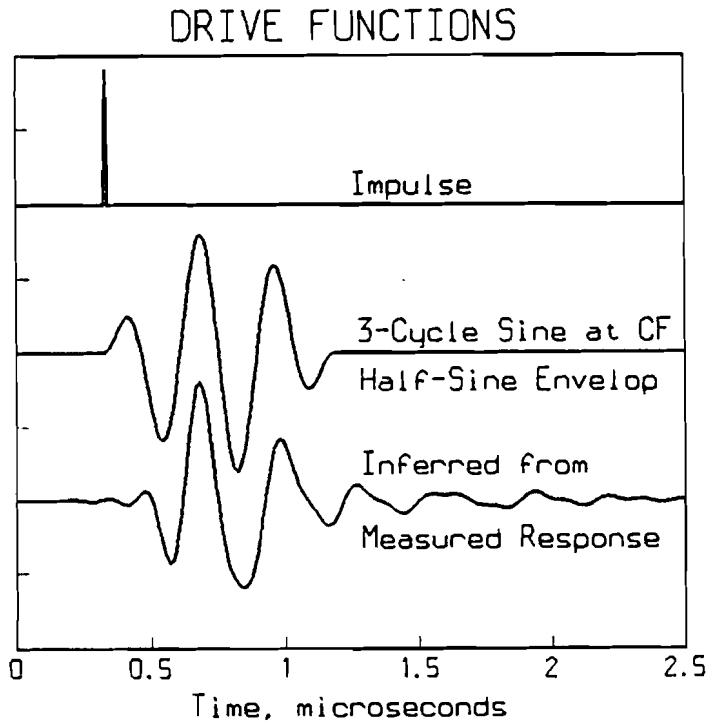

Figure 1. Drive functions at the face of each transducer used in the simulation of backscattered signals.

Point images for the simulated 32-element array for which the drive function which was a sine wave with a half-sine envelope are shown in Figure 2. The 3.8 x 3.8 mm view region is the extent of a 512 x 512 pixel image formed from backscattered signals sampled at 100 MHz. The 100 MHz sample rate was necessary to avoid significant aliasing of the impulse response of individual transducer elements. Background velocities below, equal to, and above that used to calculate the backscattered signals were assumed on reconstruction for the images in Figure 2. The 1420 m/sec point-spread function curves away from the array and is noticeably smeared laterally compared to the image with the correct background velocity on reconstruction (1500 m/sec). When background velocity was overestimated (1580 m/sec), the point-spread function curved towards the array, but like the underestimated images was smeared laterally.

Although the peak value of the image changed with assumed background velocity, we investigated measures that characterized the entire image. The average value did not change significantly; the variance did. We therefore summarized the effect of velocity error on reconstruction by considering the variance of the point-spread functions for all three drive functions given in Figure 1. Figure 3a shows the variance, σ^2, as a function of assumed background velocity.

$$\sigma^2 = \frac{1}{512^2} \sum_{i=1}^{512} \sum_{j=1}^{512} p(i,j)^2 - \mu^2 ,$$

where p(i,j) was the pixel value at a given location in each 512 x 512 image and μ was the average value of the image. The variance of the images for each of the drive functions is shown relative to its peak, which occurred when the assumed reconstruction velocity was correct (1500 m/sec).

Images of Wires in the AIUM Test Object

To check predictions of the point-spread functions we generated complete-dataset, synthetic-focus images of a water-filled AIUM 100 mm test object using an array which had the same geometry assumed in the simulations. Sample rate for the image of the six central wires shown in Figure 4 was 12.5 MHz, so that the 512 x 512 image described a 30 mm x 30 mm region of interest. Actual wire diameter is about 0.75 mm. We isolated a wire, which was about 50 mm from the array, for wlhich background velocity of 1520 m/s produced an image with maximum variance. As was observed for the simulated point-spread functions, when the background velocity was underestimated then the wire image became smeared laterally and curved away from the array; whereas reconstruction at an overestimated velocity caused lateral smearing with curvature toward the array.

The variance of the isolated wire image as a function of background velocity assumed on reconstruction is shown in Figure 3b. Like the variance of the point-spread functions, the variance of the isolated wire image decreased from a maximum (near 1520 m/sec) with either lower or higher reconstruction velocity like the variance of the point-spread functions.

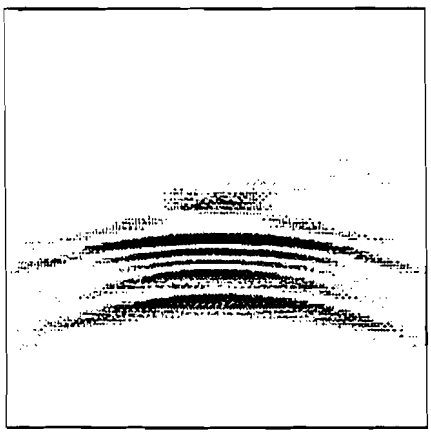

assumed velocity = 1420 m/s

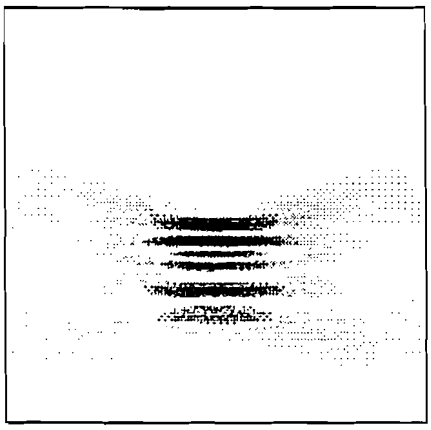

assumed velocity = 1500 m/s

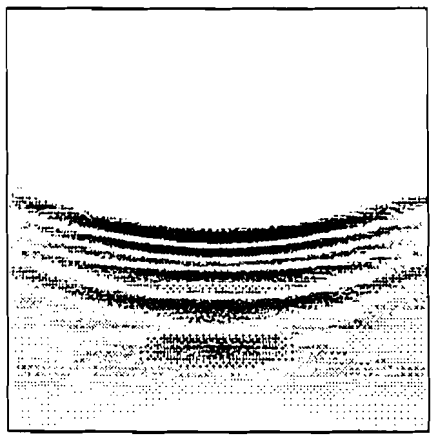

assumed velocity = 1580 m/s

Figure 2. Point-spread function at a range of 50 mm on the propagation axis of a simulated 3.5 MHz, 32-element linear array (1.1 x 13 mm elements). Actual background velocity was 1500 m/s. The simulated array was driven by three cycles of a 3.5 MHz sine wave with a half-sine envelope. The point scatterer is shown as viewed from above; image size is 3.8 x 3.8 mm.

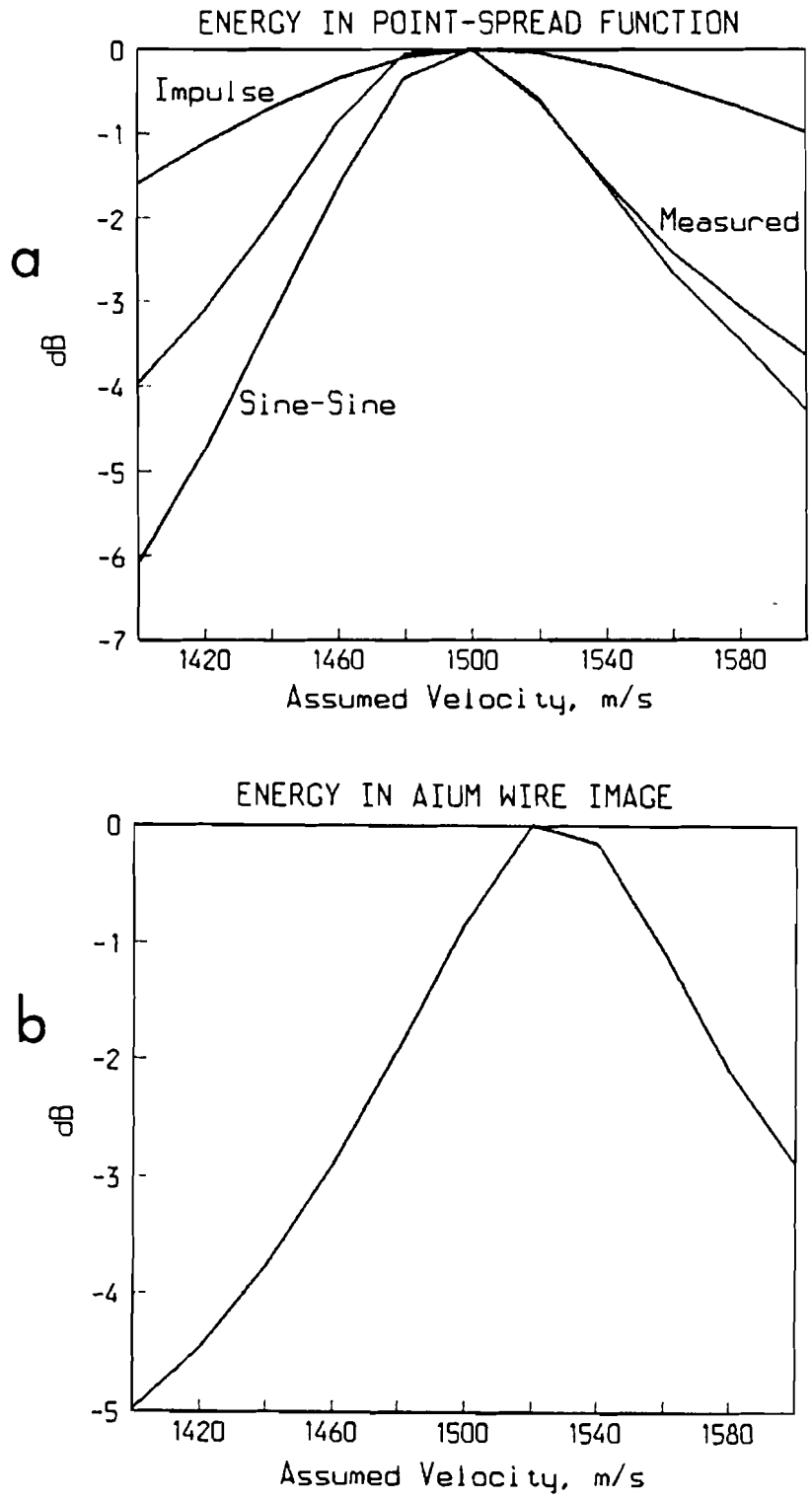

Figure 3. Variance of a) simulated point-spread functions and b) AIUM test-object wire image at a range of 50 mm. The simulated transducer was a 3.5 MHz, 32-element linear array (1.1 x 13 mm elements), driven by the functions shown in Figure 1. The test-object wire was 50 mm from a 3.5 MHz, 32-element linear array composed of uniform 1.1 x 13 mm transducers separated by 1.4 mm.

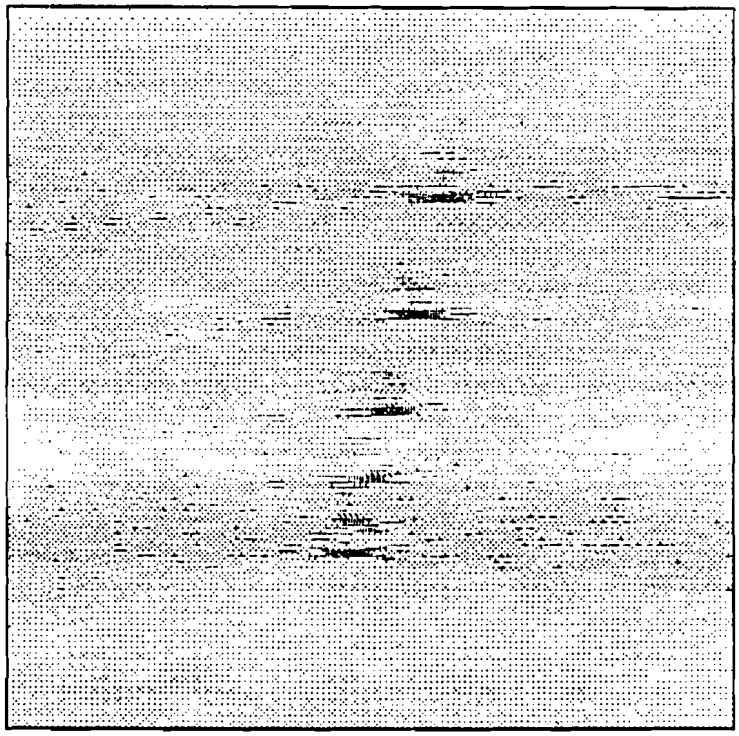

Figure 4. Complete-data-set, RF-signal reconstructed reflection tomogram of the central region of the AIUM 100-mm test object as viewed by a 32-element linear array with a center frequency of 3.5 MHz. Pixel separation is 60μm. Each image contains 512 x 512 pixels.

The behavior of both point-spread functions and wire images as a function of background velocity suggest that a peak in the variance of an image may give an estimate of the background velocity, i.e., the background velocity on reconstruction is correct if the image is focused. This interpretation requires that the wire properties influenced the background velocity. The AIUM test object was filled with deionized water at 24.3° C. Sound velocity in the water was therefore about 1495 m/s. The peak in the variance, however, occurred at 1520 m/s. Presumably the effective background velocity was shifted towards the much higher velocity of the stainless steel wire by scattering from the back and side walls of the wire.

1. Mesdag, P. R., de Vries, D., and Berkhout, A. J., "An Approach to Tissue Characterization Based on Wave Theory Using a New Velocity Analysis Technique," Acoustical Imaging, eds. E. A. Ash and C. R. Hill, Plenum Press, 12:479-491, 1982.

2. Lockwood, J. C. and Willette, J. G., "High-Speed Method for Computing the Exact Solution for the Pressure Variations in the Nearfield of a Baffled Piston," Journal of the Acoustical Society of America, 53:735-741, 1973.

C. Quantitative Imaging: Optical-Sectioning Microscopy

Knowledge of the three-dimensional architecture of organisms and cells is an obvious prerequisite to a further understanding of many significant biological and medical research problems. A classical approach to acquire such data has been to cut biological material into thin slices, and then examine each slice individually under the light or electron microscope. Unfortunately, this is a time-consuming and inaccurate process to reconstruct a three-dimensional image. Recently, alternative methods have become available to visualize a series of slices within an intact specimen. The new project of optical sectioning described here will involve the study of two of these alternative methods: computational image estimation and confocal microscopy.

Image-estimation techniques utilize knowledge of a microscope's point-spread function. This is the three-dimensional image that a point source of light would yield after passage through the lens system of the microscope. The resulting image of a point source is no longer a point, but rather a series of diffraction-ring patterns which grow in radius as one moves in either direction about the focal plane. This means that any microscope image will be a distorted version of the object under examination. Image-estimation techniques are used to recover some of this degraded information. In particular, image-estimation procedures produce a clearer image in any particular focal plane by effectively removing the contributions of diffraction-ring patterns which originate from numerous points in out-of-focus planes in the specimen. It is this out-of-focus information contributed by surrounding planes that has in the past necessitated the physical slicing of a specimen into thinner sections.

The current report describes early work on two aspects of the estimation approach to optical sectioning. In Section C-1, methods used for positron-emission tomography (Section A) are adapted to the optical-sectioning problem. As discussed in C-1, these algorithms should offer more accurate estimates of the object than algorithms currently in use elsewhere. Section C-2 describes efforts to reconcile differences between experimental determinations of the point-spread function and theoretical expectations. The aim here is to incorporate the effects of lens aberrations into the appropriate formula for the point-spread function.

A second approach to obtain optical sections is to use a confocal microscope. This instrument is designed so that a great deal of out-of-focus information is eliminated by optical means. Section C-3 briefly describes the principle of operation of such a microscope, and then reports the results of preliminary examination of one such instrument. The goal of these studies is to compare the optical-sectioning capabilities of the confocal microscope with image-estimation procedures. Another aim is eventually to apply image-estimation procedures to confocal images.

C-1. Reconstruction Algorithms for Optical-Sectioning Microscopy

Personell: D. L. Snyder, BCL
J. G. McNally, BCL
M. I. Miller, BCL
D. G. Politte, BCL
C. Preza, BCL
L. J. Thomas, Jr., BCL

Support: RR 01380

Shown in the following figure is a model for the object and data acquired in fluorescence imaging using optical-sectioning microscopy. The object consists of J planar sections through some tissue or other microscopic sample of interest. The tissue contains a minute quantity of a tracer which fluoresces when photoactivated, thereby permitting organelles of interest to which the tracer is bound to be visualized. Photons created in the fluorescence process are collected as image data with the optical system of the microscope. Several microscopic images, the number being K in the figure, are collected, where each image corresponds to a different focal-plane setting of the microscope.

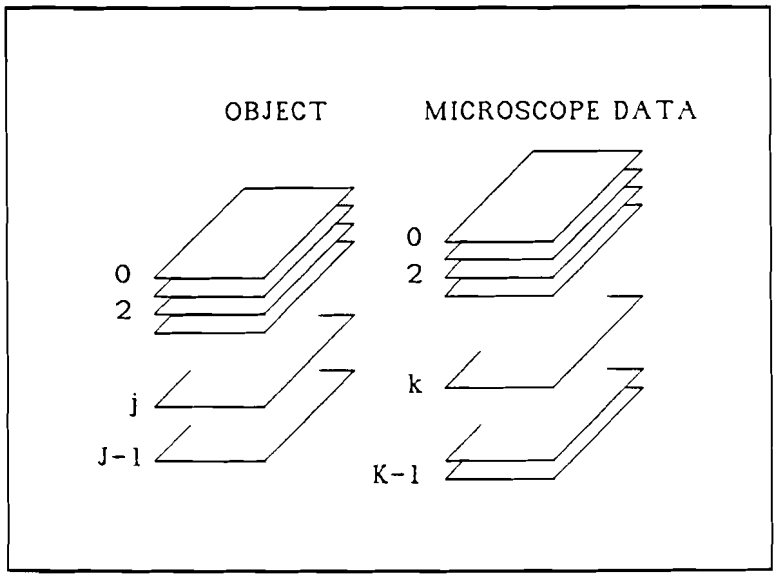

From the basic physics of the fluorescence process, the fluctuation statistics of emitted photons are described by a time-space Poisson point-process having an intensity that is constant in time, assuming a time-invariant photoactivation intensity and a stable tissue sample, and varying in space in proportion to the nonuniform spatial concentration of the tracer. We will assume that each of the K microscopic images forming the data are collected in equal time intervals, which, with the temporal

homogeneity of the photon emissions, implies that temporal aspects of the photon emissions can be disregarded.

The K data-images result from the detection of photons which have propagated from the tissue sample through the optics of the microscope and onto the surface of the photodetector. A point source of photons located somewhere in the tissue will result in a blurred data-image because the optics and detection processes are imperfect. We will denote by $p_{kj}(x,y)$ the probability density function of the location (x,y) in the data image of photons emanating from a point source in the jth section of the object when the microscope is adjusted for the kth focal plane. This density is also termed the point-spread function for section j and focal plane k, the form of this function is discussed elsewhere. We will assume that each fluorescence photon is affected independently in its propagation from the tissue to the detector. Using the same argument as in [1] for photon translations in positron-emission tomography, it then follows that the detected photons making up the kth data image are described statistically as a spatial Poisson process with a two-dimensional intensity given by:

$$\mu_k(x,y) = \sum_{j=0}^{J-1} \int\int p_{kj}(x-x',y-y')\lambda_j(x',y')dx'dy',$$

where $\lambda_j(x',y')$ is the intensity with which fluorescence photons are emitted at location (x',y') in the jth section of the object, and the integrals extend over the entire spatial extent of the object in the jth section. It is evident that photons emanating from all J sections in the object contribute photons to the image data formed for the kth focal plane.

Let $N_k(\Delta x,\Delta y)$ denote the image data obtained in pixel $(x,x+\Delta x) \times (y,y+\Delta y)$ for the kth focal plane. The data for this pixel are Poisson distributed with mean

$$\int_x^{x+\Delta x} \int_y^{y+\Delta y} \mu_k(x',y')dx'dy'.$$

The problem of estimating the spatial distribution of the tracer within the three-dimensional tissue sample may now be stated as the following statistical-estimation problem. Given the above model describing the statistics of fluorescence photons and the point-spread blurring of the microscope, and given image data $N_k(\Delta x,\Delta y)$ for k = 0, 1, ..., K-1, estimate or reconstruct the intensities $\lambda_j(x,y)$ for each section j = 0, 1, ..., J-1. We propose to apply the maximum-likelihood method for estimating these intensities.

With a development very parallel to that used for positron-emission tomography, we obtain the following expectation-maximization algorithm for producing the maximum-likelihood estimates iteratively:

$$\lambda_j^{(m+1)}(x,y) = \lambda_j^{(m)} \sum_{k=0}^{K-1} \int\int \left[\frac{p_{kj}(x'-x,y'-y)}{\sum_{j=0}^{J-1} \int\int p_{kj}(x'-u,y'-v) i_j^{(m)}(u,v)\,du\,dv} \right] N_k(dx',dy'),$$

for $j = 0, 1, \ldots, J-1$. This iteration equation is quite similar to the one for time-of-flight positron-emission tomography, with the exception that there are J images being created, one for each object section, which implies a potential increase in the computational load compared to that for positron-emission tomography. The introduction of kernel sieves and resolution kernels to suppress noise and edge artifacts would be similar to that for their use in positron-emission tomography, but here the point-spread function at each focal plane would be adjusted. This could be accomplished by modifying the known modulation transfer-function at each depth and then inverse Fourier transforming.

The use of the expectation-maximization algorithm for producing maximum-likelihood estimates of radiotracer concentrations in positron-emission tomography has been under study as an alternative to the confidence-weighted algorithm, which is the algorithm currently used for processing data acquired with all time-of-flight tomographs. The confidence-weighted algorithm is a linear, least squares solution to the problem of estimating concentrations from time-of-flight data. While the images produced with it are noiser and have more artifacts than those produced by the expectation-maximization algorithm, they have the advantage of being available more quickly because the confidence-weighted algorithm is not iterative.

Motivated by the lower computational demands of the confidence-weighted algorithm for positron-emission tomography, we have also derived the analogous result for optical sectioning microscopy. The processing can be performed in two steps. The first yields confidence-weighted preimages, and the second yields the final confidence-weighted images. For the first step, the preimage for the ith tissue section, denoted by $a_i(x,y)$, is formed according to

$$a_i(x,y) = \sum_{k=0}^{K-1} \int\int p_{ki}(y-y',x-x') N_k(dx',dy'),$$

for i = 1, 2, ..., J-1. Let $A_i(u,v)$ denote the two-dimensional Fourier transform of the ith preimage, and define the J-dimensional vector of preimages

$$A(u,v) = \begin{bmatrix} A_0(u,v) \\ A_1(u,v) \\ \vdots \\ A_{J-1}(u,v) \end{bmatrix}.$$

In the second step, the Fourier transforms of the final images are obtained from these transformed preimages in the following way. Let $B_{ij}(u,v)$ be defined as follows

$$B_{ij}(u,v) = \sum_{k=0}^{K-1} P^*_{ki}(u,v) P_{kj}(u,v),$$

where $P^*_{ki}(u,v)$ is the two-dimensional Fourier transform of the point-spread function $p_{ki}(x,y)$ for the ith section to the kth focal-plane data, and define the JxJ-dimensional matrix with these quantities as its elements

$$B(u,v) = \begin{bmatrix} B_{0,0}(u,v) & B_{0,1}(u,v) & \cdots & B_{0,J-1}(u,v) \\ B_{1,0}(u,v) & B_{1,1}(u,v) & \cdots & B_{1,J-1}(u,v) \\ \vdots & \vdots & \cdots & \vdots \\ B_{J-1,0}(u,v) & B_{J-1,1}(u,v) & \cdots & B_{J-1,J-1}(u,v) \end{bmatrix}.$$

Also, let $\Lambda_i(u,v)$ denote the Fourier transform of the image in the ith section, and define the J-dimensional vector of estimates of these according to

$$\hat{\Lambda}(u,v) = \begin{bmatrix} \hat{\Lambda}_0(u,v) \\ \hat{\Lambda}_1(u,v) \\ \vdots \\ \hat{\Lambda}_{J-1}(u,v) \end{bmatrix}.$$

Then, the Fourier transforms of the final images produced with the confidence-weighted algorithm are given by

$$\hat{A}(u,v) = B^{-1}(u,v)A(u,v).$$

In implementing these steps, a finite-resolution window applied to each element of B(u,v) may be desirable for stabilizing the matrix before inverting it. This issue and others, such as how any symmetries of the point-spread functions might be used to speed computations, must be explored for this algorithm. The preimages A(u,v) are data dependent, and therefore need to be computed following the collection of data. The matrix B(u,v) is not data dependent, so its inverse can be precomputed once the point-spread functions of a given microscope are known.

1. Snyder, D. L., Thomas, Jr., L. J., and Ter-Pogossian, M. M., "A Mathematical Model for Positron-Emission Tomography Systems Having Time-of-Flight Measurements," IEEE Transactions on Nuclear Science, NS-28(3):3575-3583, June 1981.

C-2. Computation of Three-Dimensional Optical Point-Spread Functions in the Presence of Spherical Aberration

Personnel: C. Preza, BCL
J. G. McNally, BCL
L. J. Thomas, Jr., BCL

Support: RR 01380

An essential first step in implementing reconstruction techniques for optical-sectioning microscopy is to determine the transmission properties of a microscope imaging system. Such properties are specified by the optical-transfer function (which is derived from the pupil function [1, 5, 6]) and its inverse Fourier transform, the point-spread function. The point-spread function is the three-dimensional image of a point source after passage through the microscope's lens system.

We have numerically evaluated theoretical optical-transfer functions for an aberration-free system using Hopkins' formula [5], and obtained point-spread functions by inverse-transforming. The resulting three-dimensional point-spread function shows that diffraction patterns are nearly identical on either side of the plane of focus. However, images that we obtained from fluorescent beads 0.05μm in diameter show that while diffraction rings are present on one side, only a fading central spot is observed on the other side. Others have also seen this effect [2, 4] which implies that the lens is not aberration-free. The observed point-spread function is probably due to uncorrected spherical aberration in the microscope objective lens [3, 4].

Our aim is to formulate the three-dimensional point-spread function that incorporates the effects of spherical aberration so that numerical computation of any desired function is possible without time-consuming and noise-prone experimental measurements. Black and Linfoot [1] obtained a formula for the optical-transfer function for a lens with spherical aberration. Unfortunately, their formula involves parameters which have no direct physical interpretation. Starting from first principles, we have rederived their formula in terms of variables which might be measured more easily.

As shown by Smith [7], the optical path-length error w in terms of the defocus distance Δz and the marginal longitudinal third-order spherical aberration, LA_m, (Figure 1) is

$$w = \frac{1}{2} n \sin^2 u[\Delta z - \frac{1}{2} LA_m(\frac{Y}{Y_m})^2] \qquad (1)$$

where n is the refractive index, Y is the radial coordinate in the lens, Y_m is the maximum radius of the lens, and u is the angle formed by the refracted ray and the optical axis.

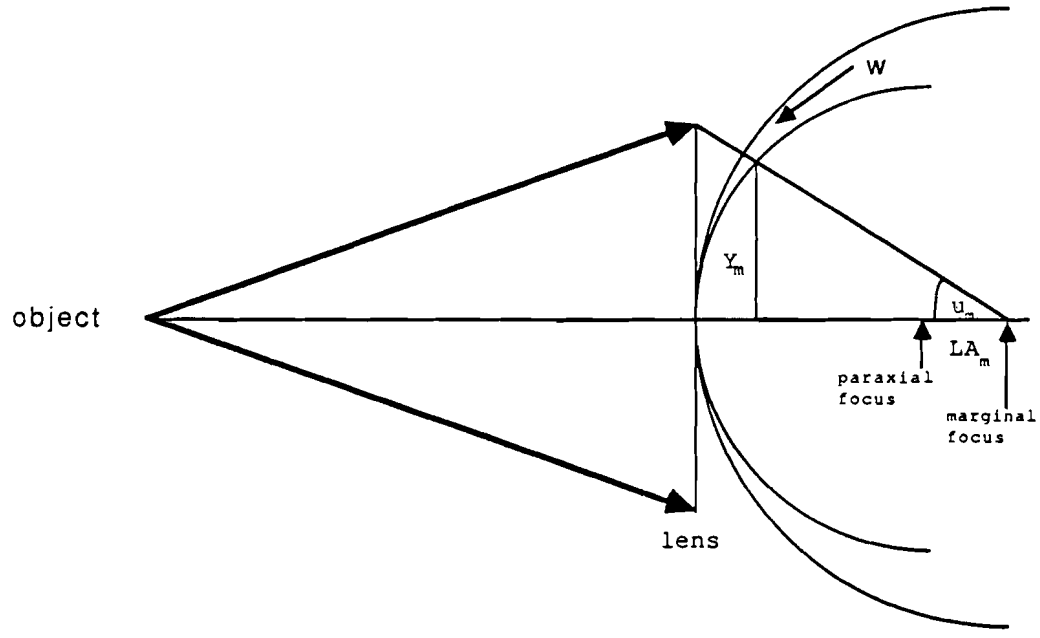

Figure 1. Schematic illustration of a lens with spherical aberration LA_m. The optical path-length error w is the difference between the two spherical wavefronts centered at the paraxial and marginal focus respectively.

Equation (1) can be simplified to

$$w = A(s^4 - Bs^2) \tag{2}$$

where we have substituted $s = \frac{Y}{Y_m}$, $A = -\frac{1}{4} n LA_m \sin^2 u_m$ and $B = -2 \frac{\Delta z}{LA_m}$.

Using w given by equation (2), we have derived by the method shown in [6] the following formula for the optical-transfer function with spherical aberration:

$$T(s) = \frac{4}{\pi} \int_0^{\sqrt{1-s^2/4}} \int_0^{-s/2+\sqrt{1-\xi^2}} \cos\left[\frac{2\pi}{\lambda} As\phi(2B + 4(\phi^2 + \xi^2)+s^2)\right] d\phi d\xi, \tag{3}$$

where s, A and B are defined above, and λ is the wavelength of light. Equation (3) agrees with Black and Linfoot's result [1].

We have numerically integrated (3) using two different methods (Simpson's and Gaussian quadrature), and then inverse-transformed the result to determine point-spread functions (Figure 2) for different values of the parameter A which measures third-order spherical aberration. Note that these functions are symmetric around r (the radial direction in the x-y plane), but not around the z axis. Observe also that, the spread is more severe for higher values of A. These calculated functions agree with qualitative observations of point-spread functions.

We are currently evaluating experimental approaches to measure A or LA_m in a lens. Our future plans include comparisons of empirically determined point-spread functions with those computed using equation (3) and the measured parameter A.

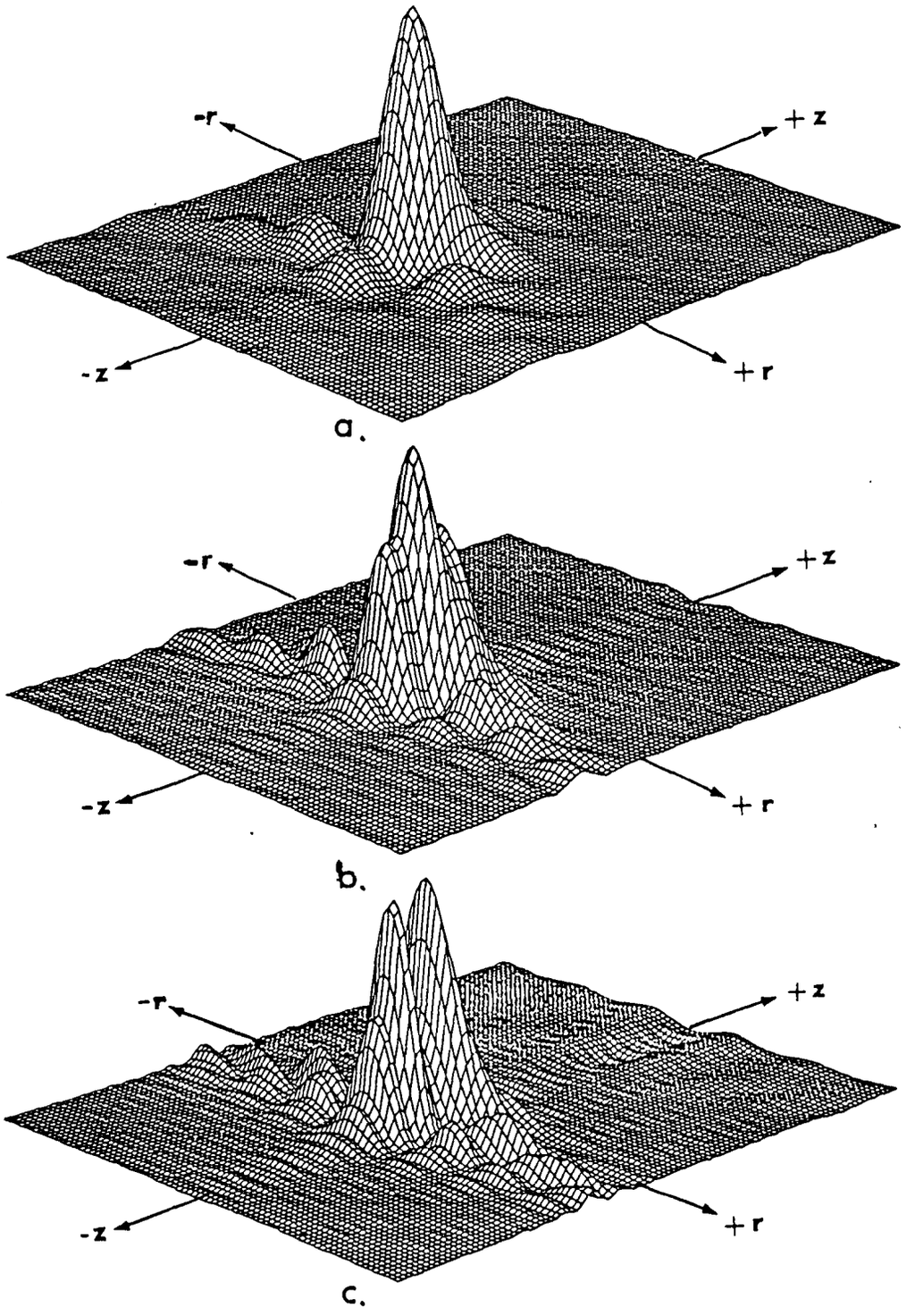

Figure 2. Three-dimensional point-spread functions with spherical aberration for three values of A: a) A = 1, b) A = 2, and c) A = 3. r denotes the radial direction in the x-y plane (the point-spread function is circularly symmetric in x-y). z indicates the amount of defocus above and below the focal plane. The height scale, and the scale in the r-z plane are the same for the three functions.

1. Black, G., and Linfoot, E. H., "Spherical Aberration and the Information Content of Optical Images," Proceedings of the Royal Society of London A., 239:522-540, 1957.

2. Fay, F. S., Fogarty, K. E., and Coggins, J. M., "Analysis of Molecular Distribution in Single Cells Using a Digital Imaging Microscope," in Optical Methods in Cell Physiology, P. DeWeer and B. M. Salzberg, eds., vol. 40, pp. 51-63, 1986.

3. Francon, M., Progress in Microscopy, Roy, Peterson, Evanston, IL, 1961.

4. Hiraoka, Y., Sedat, J. W., and Agard, D. A., "The Use of a Charge-Coupled Device for Quantitative Optical Microscopy of Biological Structures," Science, 238:36-41, 1987.

5. Hopkins, H. H., "The Frequency Response of a Defocused Optical System," Proceedings of the Royal Society of London A, 231:91-103, 1955.

6. Nussbaum, A., Phillips, R. A., Contemporary Optics for Scientists and Engineers, Prentice-Hall, NJ, 1976.

7. Smith, W. J., Modern Optical Engineering. The Design of Optical Systems, McGraw-Hill Book Company, NY, 1966.

8. Stokseth, P. A., "Properties of a Defocused Optical System," Journal of the Optical Society of America, 59:1314:1321, 1969.

C-3. Preliminary Evaluation of a Scanning Confocal Microscope

Personnel: J. G. McNally, BCL
L. J. Thomas, Jr., BCL

Support: RR 01380

The principle of confocal microscopy [1] is to image one point at a time in a specimen. An objective and a collector lens are arranged such that the focal point in the specimen coincides exactly with both the point of illumination and detection. In this way, only information at the focal point is retrieved, and out-of-focus contributions are suppressed. A complete image is constructed from a three-dimensional scan of the specimen.

We have examined one such microscope (The Biorad MRC Lasersharp) which has recently become available commercially. This instrument uses a laser for illumination. Scanning is done by moving the laser beam across the specimen.

We have used the MRC Lasersharp microscope to image 0.5μm or 0.05μm beads containing the fluorescent dye coumarin. Three different installations of the microscope have been tested. We have found evidence for two problems: bleaching and coma.

We have been unable to image 0.05μm beads because they bleach too rapidly, even with the laser attenuated as much as possible. In contrast, larger beads (0.5μm) are easily seen because they contain much more dye. Although the 0.05 μm beads can be seen, they fade in a matter of seconds. Typically, this is not enough time to locate and focus on a particular bead. It is certainly not enough time to acquire a series of images at different focal settings. (The same size bead can be visualized for up to 15 minutes on a conventional fluorescence microscope). Bleaching on the confocal microscope is a problem because experimental determination of the point-spread function is best done using as small a bead as possible (to approximate a point source). The bleaching of the 0.05μm beads means it may be difficult to measure point-spread functions and ultimately apply image-estimation procedures on the MRC Lasersharp. We intend to examine fluorescent beads on other confocal microscopes as they become available to see if the bleaching problem is a general one. Obviously, bleaching could be a serious problem for biomedical investigators. It may make it impossible to visualize probes with low quantum yields or to examine probes with high quantum yields in living specimens where low light levels are routinely used to minimize damage due to heating or products of photolysis.

A second problem that we have observed with the MRC Lasersharp is the optical aberration known as coma. Coma occurs in a lens when paraxial rays are magnified differently from marginal rays. The point-spread function of a comatic lens displays crescent-shaped segments about the central bright spot, where circularly symmetric diffraction rings are ordinarily observed. We have observed this comatic effect on two of the three MRC Lasersharp installations tested. The variation may be due to the particular objective lenses in use, or may indicate a requirement for especially precise alignment.

1. Wilson, T., and Sheppard, C., Theory and Practice of Scanning Optical Microscopy, Academic Press, London, 1984.

D. Ischemic Heart Disease and ECG Analysis

This section reports ongoing collaborative and support activities in cardiology projects concerned with the diagnosis and treatment of patients with ischemic heart disease. Collaborative projects include the assessment of vascular integrity of the myocardium following ischemic injury, the investigation of electrophysiological and biochemical factors underlying the genesis of dysrhythmias due to myocardial ischemia and infarction, and the application of the analysis of plasma-CK profiles following myocardial infarction. Supporting activities include development of a software system for frequency-domain analysis of signal-averaged ECG data. Our efforts to construct an annotated clinical-event database of ECG waveforms have ceased, as is reported in this section.

For two decades, this section reported activities related to high-speed processing of long-term, tape-recorded electrocardiograms primarily for large multicenter studies sponsored by pharmaceutical corporations or the National Institutes of Health. Those activities have now ceased as have dysrhythmia detection algorithm development efforts. Appropriately, these algorithms have found their way to other universities and to the commercial sector.

D-1. Assessment of Vascular Integrity of the Myocardium Following Ischemic Injury

Personnel: R. G. Tilton, Ph.D., Pathology
C. M. Kilo, M.D., Medicine
M. P. Land, B.S., Pathology
K. B. Larson, BCL
S. P. Sutera, Ph.D., Mechanical Engineering
J. R. Williamson, M.D., Pathology

Support: RR 01380
HL 31531
The Kilo Diabetes and Vascular Research Foundation

We have continued our previously reported studies (PR 23, D-1) of the role of the endothelium in the pathogenesis of vascular hemodynamic and permeability changes associated with ischemia and reperfusion. In these studies, we employ external-detection techniques coupled with tracer-kinetic analysis to quantify radiolabeled albumin transport across the coronary vasculature under physiological conditions, and during reperfusion after ischemia in isolated-perfused rabbit hearts. The resulting residue-detection data, analyzed on the basis of a two-compartment model of tracer transport [1], are used to estimate parameters indicative of microvascular integrity, such as permeability and ultrafiltration conductance of endothelium.

During the period covered by this report, we have assessed effects of streptozotocin (STZ)-induced diabetes on coronary vascular hemodynamics and myocyte contractility in isolated hearts from Sprague-Dawley rats during 40 minutes of constant-pressure reperfusion after 40 minutes of global, no-flow ischemia, and have demonstrated the same injury in this species that we have reported for diabetic rabbits. In hearts from control rats, vascular resistance increased 1.7x baseline and left ventricular end-diastolic pressure (LVEDP) (monitored from a left ventricle isovolumic balloon) increased 7x baseline during reflow after ischemia. Left ventricular developed pressure and maximum +dP/dt recovered 50% during reflow. In hearts from diabetic rats, vascular resistance remained at baseline levels throughout reflow, and LVEDP, which was elevated two fold after 40 minutes of no-flow ischemia, quickly returned to baseline during reflow. Both LV developed pressure and maximum +dP/dt returned to baseline by 30 minutes of reflow.

We have initiated several studies in rats assessing possible pathogenetic mechanisms involved in the diabetes-induced protection of myocardium; these experiments are focused on the possible role of the polyol pathway and functional alterations in phosphoinositide metabolism. The rationale for these experiments is based on recent studies which have provided strong evidence that most diabetic complications are aldose reductase-linked phenomena resulting from imbalances in polyol and myo-inositol metabolism.

In experiments designed to assess effects of the aldose reductase inhibitor, Sorbinil, on diabetes-induced amelioration of ischemic injury, three groups of rats were used: control, STZ-diabetic, and STZ-diabetic rats treated with Sorbinil (added to the diet to provide a daily dose of 0.2 mmole/kg body weight). Sorbinil treatment did not reverse the myocyte resistance to ischemic injury (LVEDP increases were identical in untreated and Sorbinil-treated diabetic rats); likewise, vascular resistance decreased significantly below baseline during reflow. It is of interest that Sorbinil did decrease baseline LV developed pressure and maximum +dP/dt (versus untreated diabetics), but during reflow after ischemia, both indexes of ventricular function increased 50% above baseline values.

In other experiments, we have investigated the possibility that functional derangements in intracellular phosphoinositide metabolism may be responsible for the pathogenesis of the diabetes-induced resistance to ischemic injury by using four groups of rats: control, diabetic, control rats pretreated for 24 hours with 10 mEq/kg body weight LiCl, and diabetic rats pretreated with LiCl. No differences were evident between both diabetic groups and results were similar to the data presented above. While results from the untreated control group also were similar to data presented above, it is of great interest that in the LiCl-treated control group, LVEDP, developed pressure, maximum +dP/dt, and vascular resistance changes during reflow after 40 minutes of no-flow ischemia were identical to those observed in the untreated diabetic group. These results strongly suggest that the resistance to ischemic injury observed in hearts from diabetic animals may reflect a functional derangement in the phosphoinositide signaling system.

Additional experiments are in progress assessing effects of Na^+/K^+-ATPase inhibition in control and diabetic rats. The rationale for these experiments is based on the observation that in diabetic nerve, reduction in tissue levels of myo-inositol is associated with a reduction in Na^+/K^+-ATPase activity, and that dietary myo-inositol supplementation restores tissue levels of myo-inositol, Na^+/K^+-ATPase activity, and ameliorates the functional neuropathy. Preliminary results suggest that acute intravascular perfusion of ouabain (1-10 μM) prior to ischemia slightly ameliorates ischemia-induced increases in left ventricular resting tension (versus controls) but not to the extent seen in diabetic animals.

1. Tilton, R. G., Larson, K. B., Udell, J. R., Sobel, B. E., and Williamson, J. R., "External Detection of Early Microvascular Dysfunction After No-Flow Ischemia Followed by Reperfusion in Isolated Rabbit Hearts," Circulation Research, 52:210-225, 1983.

D-2. Electrophysiological and Biochemical Factors Underlying the Genesis of Arrhythmias Due to Myocardial Ischemia and Infarction

Personnel: P. B. Corr, Ph.D., Medicine and Pharmacology
S. M. Moore, BCL and Medicine
J. M. Peirick, M.S., Medicine
S. M. Pogwizd, M.D., Medicine
B. E. Sobel, M.D., Medicine
K. A. Yamada, Ph.D., Medicine

Support: HL 07275
HL 17646
HL 28995
HL 36773

The overall concept of the research is that potential arrhythmogenic metabolites, including lysophosphoglycerides and long-chain acylcarnitines, accumulate in ischemic tissue and contribute to the electrophysiologic derangements and associated malignant arrhythmias. Over the past several years, studies have also been completed demonstrating a major electrophysiologic role of α_1-adrenergic stimulation during myocardial ischemia as well as reperfusion. In addition, we have demonstrated, using radioligand binding procedures, a two-fold reversible increase in α_1-adrenergic binding sites in ischemic and reperfused myocardium.

Results of previous studies have strongly implicated endogenous long-chain acylcarnitines (LCA) as a mediator of the electrophysiologic impairment secondary to hypoxia (PR 23, D-2). Likewise we have demonstrated the marked antiarrhythmic effect of POCA, an inhibitor of carnitine acyltransferase I (CAT I), in vivo during myocardial ischemia associated with prevention of the increase in LCA. In experiments in cats,

POCA prevented the increase of LCA in the ischemic zone, inhibited lysophosphatidylcholine (LPC) accumulation, and precluded the development of ventricular fibrillation. Thus, the potent antiarrhythmic efficacy of inhibation of CAT I is dependent on inhibition of accumulation of both LPC and LCA.

Several years ago, we demonstrated that ischemia is associated with a two-fold reversible increase in myocardial α_1-adrenergic receptors, which is induced by the accumulation of LCA in sarcolemma (SL). To determine whether the hypoxic-induced increase in α_1-adrenergic receptors results in increased intracellular coupling to inositol trisphosphate (IP_3) production, a novel procedure to quantify IP_3 in normoxic or hypoxic adult canine myocytes was used. In normoxic myocytes, IP_3 levels peaked 30 seconds after norepinephrine (NE, 10^{-5} M) stimulation (61.5 $\pm$ 7.5 pmoles/mg protein, n=4) and returned to basal levels (17.3 $\pm$ 2.8) by 60 seconds. The IP_3 response exhibited an EC_{50} of $8x10^{-8}$ M and was blocked by α_1-adrenergic antagonists. Hypoxic myocytes (10 min, PO_2 < 15 mm Hg, 37°C) produced a markedly enhanced IP_3 response to NE (EC_{50} = 1 x 10^{-8} M, p <.001) resulting in a 100-fold reduction in the concentration of NE required to produce a threshold increase in IP_3 (10^{-10} M vs 10^{-8} M). Thus, increased α_1-adrenergic receptors induced by hypoxia are coupled to an increased IP_3 response indicative of enhanced α_1-responsivity in the ischemic heart in vivo.

We recently completed studies to determine whether α_1-adrenergic receptor stimulation per se (phenylephrine 10^{-7} M) increases phospholipase A_2 activity thereby contributing to the accumulation of lysophosphatidylcholine in isolated adult canine myocytes exposed to hypoxia (PO_2 < 10 torr) with or without acidosis (pH = 6.5). Lysophosphatidylcholine in control myocytes was 2.76 $\pm$ 0.60 nmol/mg protein. Neither hypoxia nor acidosis alone induced accumulation of lysophosphatidylcholine (3.66 $\pm$ 0.73, p=NS). However, lysophosphatidylcholine increased markedly to 14.80 $\pm$ 1.67 nmol/mg protein within one minute of α_1-stimulation (p < 0.01) in the presence of hypoxia and acidosis and returned to control levels within 10 minutes. Thus, α_1-adrenergic receptors are not only enhanced by metabolic changes accompanying hypoxia, including the accumulation of LCA in the SL, but also stimulation of the α_1-adrenergic receptor potentiates the accumulation of lysophosphatidylcholine thereby contributing to the arrhythmogenic effects of catecholamines in the ischemic heart.

One major aim of this project is also to delineate the cellular electrophysiologic alterations which contribute to the frequency alterations derived from the surface ECG recordings from patients with compared to those without ventricular tachycardia after myocardial infarction. Developing a detailed understanding at the cellular level for these alterations in frequency content of the surface ECG will permit its application not only to more accurate prediction of patients at risk for developing lethal arrhythmias, but also for assessing the efficacy of pharmacologic interventions. This has required the development of unique hardware and software which will permit very high resolution X, Y, and Z lead recordings of the surface ECG. A number of developments and improvements in the electronic and computer hardware associated with this

aspect of the research have been implemented and validated during the last eight months.

High-frequency, high-resolution amplifiers have been developed to acquire three-lead ECG data. The performance of these amplifiers has been tested and verified. These amplifiers are affected by low level (approximately 106 μV), medium-frequency (600 Hz - 2000 Hz) noise emitted by the existing 240-channel mapping-system amplifiers. This problem has been addressed and corrected, to a large extent, by the construction of an electromagnetic interference grounding enclosure, or Faraday cage, for the mapping system. The Faraday cage reduces the amount of noise emitted by the mapping system significantly. There have been a number of significant upgrades to the existing computer equipment. A graphics hardware system that is more flexible and sophisticated than the existing equipment has been installed with attendant software. These improvements are essential to the aims outlined above. Additional networking hardware has been installed to allow for more flexible and free-flowing information exchange among existing computers involved in this project. Additional fixed-disk memory capacity has been installed to accomodate the quickly expanding base of data and locally generated software.

The development of several major software modules began six months ago. Now complete are programs that acquire action potentials from analog magnetic tape, process the data, and present a graphic display of each action potential and its parameters. In progress is a major software-development project for the acquisition and analysis of data from the new ECG amplifiers described above. Included in this package are sophisticated frequency-domain analysis routines as well as specialized acquisition and data-transfer routines. A routine which allows investigators to interface with the graphics hardware has been tested and is ready for use. A library of mathematical subroutines for processing of the data has been assembled; all subroutines were investigated to define the limitations of the algorithms utilized.

During the next year, these advanced hardware and software procedures will be applied to studies of evolving myocardial infarction in dogs. With the newly developed system, analysis of frequency content can be performed on single beats without signal averaging. In each animal, detailed three-dimensional mapping will be applied simultaneously with acquisition of the surface X, Y, and Z leads to answer initially two basic questions: 1) when in the cardiac cycle do the alterations in frequency content of the surface ECG occur? and 2) at the time of occurrence of these frequency alterations in the surface ECG, what are the underlying electrophysiologic alterations in the tissue?

D-3. Analysis of Plasma CK Isoforms

Personnel: D. R. Abendschein, Ph.D., Medicine
J. J. Billadello, M.D., Medicine
H. L. Fontanet, M. D., Medicine
A. S. Jaffe, M.D., Medicine
J. Markham, BCL
L. M. Seacord, M.D., Medicine
B. E. Sobel, M.D., Medicine
A. W. Strauss, M.D., Pediatrics

Support: HL 17646
HL 36274

The objective of these studies is to apply analysis of isoforms of individual isoenzymes of creatine kinase in plasma for rapid detection and timing of the onset of myocardial infarction and reperfusion. We have shown previously that changes in plasma profiles of isoforms of the MM isoenzyme permit detection of acute myocardial infarction before significant changes in conventional enzymatic criteria of infarction are manifested (PR 23, D-4). In the past year, we have shown that analysis of MM isoforms also permits very early recognition of coronary artery recanalization after thrombolysis in patients [1]. A rapid assay for quantification of MM isoform profiles in plasma samples yielding results within one hour has been implemented to facilitate analysis for early detection of both initial infarction and of coronary recanalization [2,3].

Using data obtained by serial analysis of plasma isoform concentrations in dogs after intravenous injections of purified isoforms both with and without inhibition of the enzyme identified by our laboratory as the converting agent in plasma [4], we have developed a compartmental model to describe the kinetics of the observed plasma time-activity profiles of isoforms in vivo [5]. Computer simulations with the model are close to experimental data and show, interestingly, that the isoform purified from myocardium has a faster plasma clearance than either of the two other isoforms which evolve sequentially with time.

In the next year, we plan to assess the affect on plasma profiles, and on the mathematical model developed, of converted isoforms entering the circulation from cardiac lymph and directly from myocardium during infarction in dogs. With these refinements of the model, we will then evaluate methods for estimation of the time of onset of infarction based on the isoform profiles in one or two plasma samples obtained early in the course of myocardial infarction.

1. Seacord, L. M., Abendschein, D. R., Nohara, R., Hartzler, G., Sobel, B. E., and Jaffe, A. S., "Detection of Reperfusion Within One Hour after Coronary Recanalization by Analysis of Isoforms of the MM Creatine Kinase Isoenzyme in Plasma," Fibrinolysis, 2:151-156, 1988.

2. Nohara, R., Sobel, B. E., Jaffe, A. S., and Abendschein, D. R., "Quantitative Analysis of Isoforms of Creatine Kinase MM in Plasma by Chromatofocusing, with On-Line Monitoring of Enzyme Activity," Clinical Chemistry, 34:235-239, 1988.

3. Abendschein, D. R., Seacord, L. M., Nohara, R., Sobel, B. E., and Jaffe, A. S., "Prompt Detection of Myocardial Injury by Assay of Creatine Kinase Isoforms in Initial Plasma Samples," Clinical Cardiology, in press.

4. Abendschein, D. R., Serota, H., Plummer, Jr., T. H., Amiraian, K., Strauss, A. W., Sobel, B. E., and Jaffe, A. S., "Conversion of MM Creatine Kinase Isoforms in Human Plasma by Carboxypeptidase N," Journal of Laboratory and Clinical Medicine, 110:798-806, 1987.

5. Abendschein, D. R., Fontanet, H. L., Markham, J., and Sobel, B. E., "Physiologic Modelling of MM Creatine Kinase Isoforms," in Mathematical Modelling in Science and Technology, E, Y. Rodin and X. J. R. Avula, eds., Sixth International Conference Proceedings, Great Britain, Pergamon Press, 11:621-625, 1988.

D-4. Display Software for Signal-Averaged ECG Data

Personnel: R. E. Hermes, BCL
H. D. Ambos, Medicine
J. Markham, BCL
S. M. Moore, BCL and Medicine
D. M. Wade, BCL

Support: RR 01380
HL 17646

A major project in the division of cardiology for the past few years has been the evaluation of averaged ECG signals for indicators of the susceptibility of patients to occurrences of sustained ventricular tachycardia (VT). Initial efforts in this project focused on the frequency-domain content of the terminal portion of the QRS and ST segment. Indices computed from the spectra of this portion of the cardiac cycle were shown to differentiate between patients with and without a history of sustained VT. More recently, investigations of other portions of the cardiac cycle and of appropriate filtering techniques have been undertaken in order to define the frequencies in the ECG that reflect the electrophysiologic disturbances unique to patients with VT.

In BCL, efforts for this project have been directed toward the development of software to enable investigators to easily select intervals of the ECG for analysis by manual identification of fiducial marks in any of the three channels of ECG patient recordings. The interval selection

process has evolved from the tedious use of a Tektronix 4010 storage scope interfaced to a PDP-11 to a semi-automated approach using a Lexidata 3400 graphics system for waveform display and user interaction. All display and computation software has now been implemented on a MicroVAX II. Display and user interface software have been transferred to the X-windowing system, providing display-device independence and software portability. The interactive display system can now be made available to remote sites within the cardiology division allowing investigators to execute the analysis programs from their local computer. The biomedical research network provides access to the patient ECG data which are first recorded on a small data-acquisition system and stored on floppy disc for subsequent transfer to a MicroVAX II.

D-5. Annotated Clinical-Event Database for Evaluating Ambulatory ECG Analysis Systems

Personnel: K. W. Clark, BCL
L. J. Thomas, Jr., BCL

Support: RR 01380

Two years ago (PR 22, A-1), we began construction of a digital "annotated clinical-event" database (ACED) of 70 six-hour dual-channel electrocardiographic recordings. The set of 70 included ten in each of seven categories of cardiac dysrhythmia. We planned to include annotations for the time-of-occurrence of clinically relevant events and for noise levels. After most of the waveform records were collected, we applied to the National Institutes of Health for a small grant to complete the time-consuming annotation process, which included interpretation of clinical events by cardiologists and creation of a machine-readable annotations file.

The grant was finally approved after several delays, but the funding was inadequate for the task. Besides, a similar effort was already underway elsewhere, and we considered our project to be a duplication of effort. Therefore, we declined the grant and ceased work on the ACED.

E. Systems for Specialized Biomedical Studies

This section describes a number of projects in which significant progress was made or promising new work begun but do not fit conveniently into other sections of this report and, by themselves, do not require major sections for reporting. The projects summarized here include work in DNA restriction-map reconstruction, electron-microscopic autoradiography, radiation treatment planning, distortion removal from auditory-nerve discharge patterns, studies of color visual-field defects, and studies of massively-parallel processing.

E-1. Algorithms for DNA Restriction-Map Reconstruction

Personnel: G. Rhee, M.S., BCL and Computer Science
J. R. Cox, Jr., BCL and Computer Science
M. V. Olson, Ph.D., Genetics
J. S. Turner, Ph.D., Computer Science

Support: RR 01380
GM 28232

Work in the past year has focused on two aspects of the DNA mapping procedure: random clone sequencing and fragment-sequence optimization [1]. In the clone-sequencing phase, the relationships among overlapping clones are used to construct local maps of relative locations of random clones. The algorithms used to accomplish clone sequencing are inherently greedy. However, the performance of the algorithms depends on the heuristics used to evaluate ambiguities in the overlap relationships between a set of clones. Work in the past year has led to the development of a heuristic based on the ratio of the number of fragments in the overlap between two clones to the sum of the number of fragments in that pair of clones. This heuristic is subject to a subset-consecutiveness constraint which requires the clone in the middle to be a subset of the union of the surrounding clones in every three consecutive clones in a local map.

The second phase of the restriction-map reconstruction attempts to optimize the fragment sequence of each local map for a given clone sequence. The fragment-sequence optimization problem has been shown to be NP-complete (PR 23, E-1). Current work in this area focuses on developing efficient approximation algorithms to perform the optimization. Further progress in these areas will allow the testing of the methods on real clone data acquired with the data acquisition and analysis system described in the next section of this report (E-2).

1. Rhee, G., "DNA Restriction Mapping from Random-clone Data," Washington University Computer Science Department, WUCS-88-18, June 1988.

E-2. Data Acquisition and Analysis for DNA Restriction Mapping

Personnel: H. A. Drury, BCL
R. E. Hermes, BCL
M. V. Olson, Ph.D., Genetics
D. G. Politte, BCL
L. J. Thomas, Jr., BCL

Support: RR 01380
GM 28232
Center for Genetics in Medicine at Washington University
James S. McDonnell Foundation Grant #87-24

The goal of this project is the development of a data acquisition system that will allow direct imaging of electrophoretic gels that have been stained with fluorescent DNA-binding dyes. Algorithms that will improve automated detection of band intensities and extraction of fragment-size information from band mobilities will also be developed.

The collaboration between the Department of Genetics and this Resource began with the development of a first-generation interactive image-acquisition system for the analysis of electrophoretic gels. That system was fielded to Dr. Olson's laboratory in 1984 (PR 18, C-2) [1]. However, the array detectors that were commercially available when the first-generation system was developed did not have sufficient sensitivity to allow for the direct imaging of ultra-violet stimulated fluorescence. Consequently, it was necessary to first photograph the gel and then digitize the resulting photographic negative. The photographic step severely limited the dynamic range over which the intensity of the bands could be accurately measured. Current commercially available imaging devices, specifically charge-coupled devices, now have the needed sensitivity for direct image acquisition of electrophoretic gels which have been stained with fluorescent dyes [2]. The direct digitization of fluorescing electrophoretic gels will allow researchers to broaden the scope of their projects because of the increased range of fragment sizes which can be analyzed.

In the past year we have worked with Photometrics Ltd. (Tucson, Arizona) running preliminary tests to directly digitize ethidium-bromide stained electrophoretic gels. The camera tested was a liquid-cooled charge-coupled device (CCD) with a resolution of 384 x 576 elements. The thermoelectric cooling of the CCD chip to -50^{0}C significantly reduces thermal noise which can account for as much as 20% of the signal. Several gels were successfully digitized using the Photometrics camera at exposure times ranging from 0.2 to 20 seconds. Oversampled images were analyzed to determine the resolution required to ensure adequate sampling as specified by the Nyquist criterion. Based on these studies, it was determined that increased resolution was required; a 1000 x 1000 pixel CCD was chosen. The Photometrics camera was purchased by the Department of Genetics and is now undergoing more rigorous tests. A Sun 386i workstation was acquired by us to act as a host for the Photometrics camera. Work continues on the development of an interface between the host system and the camera.

Algorithms which perform automated fragment sizing will eliminate the subjective decisions made in determining the positions of multiple closely spaced fragments. This will aid in the removal of biased data before it is used in the physical map reconstruction (E-1). Among the more powerful resolution methods, "deconvolution" is most suited to the problem of resolving closely spaced band intensities. No a priori knowledge of the number of fragments in the gel profile is required. The gel process can be modeled as the blurring of an ideal gel profile with the spatially varying point-spread function to yield the observed profile. The problem to be solved is to reverse the effects of the point-spread function and to estimate the underlying function. We modeled the point-spread function and tested two resolution methods using both simulated and actual data. The techniques used to perform the estimation of the underlying signal included the maximum-likelihood method in the fashion applied to positron-emission tomography [3] and the non-linear, constrained method of Jansson-Van Cittert [4]. A preliminary test performed on actual data showed that the maximum-likelihood method was able to resolve three very closely spaced peaks where the Jansson algorithm failed. In addition, it was found that the Jansson algorithm was more susceptible to noise than the maximum-likelihood method. Further tests using both resolution techniques on both simulated and actual data are planned.

1. Gray, A. J., Beecher, D. E., and Olson, M. V., "Computer-Based Image Analysis of One-Dimensional Electrophoretic Gels Used for the Separation of DNA Restriction Fragments," Nucleic Acids Research, 12(1):473-491, 1984.

2. Hiroaka, Y., Sedat, J. W., and Agard, D. A., "The Use of a Charge-Coupled Device for Quantitative Optical Microscopy of Biological Structures," Science, 28:36-41, October 1987.

3. Snyder, D. L., Miller, M. I., Thomas, Jr., L. J., and Politte, D. G., "Noise and Edge Artifacts in Maximum-Likelihood Reconstructions for Emission Tomography," IEEE Transactions on Medical Imaging, MI-6(3):228-238, 1987.

4. Jansson, P. A., Hunt, R. H., and Plyler, E. K., "Resolution Enhancement of Spectra," Journal of the Optical Society of America, 60(3):596-599, 1970.

E-3. Maximum-Likelihood Estimation Applied to Electron-Microscopic Autoradiography

Personnel: M. I. Miller, BCL and Electrical Engineering
D. R. Maffitt, BCL
B. Roysam, BCL
J. E. Saffitz, M.D., Ph.D., Pathology and Medicine
L. J. Thomas, Jr., BCL

Support: RR 01380
HL 17646

A new method for analysis of electron-microscopic autoradiographs has been described [1] (PR 21, E-6) which is based on the maximum-likelihood method of statistics for estimating the concentration of radioactively labeled substances within organelle structures. A Poisson statistical model describing the autoradiographic grain distributions is adopted, which we prove results from the underlying Poisson nature of the radioactive decays as well as the additive errors introduced during the formation of the grains. Within the model, an iterative procedure derived from the expectation-maximization algorithm of mathematical statistics is used to generate the maximum-likelihood estimates. The algorithm has the properties that at every stage of the iteration process the likelihood of the data increases; and for all initial non-zero starting points the algorithm converges to the maximum-likelihood estimates of the organelle intensities.

The maximum-likelihood (ML) method, and preliminary evaluations of the quantitative accuracy of the ML and crossfire-analysis algorithms using simple geometries have been reported [1-7] (PR 22, 23). Previous studies have focused on simple image geometries. Recent progress has extended the application of the ML method of electron microscopic autoradiography (EMA) to real EMA images. Results from the first EMA experiment analyzed with the ML method and results from simulation studies using real EMA images are outlined below.

Data Acquisition System.

The development of the data acquisition system EMAMAP is now complete [8]. EMAMAP is a program written in C and installed on a dedicated MASSCOMP computer interfaced to a GTCO graphics tablet. In this system, a trained operator places an electron micrograph on a graphics tablet and hand-digitizes the edges of the desired structures and the locations of the silver grains. The system is quite flexible and incorporates a number of advanced graphics features, including editing of structures and contour filling. The output of the program is a coded, segmented image which quantitatively represents the exact geometry of the line structures (e.g. nuclear membrane), regions (e.g. mitochondria), and silver grains.

One of the more advanced features of EMAMAP is the coding algorithm used for storage of the segmented image. A typical image acquired by this

system had dimension 300 by 400, or over 100k pixels. Storage of this image by standard methods would require the same number of bytes of external storage. We have developed an algorithm for encoding the information in the image which achieves a dramatic reduction in the amount of external storage. This method encodes the image as a quadtree [9], then in a second step encodes a pre-order traversal of this tree by Huffman coding [10]. The optimal Huffman codes are uniquely determined for each image and are written as part of the output. In actual use, this coding algorithm has consistently achieved data compression ratios of over 25:1.

ML Analysis of a Real Experiment.

The method for the maximum-likelihood estimation of radioactive concentrations developed above was applied to the experimental data of Dr. Jeffrey Saffitz, Department of Pathology [11]. Neonatal rat cardiac fibroblasts were incubated with ^{3}H arachidonic acid in vitro for 48 hours. Cells were processed for EMA to delineate the subcellular distribution of phospholipids containing the radiolabeled fatty acid. The experimental data consisted of 560 grains distributed over 41 micrographs which were analyzed for seven different types of subcellular structures.

The organelle geometries and the grain locations were acquired by the data-acquisition system, EMAMAP. The geometries of the structures in a real micrograph are much more complicated than were the rectangles used in simulation studies. In particular, the membrane structures are only a single pixel wide and have total areas 2 orders of magnitude less than that of the larger area structures. It must be pointed out that for the ML method, there is no need for us to define the ad hoc rim compartments that are necessary in the crossfire method for organelles with little area and high radioactivity.

Figures 1 and 2 show the results of the maximum-likelihood method for this experiment. Figure 1 depicts the maximum-likelihood estimates of the radioactive concentrations for each of the seven organelle types considered. The nuclear membrane was hypothesized to have a high activity level, and this was confirmed by the ML method. A biologically significant result of this experiment is the observation that the cell membrane has a significantly higher activity than earlier supposed by other experimenters. In fact, the fundamental intent of this experiment was to confirm this fact, which was hypothesized by Saffitz et al. from fundamental biochemical considerations. A notable success of this experiment is that it produced biologically meaningful estimates with very little data in comparison to the typical data requirements of the crossfire-analysis method. Figure 2 represents the relative area occupied by each organelle type in all micrographs. We observe that the cell and nuclear membranes occupy very little area, although they are the loci of the most intense biological activity.

Real-Data-Based Simulator.

Perhaps the most fundamental problem in EMA today is the lack of statistical certainty afforded investigators when designing experiments and producing estimates of physiological phenomena. While modern methods are

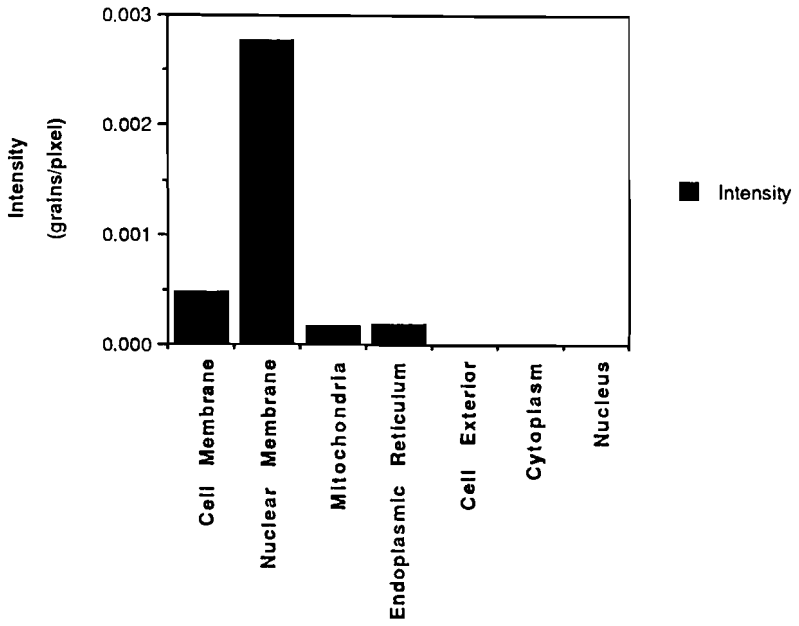

Figure 1. ML Estimates from real experiment [11].

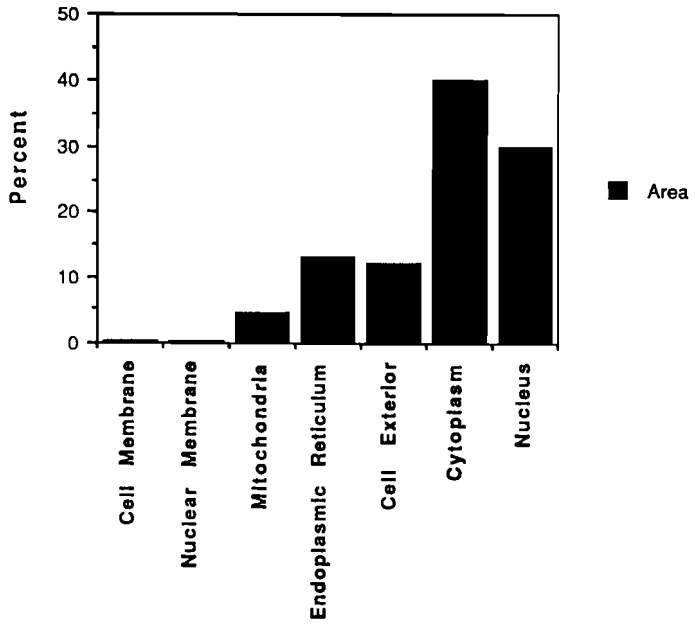

Figure 2. Percent of total area by organelle type for real experiment [11].

supposed to produce quantitative rather than qualitative measures of tracer concentrations, there presently exists no theory or procedure for determining experimental design, data collection requirements, and statistical bounds of estimators. Toward this end we have made progress in the design and implementation of an EM autoradiographic simulator which produces with every experiment a statistical measure of the accuracy of the estimates produced.

The observed data in an EMA experiment consists of images incorporating the geometric information inherent in the micrographs and a set of grain locations. These grain locations represent one realization of a Poisson point process with intensity given by the concentration of the radioactive tracer. This is enough information to compute one estimate of the radioactive concentration. In order to determine error bounds for this estimate, we need to generate ensemble statistics computed over a large number of realizations.

A study involving 100 simulated realizations has been completed for the experiment discussed above. In Figure 3, the solid bars represent the ML estimates for each of the organelles as in Figure 1. The grey bars depict the means of the estimates of the intensities in each of the organelles for 100 realizations. The error-bars define a range of one standard deviation on either side of the mean. A salient observation possible from these results is that the error bars are much wider for first and second organelles, which correspond to the cell-membrane and the nuclear membrane respectively. The accuracy of the method is so high for the other structures that the error bars are barely visible.

Performance Comparison of the Maximum-Likelihood (ML) and Crossfire (CF) Methods on Real Data.

Current quantitative methods for EM autoradiography employ the Crossfire-Analysis method of Blackett and Parry [12-14] and Salpeter et al. [15,16]. These methods account for image-spread by minimizing a chi-squared error-statistic. The statistic is based on the computation of a set of inter-compartment transition probabilities (also known as crossfire probabilities) which we term the transition probabilities

$$P(m|i) = \left(\frac{1}{A_i}\right) \int_{u \in C_m} \int_{x \in C_i} p_e(u - x)\,dx\,du \,, \qquad (1)$$

where $p_e()$ is the point-spread function, A_i is the total area of the source compartment i, and C_i and C_m are the regions occupied by the source compartment i and the grain compartment m respectively.

The masking method [16] is commonly used for computing the transition probabilities. It uses transparent plastic overlays (masks), each containing a number of equally probable source-grain pairs denoting the relative positions of a hypothetical point source of radiation and a grain resulting from that point source. The CF analysis is sensitive to

the accuracy of the transition probabilities, and the transition probability estimates generated by the masking procedure depend on the number of mask points used. We also recognize that a true evaluation of transition probabilities involves the integration of the point-spread function over continuous regions. This corresponds to the use of an uncountably infinite number of mask-points. In this context, in comparing the ML and CF methods in simulations, we have chosen to avoid a masking procedure and generate the transition probabilities by numerically evaluating the integral of Equation 1 using a computer.

The computation of transition probabilities involves a fourth-order integral representing two successive area integrals of the point spread function over the two regions involved. The CPU time required by this computation was made practical by the reformulation of Equation 1. By approximating each region's boundary by a poly-line composed of horizontal and vertical line segments, the two area integrals become line integrals on the boundaries.

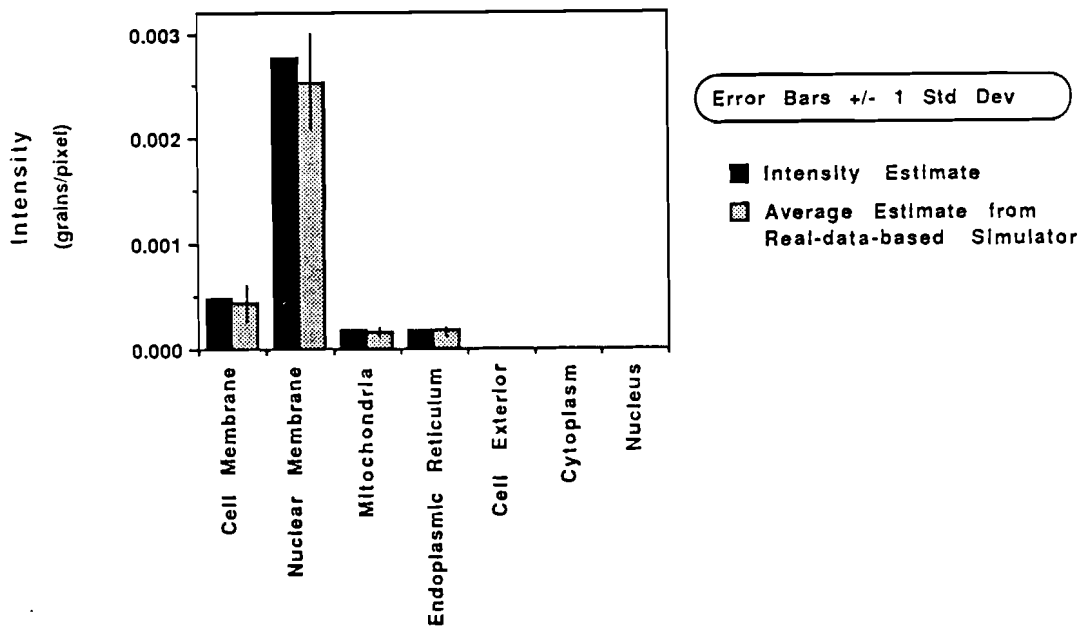

Figure 3. Results from Real-Data-Based Simulator on real experiment [11]. Black bars are the real experiment's estimates. Gray bars are the average estimates from 100 simulated experiments.

In a preliminary study, five images with horizontal and vertical boundary tracers were generated from real experiment images used above. Figure 4 shows the results of this study. The solid bars show the assigned intensity for each of the seven organelles used to generate 100 realizations of a five-image experiment. The cross-hatched bars represent the mean ML-method estimate over the 100 realizations. The clear bars indicate the mean CF-method estimate over the 100 realizations. The error bars represent plus and minus one standard deviation.

The poor performance of the CF method in this study illustrates the important role rim-compartments play in CF analysis. Without rim-compartments to adequately account for image spread from organelles with little area (e.g. nuclear membrane), the intensity tends to be assigned to the large area organelles. In contrast, the ML method performs well without the need to define rim-compartments. Work is currently underway to account for rim-compartments in our implementation of the CF method.

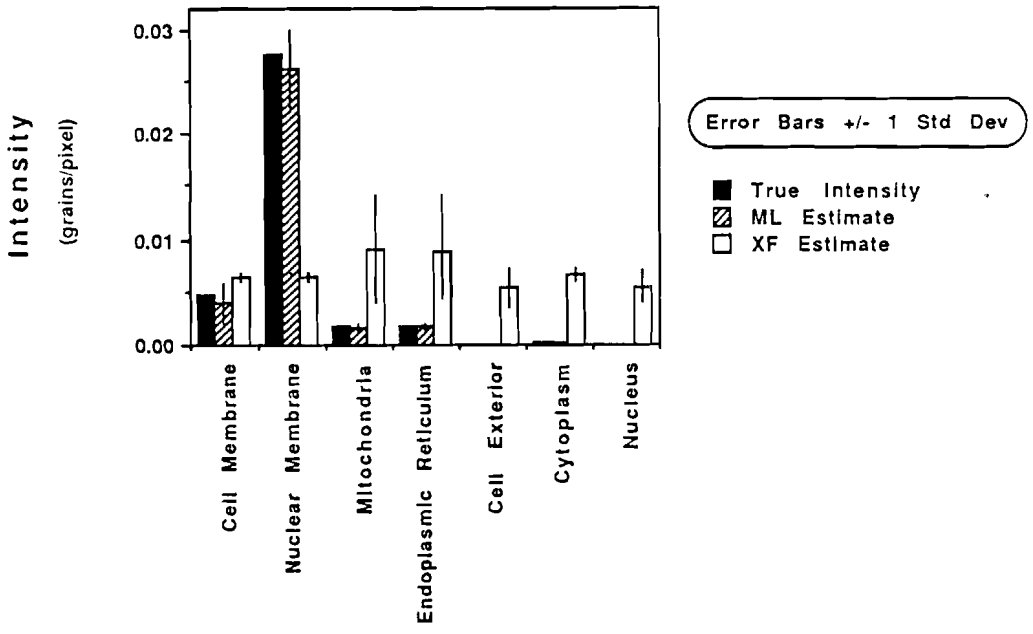

Figure 4. Comparison of ML and CF methods on a 5-image experiment simulated 100 times.

Small System Implementation.

An important new contribution toward the realization of portable software package to perform EM autoradiographic experiments on small computers, such as the IBM PC/AT, was made by reformulating the problem of computing grain-organelle probabilities in terms of line integrals taken around the boundaries of structures rather than as area integrals over the regions defining the organelles. This allows us to store only the coordinate sequences defining object-boundaries, instead of the entire two-dimensional image array. Accordingly, both the memory and CPU requirements of the method can be met by currently available personal computers.

A software package (EMA/PC) is being developed to implement the entire ML method on IBM and compatible personal computers.

EMA/PC is composed of 3 subsystems:

1) Data Entry System (DES).

2) Image Summary Generator (ISG).

3) Estimate Generator (EG).

The DES is a device-independent graphics package written in C using a graphics package called HALO. It allows the experimenter to manually digitize and segment electron micrographs using a locator device such as a graphics tablet. It incorporates an image-editing capability and allows for the device-independent input of important experimental parameters such as the half-distance of the point-spread function. It is capable of functioning with any combination of 14 different graphic locator devices, 34 different display devices and 28 different hardcopy devices. DES incorporates some detailed features that facilitate the process of archiving, documenting and keeping track of experiments.

The ISG computes the grain-organelle probabilities and object dimensions from the image files generated by DES. It is currently designed for the point-spread function for tritium.

The EG is a straightforward implementation of the iterative expectation-maximization algorithm for maximum-likelihood estimation of radioactive intensities for the organelle types of interest.

1. Miller, M. I., Larson, K. B., Saffitz, J. E., Snyder, D. L., and Thomas, Jr., L. J., "Maximum-Likelihood Estimation Applied to Electron-Microscopic Autoradiography," Journal of Electron Microscopy Technique, 2:611-636, 1985.

2. Miller, M. I., Larson, K. B., Saffitz, J. E., Snyder, D. L., and Thomas, Jr., L. J., "Maximum-Likelihood Estimation Applied to Electron-Microscopic Autoradiography," Cell Biology, 101(5):85a, 1985 (part 2 abstract).

3. Miller, M. I., Roysam, B., Saffitz, J. E., Larson, K. B., and Thomas, Jr., L. J., "Validation of Maximum-Likelihood Analysis of Electron Microscopic Autoradiographs," Proceedings of the 70th Annual FASEB Meeting, St. Louis, MO, 45(3):470, 1986 (abstract).

4. Roysam, B., "A New Method for EM Autoradiography: Validation and Comparison to Crossfire Analysis," Department of Electrical Engineering, Washington University, St. Louis, MO, May 1987 (Master of Science Thesis).

5. Miller, M. I., Roysam, B., Saffitz, J. E., Larson, K. B., and Thomas, Jr., L. J., "A New Method for the Analysis of Electron Microscopic Autoradiographs," Biotechniques, 5(4):322-328, 1987.

6. Roysam, B., "A New Method for EM Autoradiography: Evaluation and Comparison to Crossfire Analysis," Joint Meeting of the Electron Microscopic Society of America, August 1988.

7. Roysam, B., "A New Method for EM Autoradiography: Small System Implementation," Joint Meeting of the Electron Microscopic Society of America, August 1988.

8. Fuhrmann, D. R., Brown, M. A., Miller, M. I., Roysam, B., Saffitz, J. E., and Thomas, Jr, L. J., "A Data Acquisition System for Maximum-Likelihood Analysis of Electron Microscopic Autoradiographs," Journal of Electron Microscopic Technique, 7:(3)199-204, November 1987.

9. Samet, H., "The Quadtree and Related Hierarchical Data Structures," ACM Computing Surveys, 16:187, 1984.

10. Huffman, D., "A Method for the Construction of Minimum-Redundancy Codes," Proceedings of IRE, 40:1098, 1952.

11. Knabb, M. T., Saffitz, J. E., Corr, P. B., and Sobel, B. E., "The Dependence of Electrophysiological Derangements on Accumulation of Endogenous Long-Chain Carnitine in Hypoxic Neonatal Rat Myocytes," Circulation Research, 58(2):230-240, 1986.

12. Blackett, N. M., and Parry, D. M., "A New Method for Analyzing Electron Microscopic Autoradiographs Using Hypothetical Grain Distributions," Journal of Cell Biology 57:9, 1973.

13. Blackett, N. M., and Parry, D. M., "A Simplified Method of Hypothetical Grain Analysis of Electron Microscopic Autoradiographs," Journal of Histochemistry and Cytochemistry, 25(3):206-214, 1977.

14. Blackett, N. M., and Parry, D. M., "Analysis of Electron Microscope Autoradiographs Using the Hypothetical Grain Analysis Method," Journal of Microscopy (Oxf), 106:117-124, 1976.

15. Land, B., and Salpeter, E. E., "Basis for a Computer Program for Mask Analysis of EM Autoradiographs," Journal of Cell Biology, 76:142, 1978.

16. Salpeter, M. M., McHenry, F. A., and Salpeter, E. E., "Resolution in Electron Microscopic Autoradiography - IV," Journal of Cell Biology, 76:127-145, 1978.

E-4. Automated Segmentation of Biomedical Images

Personnel: D. R. Fuhrmann, BCL and Electrical Engineering
M. A. Brown, BCL
J. E. Saffitz, M.D., Ph.D., Pathology and Medicine
L. J. Thomas, Jr., BCL

Support: RR 01380
HL 17646

This year, work on the automated segmentation of electron microscopic cell images was brought to a close. It was felt that over the past three years we had developed a very useful software package for relatively error-free image acquisition by hand-digitization and that further work to automate the process by computerized image segmentation would be insufficiently productive.

The tangible result of our efforts is the software package EMAMAP, which is described in PR-23, E-4, and has been reported in [1]. In the present system, a trained operator places a micrograph on a graphics tablet and hand-digitizes the edges of biological structures. The edges are labeled according to their biological type at the time they are drawn. Those edges which form closed contours in the interior of the image are filled automatically with the correct region label using a contour-filling algorithm. The image is then coded for efficient storage using a hybrid quadtree/Huffman coding scheme.

Several new features have been added to EMAMAP. The program was made more flexible in that the operator can enter the edge-tracing mode at any time in the program, even after region filling. Automatically filled regions can be manually re-labeled by the operator if desired. A new method of coding the edge information using chain codes, for intermediate storage of the edges only, was incorporated. A new, more compact image header contains information about the coded images. Finally, the algorithm for image coding was incorporated directly into EMAMAP; previously it was a separate experimental program which took as its input the full images created by EMAMAP.

A study of automated image segmentation using statistical texture segmentation functions was carried out. The basic segmentation algorithm studied was the Split-Merge-Group-Join (SMGJ) algorithm, which is based on the quadtree description of the image. This algorithm provides a framework for classifying image pixels using a texture measure which is chosen independently. Law's Texture Energy Measures and Co-occurrence Probability

Measures were chosen for detailed study. We concluded that this approach offered little promise for a reliable image segmentation algorithm for use on the class of EMA images considered in this study.

The EMAMAP program has been used to gather data for an experiment studying the degradation of membrane phospholipids in reversibly and irreversibly injured cardiac muscle cells. In the experiment 90 micrographs containing 1296 silver grains were digitized to a total of 22.5×10^6 pixels. The experimental conclusion was that the critical metabolic events in the degradation of the phospholipids were localized in the cell sarcolemma. This result was not known from previous experimental methods and has significant clinical implications.

Future plans for the use of EMAMAP include the data acquisition for an experiment in the localization of adrenergic receptors in cardiac muscle cells.

Other BCL personnel have studied a reformulation of the computation required in the maximum-likelihood method and have developed a modified data acquisition system suitable for implementation on a PC-class computer (E-3).

1. Fuhrmann, D. R., Brown, M.A., Miller, M. I., Roysam, B., Saffitz, J. E., and Thomas, Jr., L. J., "Data Acquisition System for Maximum-Likelihood Analysis of Electron Microscopic Autoradiographs," Journal of Electron Microscopy Technique, 7(3):199-204, November 1987.

E-5. Radiation Treatment Planning

Personnel: F. U. Rosenberger, BCL and Computer Systems Laboratory
W. R. Binns, Ph.D., Physics
J. W. Epstein, Physics
W. S. Ge, M.S., Radiology
W. B. Harms, B.S., Radiology
S. S. Hancock, Ph.D., Medical College of Ohio
M. H. Israel, Ph.D., Physics
J. Klarmann, Ph.D., Physics
J. W. Matthews, D.Sc., Computer Systems Laboratory
J. A. Purdy, Ph.D., Radiology
J. W. Wong, Ph.D., Radiology
X. Ying, D.Sc., Radiology
C. W. Yu, M.S., Radiology

Support: RR 01380
RR 01379
CA 41574
CA 42993
CM 47715
AW Company
Mallinckrodt Institute of Radiology

This work is centered in the Mallinckrodt Institute of Radiology and represents a set of activities targeted to providing more effective radiation therapy treatment of cancer. A more extensive description of some of these activities was given in PR 23, Section C. Major activities include: evaluation of high-energy photon external-beam treatment planning; development of a rapid area dosimetry system; an online radiotherapy imaging system; development of new algorithms for electron dose deposition; and development of methods for verifying actual dose delivered to patients by quantitative use of exit-dose data. These activities provide a broad attack on some of the present limits to effective radiotherapy treatment of cancer.

An MMS-X high-performance graphics system developed at IBC and on loan from BCL is in use for display and operator evaluation of treatment plans. Its ability to interactively display and modify beam-eye views of treatment plans has been extremely valuable and provides a capability that has only recently become practical with advanced raster-scan graphics systems. Remote access has been provided via IPAQ (Section F) and the Campus-Wide Network to allow investigators in Radiation Physics extensive use of IBC computer facilities and programs for calculation, plotting, data transfer, and storage.

A major new activity carried out by Drs. Wong and Ying has been the investigation of quantitative treatment verification using exit-dose measurements and 3-D patient data. Verification must take into account the fact that patient characteristics and orientation may change from treatment to treatment. Measured exit-dose distribution and patient CT data can be used to calculate primary intensity in the patient, ignoring scatter. The

primary intensity is then used to calculate a new exit-dose distribution including scatter effects. The difference between that calculated exit dose and the measured dose can then be used to correct the initially calculated primary and a new, more accurate calculation of exit dose performed. This can be repeated until sufficient agreement between calculated exit dose and measured exit dose is achieved, after which the dose to the patient can be calculated from the primary that has been determined during this procedure. It can be shown that the procedure must converge to the correct primary intensity if the primary dominates the exit dose and there is no "error" in the CT data.

The comparison of calculated with measured exit dose distributions provides information about "errors" in the CT data which may be due to changes in the patient geometry or positioning. Finally, if a model is available for changes in the patient, for example, changes in lung volume or density, an iterative procedure may be used to estimate these changes, and the actual dose delivered to the patient. These techniques, along with new methods under development for exit-dose measurement (PR 23, C-3), promise to make greatly improved verification of treatment delivery possible, even to the extent of adaptively modifying treatment as it progresses, thereby better meeting the treatment objectives.

E-6. EM Algorithms Incorporating Monotonicity Constraints for Removing Recovery-Related Distortion from Auditory-Nerve Discharge Patterns

Personnel: M. I. Miller, BCL and Electrical Engineering
N. Karamanos, BCL
K. E. Mark, BCL

Support: NS 23007

A new method for the analysis of auditory-nerve discharge patterns has been developed. This method models neural discharge as a self-exciting point process (SEPP) in which the intensity is given by the product of two functions $s(t)$ and $r(\tau)$. The function $s(t)$ depends on the acoustic stimulus. The recovery related function $r(\tau)$ depends on the history of the process and is assumed to be a monotonic function of time. Using maximum-likelihood estimation (MLE) techniques, the functions $r(\tau)$ and $s(t)$ are jointly estimated from the auditory-nerve discharge data.

Since the joint MLE equations are coupled, analytic closed form solutions for $s(t)$ and $r(\tau)$ do not exist. An iterative expectation maximization (EM) algorithm has been derived to compute the maximum-likelihood estimated (MLEs) of $s(t)$ and $r(\tau)$. This EM algorithm has been implemented and the following results are based on its use.

The EM algorithm has been shown to perform well under the typical conditions of neural discharge based on simulations. The simulation

parameters, s(t) and r(τ), were chosen to closely match the maximum-likelihood estimates from a population of auditory-nerve fibers in response to a 1-kHz tone stimulus. Using these simulation parameters and the SEPP model, auditory-nerve discharge data were simulated until a threshold number of events were generated. From the simulated data, the functions s(t) and r(τ) were estimated using the EM algorithm. The MLEs were found to be very slightly biased when a threshold of 1000 events was used. However, as the threshold was increased to 2000 and 4000 events, the bias of the estimates decreased. This result verifies the asymptotically unbiased behavior of the MLEs.

Two populations of nerve fibers have been analyzed using the EM algorithm method. The first population consists of 142 nerve fibers stimulated by a 1-kHz tone; the second consists of 206 nerve fibers stimulated by a 3-kHz tone. The following results were obtained through this analysis:

1) The MLE of s(t) is a scaled version of the post-stimulus time (PST) histogram.

2) Neurons have widely varying recovery functions r(τ).

3) Evidence indicates that the recovery function exhibited by a nerve fiber varies with the average firing rate.

4) Low-spontaneous-activity neurons seem to form a separate subgroup in that their recovery functions are markedly less steep.

5) The adopted SEPP method models neural discharge better than an inhomogeneous Poisson model.

6) The statistical effect of the recovery function is to reduce the variability of the large synchronized components in the temporal discharges of response, to well below that predicted by a Poisson model, while having little effect on the variability of small synchrony coefficients.

We are currently using the EM algorithm method to analyze a population of nerve fibers stimulated by a speech stimulus. This analysis will provide further information on the appropriateness of the SEPP model and on the encoding of broadband speech stimuli in auditory-nerve discharge data.

E-7. Color Perimetry Studies

Personnel: W. M. Hart, M.D., Ph.D., Ophthalmology
R. Nesher, M.D., Ophthalmology
S. R. Phillips, BCL
G. L. Trick, Ph.D., Ophthalmology

Support: RR 01380
EY 06582
Washington University

This project is in continuing support of a multi-year prospective follow-up study of patients with known and suspected glaucoma. Principal instrumentation development for this project has been a microcomputer-driven controller for a color-video display processor used to generate stimuli for clinical visual field testing. During the past project year, modifications to the software of the system have allowed testing with target-background combinations of differing color combinations from those previously used. Current work underway is additional software development to convert the instrument from use solely as a manual kinetic perimetric device to its use as an automated static perimeter for constant-luminance color-contrast testing.

1. Hart, W. M., Trick, G. L., Nesher, R., and Gordon, M. O., "The Effect of Glaucomatous Damage on Static Perimetric Thresholds Determined with Luminance Increment and Blue/Yellow Color Increment Thresholds," Investigative Ophthalmology and Visual Science, 29:422, 1988.

2. Hart, W. M., "Blue/Yellow Color Contrast Perimetry Compared to Conventional Kinetic Perimetry in Patients with Established Glaucomatous Visual Field Defects," presented at the 8th Meeting of the International Perimetric Society, Vancouver, Canada, May 9, 1988.

E-8. Theory, Analysis, and Applications of Massively Parallel Processing

Personnel: K. R. Smith, BCL
M. I. Miller, BCL and Electrical Engineering
R. E. Morley, Jr., D.Sc., Electrical Engineering
B. Roysam, BCL

Support RR 01380

Massively parallel processors represent a new class of computer architectures featuring mesh-connected arrays of bit-serial processing elements on a single integrated circuit. This class of parallel architectures offers a major increase in computational speed over

conventional machines in applications for which the computations may be restructured so that the operations required involve local data passage. A broad class of biomedical estimation problems have potential applicability on massively parallel processors due to the nature of the computations associated with estimation problems. Specifically, estimation problems have some form of a cost function which is to be minimized in order to arrive at the estimate. Such function minimization problems map quite naturally onto massively parallel architectures.

The primary focus of our work has been to develop a unified programming methodology for embedding rule-based, regular-grammar constraints onto massively parallel processors. We have recently taken a major step toward this goal by proposing the unification of syntactic grammars and stochastic optimization through the representation of regular grammars via their equivalent stochastic representations [1]. This allows for a unified solution of stochastic estimation and/or statistical pattern recognition problems over rule-generated constraint spaces. The basic approach taken has been to establish the formal connection of rules to Chomsky grammars, and to generalize the original work of Shannon on encoding rule-based channel sequences from Markov chains of the same entropy. By embedding the rules using the principle of maximum entropy, constrained spaces corresponding to the Chomsky regular grammars are generated by sampling Gibbs distributions whose entropy corresponds to the logarithm of the total number of sequences in the regular language, and whose domain corresponds to legal derivations of the grammar. By using the principle of maximum entropy, more general regular-like languages in multiple dimensions may be generated which have the property that the set of sequences in the constraint space are all equi-probable under the Gibbs measure and correspond to Shannon's "equi-probable, weakly-typical" set. Our unified programming method is subsequently derived by modeling the massively parallel architecture as a Markov random field which allows us to map the Gibbs distribution containing the grammar directly onto the massively parallel architecture.

Although our programming method applies to an array of applications in biomedical imaging, our initial emphasis has focused on the computer-vision problem of boundary tracing. By modeling the boundary tracing problem as a Markov random field, we are able to utilize our programming theory to embed rule-based constraints into the boundary-tracing process which then allows us to perform a constrained maximum-likelihood estimation of the boundaries through a simulated annealing procedure. This technique allows a fully parallel boundary-tracing process which executes orders of magnitude faster than serial boundary tracing. The power of our theory and methods is the ability to embed high-level heuristic constraints into our programming model which can then be computed in a massively parallel processing environment.

The future of this research calls for refinement of our programming method to include rules and constraints which do not fall into the regular language category. We plan to perform experiments and simulations which examine the effects of these different languages on constrained estimation problems. We are also interested in the massively parallel computer models which could perform these more complicated estimation algorithms. As with

our previous theoretical results and the boundary tracing algorithm, these experiments will be executed on the 1024 processing element Distributed Array Processor (DAP) manufactured by Active Memory Technology.

1. Miller, M. I., Roysam, B., Smith, K. R., and Udding, J. T., "Mapping Rule-Based Regular Grammars to Gibbs Distributions," AMS-IMS-SIAM Joint Conference on Spatial Statistics and Imaging, American Mathematical Society, July 1988.

F. Resource Development Activities

Resource development activities are those which contribute to the goals of more than one major program of the laboratory, address the needs of individual users who can benefit from the expertise of the BCL staff and the inventory of computing and specialized test equipment, or identify new technologies which may become appropriate foundations for new experimental tools. Service to users does not follow the usual computation-center pattern with an established fee schedule and a highly centralized facility. Rather, senior laboratory staff members consider requests for assistance from investigators who must address a particular biomedical computing problem. If an appropriate technology exists, investigators may be referred to commercial vendors or fee-for-service organizations when these are available. In other cases, problems may be approached by the laboratory provided that the effort complements other activities of the laboratory. Many times the project can be assigned to a staff member with appropriate experience and completed in a short time. The investigator then has his or her results, and a short note describing the work will appear in the annual report and perhaps the open literature. A few projects, however, may develop into major initiatives within the laboratory. Most of the major projects began in this fashion and the opportunities that supporting activities provide are valued.

The IPAQ project (F-1 thru F-6) has focused laboratory efforts on providing a computational environment which can be utilized in addressing the demanding needs of algorithm development. A distributed approach, multiple computing systems integrated with communication networks, is being developed. Equipment acquisition and system integration continue to be major activities, with more effort now directed to improving the image display and manipulation environment (F-4, F-9).

Network related activities at the University have accelerated during the past year, with the Resource serving as a major participant in these developments (F-7, F-5). The installation of the Biomedical Research Network has already influenced Resource activities and access to supercomputers may have an even greater impact.

Evaluation of a reflectance camera (F-8) for acquisition of biomedical images is an important first step to providing better methods for improving image quality and acquisition techniques. Likewise, exploration of various hardware systems (F-6) will stimulate new ideas for better implementations of complex, computationally demanding algorithms.

F-1. A Distributed Facility for Image Presentation, Analysis and Quantification (IPAQ)

Personnel: G. J. Blaine, BCL
M. A. Brown, BCL
K. W. Clark, BCL
J. R. Cox, Jr., BCL
H. A. Drury, BCL
R. E. Hermes, BCL
S. M. Moore, BCL and Medicine
S. R. Phillips, BCL

Support: RR 01380
Digital Equipment Corporation
Washington University

Decentralized computing organized along departmental and research laboratory lines characterizes the environment which continues to evolve at most major medical-research institutions. This is particularly true in quantitative imaging where many projects have diverse image-data sources (modalities), different data-acquisition requirements, and dissimilar methods for the extraction of quantitative information. Rather naturally, diverse computing styles and equipment choices have evolved. For example, our major collaborative research groups support installations tailored to their specific measurement and picture transformation needs, for which display peripherals from a variety of manufacturers (DeAnza, Ramtek, and Lexidata) are tightly coupled to different computers (DEC 750 & 780, MicroVAX II, PE 3230 & 3242). Commonality is limited to little more than the popularity of Vax-class computers and a FORTRAN programming environment. Furthermore, the lack of common program-development tools and display-support software has minimized the opportunities for sharing developments across research programs and has necessitated large host-specific investments by those Resource researchers and collaborators who participate in modeling and algorithm development.

Algorithm development is often characterized by computationally demanding and memory-intensive tasks which must compete with concurrent usage of the existing computing resources for data acquisition and analysis activities. The limited computational capacity available for algorithm development and pressures for expediting the research process biases the investigator's attention toward ad hoc approaches to improvements in execution performance, often at the expense of fundamental algorithm studies which are more likely to yield long-term benefits.

The broad goal of this activity is to create an environment for biomedical image presentation, analysis and quantification (IPAQ) which:

1) is focused on fundamental algorithm developments that individual biological scientists may not have the expertise, time, patience or resources to pursue;

2) provides an integrated approach to expedite the development and export to the local and national communities of new algorithms for improved quantification of biological information;

3) improves access for purposes of algorithm development to data from the diverse imaging modalities to encourage modality integration; and,

4) protects existing investments in decentralized and specialized biomedical research systems.

The IPAQ facility includes: 1) acquisition nodes consisting of specialized imaging resources; 2) computation-oriented nodes to support development and initial evaluation of algorithms; 3) computation/display nodes which are tailored to export specialized computation and/or picture presentation; and 4) a high-bandwidth network to interconnect nodes within the Resource as well as provide access to other resources within the local and national research community.

Computer systems integration and software development continue as principal activities. Specifics of these activities are described in sections (F-2 thru F-6). Figure 1 illustrates the current system-resource configuration.

In order to maintain a current knowledge of new hardware and software products, product evaluations and hardware/software field tests have been performed for several vendors including Sun Microsystems, IBM, and Digital Equipment. Close involvement with the development and installation of the Biomedical Research Network and the Campus-Wide Network continues as an important part of the IPAQ activity.

Support of the IPAQ facility and its users is eased by the availability of a series of locally-generated references: the IPAQ User's Notebook, Document Preparation Binder, and Revision Control System Reference (RCS). These references are not intended for use as computer recipe books, but rather, are intended as guides to assist the resource users in getting started by identifying available software and hardware, supplying pointers to detailed documentation, and providing helpful hints for effective resource utilization.

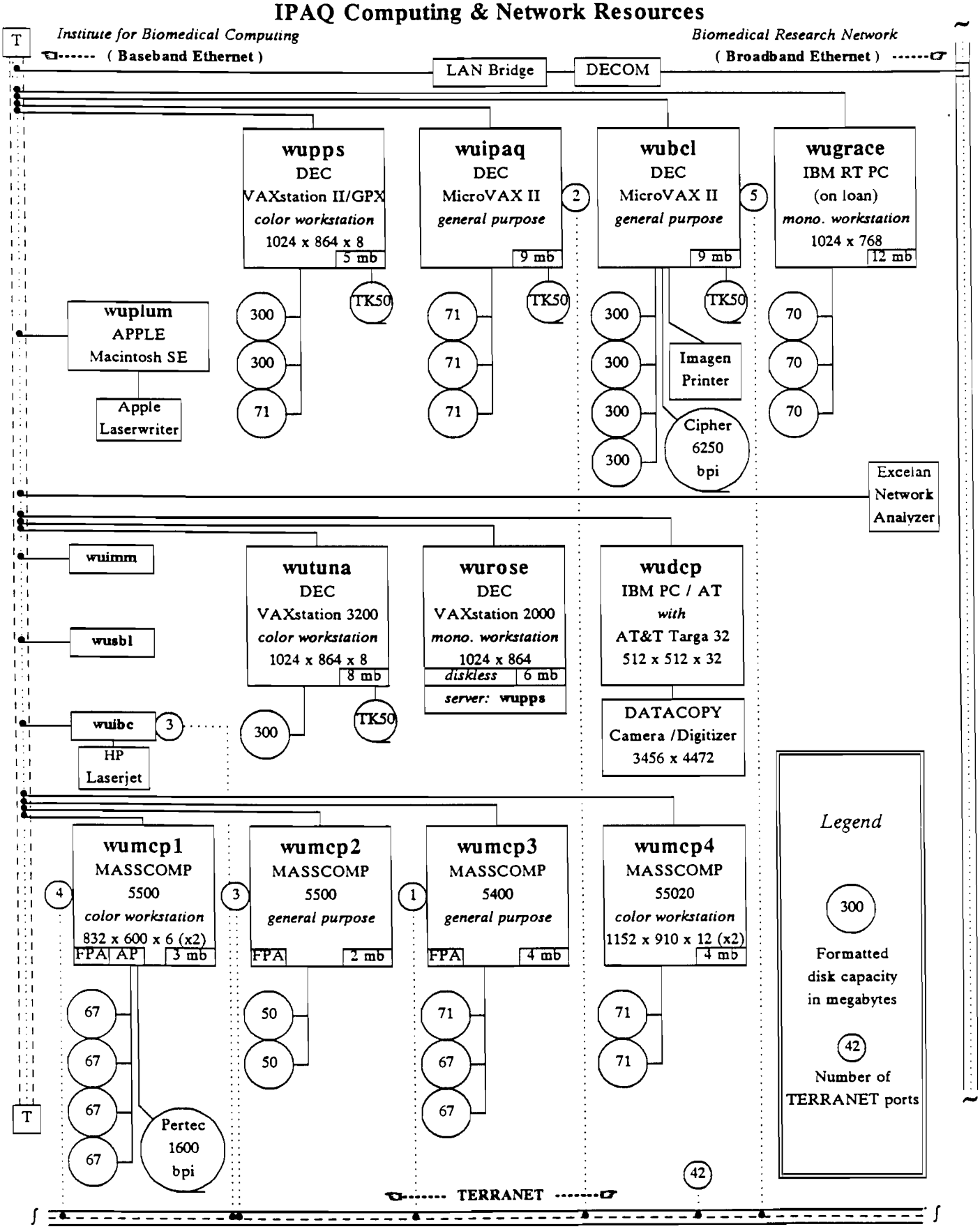

Figure 1. IPAQ Computing & Network Resources

F-2. IPAQ: System Integration

Personnel: R. E. Hermes, BCL
M. A. Brown, BCL
K. W. Clark, BCL
S. R. Phillips, BCL
D. A. Schwab, BCL

Support: RR 01380
Digital Equipment Corporation

Computer system acquisition and integration continues to be a major activity of the IPAQ working group. A monochrome VAXstation 2000 and a color VAXstation 3200 were acquired. A MicroVAX II (nodename: WUCON) was eliminated. An IBM PC/RT has been available as an evaluation unit on loan from IBM. An Apple MacIntosh SE and Laserwriter laser printer were also acquired for use in preparation of presentations and publications.

The VAXstation 2000 is a diskless monochrome graphics system which is being used in development of window-based user interfaces and for document preparation. The VAXstation 3200 is a high performance graphics workstation with 1024x832x8 bits of image memory. The system is used for development of windowing software and computation. The IBM PC/RT is a RISC-processor-based workstation with a monochrome graphics adaptor. The system is used for computation, graphics display, and for evaluation of the Carnegie Mellon Andrew system, IBM,s UNIX implementation called AIX, and potentially the MACH operating system.

The data-storage needs of imaging research activities have been met by the addition of seven 300-mbyte disc drives to existing systems. A 40-mbyte disk drive was added to an IBM PC/AT which now hosts a Datacopy reflectance camera and AT&T Targa 32 display system. An additional floating-point processor has been added to an existing MASSCOMP system to provide more computation capability.

A Excelan LANanalyzer network analyzer was acquired for monitoring local network activity as well as for providing a mechanism to test and evaluate the Biomedical Research Network. The network analyzer is hosted by a COMPAQ Portable II personal computer.

F-3. IPAQ: System Support

Personnel: K. W. Clark, BCL
M. A. Brown, BCL
H. A. Drury, BCL
R. E. Hermes, BCL
S. R. Phillips, BCL

Support: RR 01380
Digital Equipment Corporation

The many general-purpose and workstation-class computers from a variety of vendors (DEC, MASSCOMP, IBM, SUN) installed in the last few years have pressed the need for solid systems support. A versatile research environment demands that systems run with up-to-date operating system software. Since last report, two upgrades of the ULTRIX operating system have been installed on the DEC machines; another is scheduled for the near future. The MASSCOMPS have likewise been upgraded. With all machines connected in a local-area network via Ethernet, the process of installing new versions of operating systems has been made easier because some machines may be upgraded with a remote-install (RIS) facility over the network, eliminating the need to load multiple tapes or diskettes. Likewise, many operating-system-independent files can be copied over the network rather than loaded with each system upgrade.

The Network File System (NFS) has been installed on all the DEC machines (and on the MASSCOMPS shortly). NFS permits users direct access to files on other systems without having to "log-in" to those systems. A user's files can be kept in one place rather than spreading copies of identical files around to all machines the user may need. DECNET-ULTRIX has been installed on the DEC machines.

IBM has loaned us an RT PC. The system is currently configured with the Berkeley 4.3 UNIX operating system. The system also has the MIT (Massachusetts Institute of Technology) X-windows graphics system plus Carnegie-Mellon's Andrew Toolkit. The RT PC is Ethernet-linked to the local network of DEC and MASSCOMP machines.

DEC has selected BCL as a field-test site for a new generation of MicroVAXes and for the ULTRIX operating system including windowing software and DECNET-ULTRIX. A test machine is at BCL; the new operating system has been installed on that machine and another VAXstation.

F-4. IPAQ: Image Presentation

Personnel: K. W. Clark, BCL
M. A. Brown, BCL
G. E. Christensen, BCL
H. A. Drury, BCL
G. E. Gutenschwager, BCL
R. E. Hermes, BCL
A. J. Loth, BCL
D. G. Politte, BCL
D. M. Wade, BCL

Support: RR 01380

The influx of many workstation-class machines at BCL (F-2) and the need to visualize PET, DNA-gel, EMA, and optically-sectioned images have demanded good image manipulation and presentation tools. The MIT (Massachusetts Institute of Technology) X-windows (version X11) network-transparent hardware-independent graphics system, already adopted by major graphics system vendors, is being installed on the DEC GPX MicroVAX and VAXstations over a previous version (X10). This X graphics system is unique because it allows remote network access to image displays and graphics devices. Furthermore, the data-transport protocol of the network is transparent to the graphics system. Many utilities are available for X-windows, including image display/manipulation and previewers for various text-processing and graphics software systems such as POSTSCRIPT (Adobe Corporation) and imPRESS (Imagen Corporation). The Carnegie-Mellon Andrew Toolkit is also available on the RT PC. On the MASSCOMP workstation, a locally-developed image manipulation package, MULTI (F-9), has greatly aided BCL staff in visualizing multiple images, including the presentation on the same screen of images of different sizes and from different sources.

F-5. IPAQ: Networking

Personnel: G. J. Blaine, BCL
R. E. Hermes, BCL
S. R. Phillips, BCL
D. A. Schwab, BCL
E. Senol, BCL

Support: RR 01380
Washington University

Close coupling of algorithm research, development and evaluation to the collaborative research areas is facilitated by a communication network which serves to federate distributed resources. Access to data from specialized imaging instruments located in collaborator's laboratories is

important to evaluating algorithm performance. Additionally, the communication network is to support presentation of images to collaborating biomedical scientists. Remote quick-look capability should stimulate increased participation and reduce the time constant in the necessarily interactive evaluations of algorithm performances.

Information interchange between the distributed image-acquisition resources within the medical center, the computation-oriented nodes at the BCL and the presentation nodes (currently located within BCL) can be functionally partitioned into "message" and "service" classes. Two-way query-based conversations are addressed by the "message network." The transport of large data sets for access to measurement and image information is to be supported by bulk-transfer at high rate in a "service network."

Local message-network connectivity is supported by TERRANET (PR 22, F-10). Approximately twenty-five terminal ports, twenty-five computer ports and two telephone-line modems are provided 9600-bps switched-circuit access. Dedicated point-to-point 9600-bps channels on the MIR CATV network provide TERRANET access to remote resources such as the CCU-PET computer as well as terminal support to collaborators in Radiation Oncology.

Our current "service network" uses a baseband-Ethernet LAN which spans the Institute's medical campus facilities. A DEC LAN 100 Bridge supports inter-LAN traffic to the broadband-based Biomedical Research network while minimizing backbone loading. The Ethernet channel supports packet transmission for both DECNET and TCP/IP communication protocols. Digital Equipment's DECNET-Ultrix product installed on several MicroVAX IIs facilitates file transfer from DECNET nodes elsewhere in the University research community. Connectivity to resources at the Engineering School Campus is supported by a 10-Mbps microwave channel (F-7).

F-6. IPAQ: Computation

Personnel: R. E. Hermes, BCL
M. A. Brown, BCL
K. W. Clark, BCL
S. M. Moore, BCL and Medicine
D. G. Politte, BCL

Support: RR 01380

Algorithm development and computation for quantitative imaging is the central activity of the Resource. Satisfying the computing needs of these project areas is a significant part of the IPAQ activity. Attention has been focused on two major goals:

1. the reduction of computation time needed for current studies employing computationally intensive algorithms and

2. understanding the relative performance of different processors to allow prediction of computation times and allocation of computation resources.

The first goal presents a continuous challenge to review algorithm implementations to determine whether all possible software techniques have been used to assure efficient code. Often simple algorithmic or coding changes have shortened computation times significantly. This has been particularly true for algorithms which are iterative.

The second goal is met in two ways. First, by understanding the relative hardware architectural differences of different computation resources, we are able to match certain computation needs to particular resources. As new computer systems become available, we investigate and attempt to evaluate them for local needs. Secondly, the distributed nature of IPAQ resources allows machines to be dedicated to certain tasks as needed. Table 1 shows how machine resources are usually allocated to research activities. As the intensities of activities change, the allocations of resources often change accordingly.

Table 1. Computer Systems and Applications

Nodename	WUIPAQ	WUBCL	WUPPS	WUTUNA	WUROSE	WUGRACE
Application Areas	Networking & Communications	Program Dev. Text Processing	Networking Program Dev. X-Windows Image Display	Program Dev. Computation X-Windows Image Display	Program Dev. X-Windows Graphics	Computation X-Windows Software Evaluation
Nodename	**WUMCP1**	**WUMCP2**	**WUMCP3**	**WUMCP4**	**WUDCP**	**WUPLUM**
Application Areas	Program Dev. Computation Graphics	Text Processing	Program Dev. Computation	Program Dev. Computation Image Display	Program Dev. Graphics Data Acquisition	Text Processing Administrative Use Illustrations

F-7. Campus-Wide Network Program

Personnel: G. J. Blaine, BCL and Radiology
J. R. Cox, Jr., BCL and Computer Science
R. E. Hermes, BCL
R. L. Hill, BCL and Radiology
D. G. Hirsh, B.A., Office of the Network Coordinator
R. G. Jost, M.D., Radiology
S. R. Phillips, BCL
A. P. Rueter, B.S., Radiology
D. E. Schwab, BCL
E. Senol, BCL

Support RR 01380
RR 03522
Digital Equipment Corporation
Washington University

Networking at Washington University

Distributed computing, the decentralized deployment of inexpensive personal workstations and laboratory computers and the sharing of more expensive processing, storage and printing resources has long been the defacto style of computing for researchers at Washington University. At the Biomedical Computer Laboratory (BCL) in 1967 several computers (that would now be called workstations) were connected to the central University computer by twisted wire-pairs and leased telephone lines. This style of networking grew on the campus so that today electronic switches connect more than 1300 terminals and personal computers to computing resources. At the School of Medicine alone, the Medical Computing Facilities serves over 500 users via twisted wire-pairs and a central electronic switch.

Computer networking that allowed direct high-speed transmission of data between computers became popular about 1980. Washington University's Mallinckrodt Institute of Radiology (MIR) began installing DECnet (Digital Equipment Corporation's proprietary computer network) in that year and has developed a large network of computers over the years since then. When Ethernet became available commercially in 1983 several laboratories at Washington University installed this LAN to serve nearby users. In the years that followed, almost two dozen such installations appeared on the two campuses. Baseband signaling is the most common method for Ethernet communication since it provides for inexpensive network taps. Two limitations exist, however: the distance between network nodes cannot exceed 2800 meters and the physical medium can support only one channel.

Work toward a picture archiving and communication system (PACS) was begun in 1982 through a collaborative program between the Mallinckrodt Institute of Radiology and the Biomedical Computer Laboratory. A broadband CATV cable was installed to study the problems associated with picture transmission. This system for PACS development now carries radiological images in both digital and video form to several sites in the School of Medicine.

Several universities, notable among them Carnegie-Mellon, MIT, Stanford, Brown, Johns Hopkins and Dartmouth, have engaged in substantial centrally-funded programs to implement large-scale networks on their campuses. Our approach has recognized the decentralized nature of our research community and provides a focus for establishing connectivity between computing resources both at the individual researcher and departmental levels. Network activities have been funded through a mixture of equipment grants (Digital Equipment Corporation $15 million over three years; Division of Research Resources, Shared-Instrument Grant $300,000, and personnel support from related research activities, the Medical school and the central administration.

Program Organization

To address the issues of a campus-wide network the Office of the Network Coordinator (ONC) was formed in May 1985. The ONC (directed by J. R. Cox, Jr.) is a small organization whose principal role is planning and coordination. A meeting of system managers and interested individuals within the university is hosted monthly. During the Spring of 1988, a technical advisory group was assembled and met on weekly basis to review results and plan testing strategies with which to achieve robust integration of the hilltop and medical school networks.

Project Activities

- Supercomputer Access

A three-year, 1.2 million dollar grant from the National Science Foundation has been awarded to fund MIDnet, a regional network that connects eight midwestern universities to the National Center for Supercomputer Applications (NCSA) at the University of Illinois, Champaign-Urbana and to NSFnet a national network that connects all five of the NSF sponsored supercomputer centers. Researchers at Washington University have interactive access to any of these five centers. Both the NCSA and the Pittsburg Supercomputer Center have solicited researchers at Washington University. A Proteon router brokers packet traffic between our local Ethernet-based network and the 56 Kbps MIDnet backbone.

- Network for Biomedical Research

A Shared-Instrument Grant from the Division of Research Resources has funded the installation of a network to provide high-speed communications within the broad community of biomedical investigators at Washington University. The shared facility, completed in late 1987, enables investigators to exchange scientific data and ideas throughout both university campuses. Principal components of the ethernet-based portion of network are: two CATV-based backbones, an intercampus ethernet via microwave, and distributed departmental baseband ethernets connected by LAN100 bridges. Preliminary experiments have demonstrated video transmission of images.

A CATV-based backbone was designed and installed on the hilltop campus. The cable plant was carefully tested using TDR to verify installed

cable lengths and sweep tested to measure and verify input and output signal levels. The results provide a basis for designing extensions and maintaining the cable plant. The intercampus 10-Mbps Ethernet channel and a full-duplex broadcast-quality video channel span a 2.5-mile line-of-sight distance and utilize 23-GHz microwave equipment. The medical-school-campus portion of the network utilizes a second ethernet channel on the existing MIR CATV-based backbone.

Principle efforts were expended in learning how to configure, measure, and manage a large distribute network which supports both TCP/IP and DECnet protocols and hosts a heterogenous collection of processors operating with a variety of operating systems. Network activity profiles or "signatures" have been gathered to provide a basis for measuring traffic growth as additional hosts join the network. Operational procedures were established to encourage appropriate system software configuration control for hosts joining the network.

- A Campus-Wide Software Library

While there are a great many benefits to networks of autonomous mini- and microcomputers, decentralized computing as it is practiced by most organizations suffers from a lack of software. Organizations typically have enough money to purchase machines but do not a budget for a rich collection of software. Consequently programmers and users are continually "reinventing the wheel" building programs that emulate the functions of commercially available software or writing programs that have been previously written by other programmers within and without the university community. If the average price of commercial software could be significantly reduced and if public-domain and quasi-commercial software could be more efficiently distributed, people would be encouraged to build their applications with more sophisticated tools. This is the motivation behind the Washington University Campus-Wide Software Library.

The library began operation in July, 1987. Our first significant action is a contract that ONC has negotiated with Digital Equipment Corporation that will allow users of VAX computers to pay a fixed annual fee, based on processor-size. In exchange for this annual fee the machine is granted a one-year license for a collection of twenty-five software products, including operating systems, network software, compilers, application development tools, databases and a smattering of office automation products. Over fifty systems participated in the first year of this program.

F-8. Evaluation and Characterization of the DATACOPY Reflectance Camera

Personnel: S. M. Moore, BCL and Medicine
G. K. Garg, BCL

Support: RR 01380

The Datacopy model 920 reflectance camera is used to capture images of opaque photographs and other similar objects. The camera operates at two different resolutions with the field of view determined by camera elevation above the object. The camera is interfaced to an IBM PC/AT with 1 Megabyte of memory and 60 Megabytes of disk storage. Connection to other stations is made via Ethernet.

Several sets of tests were run on the camera in order to characterize its features. The first test involved determining the best placement of the lamps to provide even illumination over the entire field of view. Repeated trials were used to determine optimal lamp placement, and the best placement yielded a standard deviation of 2% (on a range of 0 to 255). Illustrations of the proper placement of the lamps is provided in Working Note 80, "The Datacopy Digital Reflectance Camera." In addition to lamp placement, this working note provides other instructions which help explain the operation and improve the performance of the camera.

Additional experiments were performed to examine the gray-scale characteristics of the Datacopy camera. A target calibrated in optical density was used to test the linearity of the camera's response to light reflected by the target. The target has 12 areas with different optical densities. A plot of observed gray-scale value versus optical density indicates that the camera provides a linear repsonse for gray-scale values between 35 and 158. A target with more samples would be useful for a more complete evaluation.

Experiments were run to determine the Modulation Transfer Function (MTF) of the camera at three heights above the target: 250, 410, and 700 mm. Since we were not able to generate test images with different frequency content, we used a step function as a target and inferred the MTF from measurements involving that step. We captured an image of a step function and computed the Fourier Transform of a line through the image. This transform was compared to the transform of an ideal step function. We took the ratio of non-zero values of the transforms at different frequencies to get an estimate of the MTF. As would be expected, the MTF depends on the height of the camera above the target, but the shapes of the functions computed are similar for the three heights. We found the MTF is flattest (near 100%) for a short interval near the origin and then tails off to values in the 40-to-60% range as the frequency (line pairs per millimeter) increases.

A fuller explanation of the experiments can be found in Working Note 80. No attempt was made to provide corrections for the camera limitations.

F-9. MULTI: A Windowing System for Image Display

Personnel: R. E. Hermes, BCL
G. E. Christensen, BCL

Support: RR 01380

A software system consisting of image-manipulation and display tools integrated with an easy-to-use interface has been developed. MULTI is a multi-window image-presentation system which can display image data stored in most of the image formats frequently used in the Resource.

The user interface is composed of pop-up menus which offer the user a variety of options. The main menu offers a set of basic image window manipulation features such as create, pan, resize, move, shrink, zoom, and rotate. Options to execute UNIX commands, display a color bar, select an arbitrary color-look-up table, and to save the current display also exist. On-line help is also provided from the menu. Some menu options require more user input such as a "create window" option which prompts for the window size, image file name, and image data format type. Free text can be imposed anywhere on the display screen and is often used to create legends for windows. Users have found the ability to save the current display contents for later retrieval and manipulation as an essential tool. It allows users to compile a sequence of display presentations which can be rapidly recalled in any order for taking photographs or reviewing algorithm results with collaborators.

MULTI is implemented on a MASSCOMP Aurora display system using the MASSCOMP library of display utilities. MULTI is now being converted to use the X-system which will provide software and display portability to systems from other vendors.

VI. TRAINING ACTIVITIES AND SEMINARS

Training activities of the Biomedical Computer Laboratory are directed toward the goals of informing the local and national scientific communities about resource projects and facilities and of instructing a broad spectrum of people in the application of advanced computer-techniques to problems in clinical medicine and biological research. Training activities include the teaching of formal courses at the School of Medicine and the School of Engineering as well as supervision of graduate students by Laboratory staff. Both individual and small-group training about resource facilities are made available to the biomedical scientist. National workshops and symposia on topics of interest and importance to the resource and community are supported.

The bringing together of biomedical scientists, engineers, and computer scientists provides important cross-fertilization between disciplines. In these settings, students and staff find the need and opportunity to test the relevance of theory and the usefulness of technology in applications to real problems. Also, the biomedical scientists are aided in learning new techniques for acquiring useful information. To this end, some of the courses offered are addressed to biologists without strong technical backgrounds who want and need a below-the-surface appreciation of biomedical computing. Laboratory personnel also participate in regularly scheduled conferences in the clinical departments where both the biological and technological issues are examined.

Seminars and presentations relating to resource projects and applications are conducted by Laboratory staff as well as scientists and engineers from the national community. During the year the following activities were supported:

Seminars

"Videodisc Recording/Authoring System" Demonstration July 29, 1987	Dr. Michael C. Moore Edudisc Nashville, TN
"Entropy, Markov Random Fields, and Constrained Optimization: Applications to Image Processing" October 9, 1987	Dr. Michael I. Miller Institute for Biomedical Computing Washington University St. Louis, MO

"Demonstration of Photometrics Charge-Coupled Device for Image Acquisition"

December 8, 1987

Mr. Tim Bruchman
Photometrics, Ltd.
Tuscon, AZ

"Summary of the Medical Imaging II Conference"

February 22, 1988

Mr. Evren Senol
Department of Electrical Engineering
Washington University
St. Louis, MO

"Direct Image Acquisition of Electrophoretic Gels with Photometrics Charge-Coupled Device"

April 14, 1988

Ms. Heather Drury
Biomedical Computer Laboratory
Washington University
St. Louis, MO

"Modeling Electrophoretic Mobility and Band Shape"

April 21, 1988

Mr. William S. Gee
Mallinckrodt Institute of Radiology
Washington University
St. Louis, MO

VII. PUBLICATIONS AND ORAL PRESENTATIONS

Abendschein, D. R., Fontanet, H. L., Markham, J., and Sobel, B. E., "Physiologic Modelling of MM Creatine Kinase Isoforms," in Mathematical Modelling in Science and Technology, E. Y. Rodin and X. J. R. Avula, eds., Sixth International Conference Proceedings, Great Britain, Pergamon Press, 11:621-625, 1988.

Abendschein, D. R., Fox, K. A. A., Ambos, H., D., Sobel, B. E., and Bergmann, S. R., "Metabolism of Beta-Methyl [1-^{11}C] Heptadecanoic Acid in Canine Myocardium," International Journal of Radiation Applications, Part B, Nuclear Medicine and Biology, 14:579-585, 1987.

Abendschein, D. R., Seacord, L. M., Nohara, R., Sobel, B. E., and Jaffe, A. S., "Prompt Detection of Myocardial Injury by Assay of Creatine Kinase Isoforms in Initial Plasma Samples," Clinical Cardiology, in press.

Abendschein, D. R., Serota, H., Plummer, Jr., T. H., Amiraian, K., Strauss, A. W., Sobel, B. E., and Jaffe, A. S., "Conversion of MM Creatine Kinase Isoforms in Human Plasma by Carboxypeptidase N," Journal of Laboratory and Clinical Medicine, 110:798-806, 1987.

Arthur, R. M., and Broadstone, S. R., "The Effect of Background Velocity Variation on the Point-Spread Function of Ultrasonic Transducer Arrays," 1987 Ultrasonics Symposium Proceedings, IEEE Catalog No. 87CH2492-7, 2:947-950, 1987.

Bergmann, S. R., Myears, D. W., Walsh, M. N., Weinheimer, C. J., Geltman, E. M., Markham, J., and Herrero, P., "Quantitation of Myocardial Blood Flow with $H_2{}^{15}O$ and Positron Emission Tomography (PET)," Circulation, 76:IV-116, 1987 (abstract).

Blaine, G. J., "PACS Developments at Mallinckrodt Institute of Radiology," presented at the Topical Symposium on Digital Radiography and PACS, American Association of Physicists in Medicine, New Orleans, LA, April 23, 1988.

Blaine, G. J., Hill, R. L., Rueter, A. P., Senol, E., and Studt, J. W., "Image Transmission Studies," Proceedings of SPIE, vol. 914 (part B), Medical Imaging II: Image Data Management and Display, Newport Beach, CA, pp. 953-960, January 31-February 5, 1988.

Boineau, J. P., Canavan, T. E., Schuessler, R. B., Cain, M. E., Corr, P. B., and Cox, J. L., "Demonstration of a Widely Distributed Atrial Pacemaker Complex in the Human Heart," Circulation, in press.

Broadstone, S. R., and Arthur, R. M., "Time-of-Flight Approximation for Medical Ultrasonic Imaging," Acoustical Imaging, in press.

Brown, M. A., Marshall, D. R., Sobel, B. E., and Bergmann, S. R., "Delineation of Myocardial Oxygen Utilization with Carbon-11 Labeled Acetate," Circulation, 76:687-696, 1987.

Brown, M. A., Myears, D. W., and Bergmann, S. R., "Noninvasive Assessment of Canine Myocardial Oxidative Metabolism with ^{11}C-Acetate and Positron Emission Tomograpny," Journal of the American College of Cardiology, in press.

Brown, M. A., Myears, D. W., Herrero, P., and Bergmann, S. R., "Disparity Between Oxidative and Fatty Acid Metabolism in Reperfused Myocardium Assessed with Positron Emission Tomography," Circulation, 76:IV-4, 1987 (abstract).

Brown, M. A., Walsh, M. N., Weinheimer, C. J., Geltman, E. M., Sobel, B. E., and Bergmann, S. R., "Assessment of Regional Oxidative Metabolism by Positron Tomography with C-11-Acetate in Patients with Myocardial Infarction," Journal of Nuclear Medicine, 29:818, 1988 (abstract).

Canavan, T. E., Schuessler, R. B., Boineau, J. P., Corr, P. B., Cain, M. E., and Cox, J. L., "Simultaneous Global Epicardial Activation Mapping During Atrial Fibrillation in Patients with Wolff-Parkinson-White Syndrome," Journal of Thoracic and Cardiovascular Surgery, in press.

Canavan, T. E., Schuessler, R. B., Boineau, P., Corr, P. B., Cain, M. E., and Cox, J. L., "Simultaneous 156-Point Activation Mapping During Induced Atrial Fibrillation in Patients with Wolff-Parkinson-White Syndrome," Circulation, 76:IV-138, 1987 (abstract).

Canavan, T. E., Schuessler, R. B., Cain, M. E., Lindsay, B. D., Boineau, J. P., Corr, P. B., and Cox, J. L., "Computerized Global Electrophysiologic Mapping of the Atrium in a Patient with Multiple Supraventricular Tachyarrhythmias," Annals of Thoracic Surgery, in press.

Corr, P. B., and Dobmeyer, D. J., "Amphiphathic Lipid Metabolites and Arrhythmogenesis: A Perspective," in Lethal Arrhythmias Resulting from Myocardial Ischemia and Infarction, M. Rosen and Y. Palti, eds., in press.

Corr, P. B., Pitt, B., Natelson, B. H., Reis, D. J., Shine, K. I., and Skinner, J. E., "Task Force 3: Sudden Cardiac Death. Neural-Chemical Interactions," Circulation, 76:I-208-I-214, 1987.

Corr, P. B., Saffitz, J. E., and Sobel, B. E., "Lysophospholipids, Long Chain Acylcarnitines and Membrane Dysfunction in the Ischemic Heart," in Lipid Alterations in the Normoxic and Ischaemic Heart, H. Stam, G. J. van der Vusse, eds., Springer-Verlag, New York, pp. 199-208, 1987.

Corr, P. B., Saffitz, J. E., and Sobel, B. E., "What Is the Contribution of Altered Lipid Metabolism to Arrhythmogenesis in the Ischemic Heart?" in Life-Threatening Arrhythmias During Ischemia and Infarction, D. J. Hearse, A. S. Manning, and M. J. Janse, eds., Raven Press, New York, 91-114, 1987.

Corr, P. B., Yamada, K. A., Creer, M., Sharma, A. D., and Sobel, B. E., "Lysophosphoglycerides and Ventricular Fibrillation Early after Onset of Ischemia," Journal of Molecular and Cellular Cardiology, 19:45-53, 1987.

Cox, J. R., "Recollections on the Processing of Biomedical Signals," Proceedings of the ACM Conference on the History of Medical Informatics, Washington, D.C., November 1987, in press.

Cox, J. R., Jost, R. G., Monsees, T., Ramamurthy, S., and Karlsson, M., "An Inexpensive Electronic Viewbox," Proceedings of the SPIE Medical Imaging II Conference, Newport Beach, CA, pp. 1218-1224, January 31-February 5, 1988.

Creer, M. H., Sobel, B. E., Saffitz, J. E., Pogwizd, S. M., and Corr, P. B., "Prevention of Accumulation of Acylcarnitine, Lysophatides and Ventricular Fibrillation by Inhibition of Carnitine Acyltransferase I in Ischemic Heart," Circulation, 76:IV-111, 1987 (abstract).

Eisenberg, J. D., Sobel, B. E., and Geltman, E. M., "Differentiation of Ischemic from Nonischemic Cardiomyopathy and Positron Emission Tomography," American Journal of Cardiology, 59:1410-1416, 1987.

Fields, L. E., Daugherty, A., and Bergmann, S. R., "Effect of Fatty Acid on Performance and Lipid Content of Hearts from Diabetic Rabbits," American Journal of Physiology: Heart and Circulatory Physiology, 250:H1079-1085, 1986.

Fuhrmann, D. R., "An Algorithm for Subspace Computation, with Applications in Signal Processing," SIAM Journal of Matrix Analysis and Applications, 9:213, April 1988.

Fuhrmann, D. R., "Quadtree Traversal Algorithms for Pointer-Based and Depth-First Representations," IEEE Transactions on Pattern Analysis and Machine Intelligence, in press.

Fuhrmann, D. R., Brown, M. A., Miller, M. I., Roysam, B., Saffitz, J. E., and Thomas, Jr., L. J., "Data Acquisition System for Maximum-Likelihood Analysis of Electron Microscopic Autoradiographs," Journal of Electron Microscopy Technique, 7(3):199-204, 1987.

Fuhrmann, D. R., Turmon, M. J., and Miller, M. I., "Efficient Implementation of the EM Algorithm for Toeplitz Covariance Estimation," Proceedings of the Twenty-Second Annual Conference on Information Sciences and System, Princeton University, Princeton, NJ, p. 177, March 1988.

Geltman, E. M., "Assessment of Myocardial Metabolism and Perfusion with Positron Emission Tomography," Cardiology, pp. 77-110, November 1987.

Green, M. A., Welch, M. J., Mathias, C. J., Shelton, M. E., and Bergmann, S. R., "Validation of Potential Cerebral and Myocardial Blood Flow Tracers: Single-Pass Studies of Copper BIS (Thiosemicarbazones)," Journal of Nuclear Medicine, 29:848, 1988 (abstract).

Hart, Jr., W. M., "Acquired Dyschromatopsias," Survey of Ophthalmology, 32:10-31, 1987.

Hart, Jr., W. M., Trick, G., Nesher, R., and Gordon, M., "The Effect of Glaucomatous Damage on Static Perimetric Thresholds Determined with

Luminance Increment and Blue/Yellow Color Increment Thresholds," Investigative Ophthalmology and Visual Science," (supplement) 29:422, 1988 (abstract).

Heathers, G. P., Corr, P. B., and Evers, A. S., "A Novel Method for Measurement Mass of Inositol Phosphates in Adult Canine Myocytes," Circulation, 76:IV-13, 1987 (abstract).

Heathers, G. P., Yamada, K. A., Kanter, E. M., and Corr, P. B., "Long-Chain Acylcarnitines Mediate the Hypoxia Induced Increase in $Alpha_1$-Adrenergic Receptors on Adult Canine Myocytes," Circulation Research, 61:735-746, 1987.

Heathers, G. P., Yamada, K. A., Pogwizd, S. M., and Corr, P. B., "The Contribution of α- and β-Adrenergic Mechanisms in the Genesis of Arrhythmias During Myocardial Ischemia and Reperfusion," in Neurocardiology, H. E. Kulbertus and G. Franck, eds., Futura Publishing, New York, pp. 143-178, 1988.

Hermes, R. E., and Blaine, G. J., "Performance Assessment of a Campus-Wide Network: Initial Observations," presented at the Digital Equipment Corporation Users Group meeting (DECUS), Anaheim, CA, December 7-11, 1987.

Herrero, P., Markham, J., Myears, D. W., Weinheimer, C. J., and Bergmann, S. R., "Measurement of Myocardial Blood Flow with Positron Emission Tomography: Correction for Count Spillover and Partial Volume Effects," in Mathematical Modelling in Science and Technology, E. Y. Rodin and X. J. R. Avula, eds., Sixth International Conference Proceedings, Pergamon Press, Great Britian, 11:807-812, 1988.

Jaffe, A. S., Biello, D. R., Sobel, B. E., and Geltman, E.M., "Enhancement of Metabolism of Jeopardized Myocardium by Nifedipine," International Journal of Cardiology, 15:77-89, 1987.

Karamanos, N. A., "A New Method for Analyzing Auditory-Nerve Discharge Patterns," Department of Electrical Engineering, Sever Institute of Technology, Washington University, St. Louis, MO, December 1987 (Master of Science Thesis).

Karamanos, N., and Miller, M. I., "A New Method for Estimating Stimulus Related and Recovery Related Components in Auditory-Nerve Discharges," presented at the 8th International Symposium on Hearing, "Basic Issues in Hearing," Groningen, The Netherlands, April 9, 1988.

Knabb, R. M., Bergmann, S. R., Fox, K. A. A., and Sobel, B. E., "The Temporal Pattern of Recovery of Myocardial Perfusion and Metabolism Delineated by Positron Emission Tomography after Coronary Thrombolysis," Journal of Nuclear Medicine, 28:1563-1570, 1987.

Larson, K. B., "Physical and Mathematical Principles of Tracer Kinetics in Biological Applications," seminar presented to Washington University Three-Two Program students, St. Louis, MO, January 18, 1988.

Larson, K. B., "Tracer Kinetics for Dynamic Stuydies Using Externally Detected Radiotracers," lecture series for Radiation Sciences - Neurology Research Staff, Mallinckrodt Institute of Radiology, Washington University School of Medicine, St. Louis, MO, November 13, 1987 - April 29, 1988.

Larson, K. B., Markham, J., and Raichle, M. E., "Tracer-Kinetic Models for Measuring Cerebral-Blood Flow Using Externally Detected Radiotracers," Journal of Cerebral Blood Flow and Metabolism, 7:443-463, 1987.

Lerch, R. A., and Bergmann, S. R., "Non-Invasive Assessment of Myocardial Fatty Acid Metabolism with Positron Emission Tomography and Gamma Imaging," in New Concepts in Cardiac Imaging 1988, J. L. Ritchie, ed., Year Book Medical Publishers, Chicago, IL, pp. 91-116, 1988.

Lindsay, B. D., Ambos, H. D., Schechtman, K. B., and Cain, M. E., "Improved Differentiation of Patients with and Without Ventricular Tachycardia by Frequency Analysis of Multiple ECG Leads," in press.

Lindsay, B. D., Markham, J., Schechtman, K. B., Ambos, H. D., and Cain, M. E., "Identification of Patients with Sustained Ventricular Tachycardia by Frequency Analysis of Signal-Averaged Electrocardiograms Despite the Presence of Bundle Branch Block," Circulation, 77(1):122-130, 1988.

Madaras, E. I., Perez, J., Sobel, B. E., Mottley, J. G., and Miller, J. G., "Anisotropy of the Ultrasonic Backscatter of Myocardial Tissue: II. Measurements in Vivo," Journal of the Acoustical Society of America, 83:762-769, 1988.

Miller, M. I., Roysam, B., and Smith, K. R., "Mapping Rule-based and Stochastic Constraints to Connection Architectures: Implication for Hierarchical Image Processing," accepted for presentation at the Visual Communications and Image Processing 1988 SPIE Conference, Cambridge, MA, November 1988.

Mohr, G. A., Vered, Z., Barzilai, B., Perez, J. E., Sobel, B. E., and Miller, J. G., "An Algorithm for the Automated Determination of the Magnitude and Time Delay ("Phase") of the Cyclic Variation of Ultrasonic Backscatter from Myocardium," Ultrasonic Imaging, 1988 (abstract), in press.

Mottley, J. G., and Miller, J. G., "Anisotropy of the Ultrasonic Backscatter of Myocardial Tissue: I. Theory and Measurements in Vitro," Journal of the Acoustical Society of America, 83:755-761, 1988.

Myears, D. W., Nohara, R., Abendschein, D. R., Saffitz, J. E., Sobel, B. E., and Bergmann, S. R., "Compromise of Beneficial Effects of Reperfusion on Myocardium Supplied by Vessels with Critical Residual Stenosis," Journal of the American College of Cardiology, 11:1078-1086, 1988.

Myears, D. W., Nohara, R., Saffitz, J. E., Abendschein, D. R., and Bergmann, S. R., "Adequate Reperfusion Despite Residual Critical Coronary Stenosis," Circulation, 76:IV-20, 1987 (abstract).

Myears, D. W., Sobel, B. E., and Bergmann, S. R., "Substrate Use in Ischemic and Reperfused Canine Myocardium: Quantitative Considerations," American Journal of Physiology (Heart and Circulatory Physiology), 253:H107-H114, 1987.

Nohara, R., Abendschein, D. R., and Bergmann, S. R., "Limitation of Coronary Flow Reserve: Relationship to Degree of Coronary Arterial Narrowing," The FASEB Journal, 2:A1709, 1988 (abstract).

Nohara, R., Sobel, B. E., Jaffe, A. S., and Abendschein, D. R., "Quantitative Analysis of Isoforms of Creatine Kinase MM in Plasma by Chromatofocusing with On-Line Monitoring of Enzyme Activity," Clinical Chemistry, 34:235-239, 1988.

Pogwizd, S. M., and Corr, P. B, "Electrophysiologic Mechanisms Underlying Arrhythmias Due to Reperfusion of Ischemic Myocardium," Circulation, 76:404-426, 1987.

Pogwizd, S. M., and Corr, P. B., "Mechanisms Contributing to Arrhythmogenesis During Early Myocardial Ischemia, Subsequent Reperfusion and Chronic Infarction," Angiology, in press.

Pogwizd, S. M., and Corr, P. B., "Reentrant and Non-reentrant Mechanisms Contribute to Arrhythmogenesis During Early Myocardial Ischemia: Results Using Three-Dimensional Mapping," Circulation Research, 61:352-371, 1987.

Pogwizd, S. M., Moore, S. M., and Corr, P. B., "Mechanisms Responsible for the Transition to Ventricular Fibrillation During Ischemia," Circulation, 76:IV-114, 1987 (abstract).

Politte, D. G., and Snyder, D. L., "The Use of Constraints to Eliminate Artifacts in Maximum-Likelihood Image Estimation for Emission Tomography," IEEE Transactions on Nuclear Science, NS-35:608-610, February 1988.

Purdy, J. A., Wong, J. W., and Harms, W. B., "Treatment Planning Computers (Present and Future)," in Radiation Oncology Physics - 1986, J. G. Kereiakes, H. R. Elson, and C. G. Born, eds., American Institute of Physics, pp. 495-511, 1987.

Rosamond, T. L., Abendschein, D. R., Sobel, B. E., Bergmann, S. R., and Fox, K. A. A., "Metabolic Fate of Radiolabeled Palmitate in Ischemic Canine Myocardium: Implications for Positron Emission Tomography," Journal of Nuclear Medicine, 28:1322-1329, 1987.

Roysam, B., "The Maximum-Likelihood Method for EM Autoradiography: Evaluation and Comparison to Crossfire-Analysis," in Proceedings of the 46th Annual Meeting of the Electron Microscopy Society of America, G. W. Bailey, ed., San Francisco Press, San Francisco, CA, pp. 844-845, 1988.

Roysam, B., "The Maximum-Likelihood Method for EM Autoradiography: Small-System Implementation Technique," in Proceedings of the 46th Annual Meeting of the Electron Microscopy Society of America, G. W. Bailey, ed., San Francisco Press, San Francisco, CA, pp. 424-425, 1988.

Roysam, B., and Miller, M. I., "Mapping Deterministic Rules to Stochastic Representations via Gibbs' Distributions on Massively Parallel Analog Networks: Application to Global Optimization," Proceedings of the 1988 Connectionists Models Summer School, Carnegie Mellon University, Pittsburgh, PA, June 17-26, 1988, in press.

Roysam, B., Shrauner, J. A., and Miller, M. I., "Bayesian Imaging Using Good's Roughness Measure - Implementation on a Massively Parallel Processor," International Conference on Acoustics, Speech, and Signal Processing, New York, NY, 2:932, April 1988 (abstract).

Seacord, L. M., Abendschein, D. R., Nohara, R., Hartzler, G., Sobel, B. E., and Jaffe, A. S., "Detection of Reperfusion Within One Hour after Coronary Recanalization by Analysis of Isoforms of the MM Creatine Kinase Isoenzyme in Plasma," Fibrinolysis, 2:151-156, 1988.

Seacord, L. M., and Jaffe, A. S., "Early Diagnosis and Detection of Reperfusion with Isoform of Creatine Kinase," in Acute Coronary Care in the Thrombolytic Era, G. Wagner, ed., in press.

Schuessler, R. B., Canavan, T. E., Boineau, P., Corr, P. B., Cain, M. E., and Cox, J. L., "Human Atrial Activation Mapping Demonstrates Multicentric Impulse Origin: The Human Pacemaker Complex," Circulation, 76:IV-176, 1987 (abstract).

Shelton, M. E., Welch, M. J., Dence, C. S., Hwang, D.-R., and Bergmann, S. R. "[F-18] Fluoromisonidazole: A Potential Marker of Salvageable Myocardium," Journal of Nuclear Medicine, 29-807, 1988 (abstract).

Shipton, H. W., "Recording Technology," chapter in Clinical Electroencephalography, 2nd edition, D. Daly, ed., Raven Press, NY, in press.

Smith, K. R., "Spherical PET Studies," presented to the ESSRL Group at Washington University, St. Louis, MO, November 18, 1987.

Snyder, D. L., Miller, M. I., and Schulz, T. J., "Constrained Probability-Density Estimation from Noisy Data," Proceedings of the Twenty-Second Annual Conference on Information Sciences and System, Princeton University, Princeton, NJ, pp. 170-172, March 1988.

Thomas, Jr., L. J., "Computers, Cardiologists and Cardiograms," seminar presented to Washington University Three-Two Program students, St. Louis, MO, January 5, 1988.

Tilton, R. G., Cole, P. A., Zions, J. D., Daugherty, A., Larson, K. B., Sutera, S. P., Kilo, C., and Williamson, J. R., "Increased Ischemia-Reperfusion Injury to the Heart Associated with Short-Term, Diet-Induced Hypercholesterolemia," Circulation Research, 60:551-559, 1987.

Vered, Z., Barzilai, B., Mohr, G. A., Thomas, III, L. J., Perez, J. E., Sobel, B. E., and Miller, J. G., "Real-Time Two-Dimensional Imaging Based

on Radio Frequency Derived Integrated Backscatter in Normal Volunteers and Patients," Ultrasonic Imaging, 9:51, 1987 (abstract).

Vered, Z., Barzilai, B., Mohr, G. A., Thomas III, L. J., Sobel, B. E., Shoup, T. A., Melton, H. E., Miller, J. G., and Perez, J. E., "Quantitative Ultrasonic Tissue Characterization with Real-Time Integrated Backscatter Imaging in Normal Human Subjects and in Patients with Dilated Cardiomyopathy," Circulation, 76:1067-1073, 1987.

Walsh, M. N., Bergmann, S. R., Baird, T. R., Schaab, C. M., Sobel, B. E., and Geltman, E. M., "Improved Myocardial Perfusion after Angioplasty Delineated by Positron Emission Tomography and $H_2{}^{15}O$," Circulation, 76:IV-401, 1987 (abstract).

Walsh, M. N., Bergmann, S. R., Steele, R. L., Kenzora, J. L., Ter-Pogossian, M. M., Sobel, B. E., and Geltman, E. M., "Delineation of Impaired Regional Myocardial Perfusion by Positron Emission Tomography with $H_2{}^{15}O$," Circulation, in press.

Walsh, M. N., Bergmann, S. R., Ter-Pogossian, M. M., Sobel, B. E., and Geltman, E. M., "Identification of Patients with Coronary Artery Disease by Positron Tomography with $H_2{}^{15}O$," Circulation, in press.

Walsh, M. N., Herrero, P., Steele, R. L., Geltman, E. M., Sobel, B. E., and Bergmann, S. R., "Quantitative Delineation of Diminished Resting Myocardial Perfusion in Patients with Critical Coronary Stenosis Assessed with Positron Emission Tomography and $H_2{}^{15}O$," Journal of the American College of Cardiology, 11:152A, 1988 (abstract).

Walsh, M. N., Serota, H., Bergmann, S. R., Sobel, B. E., and Geltman, B. E., "Assessment of Relative Coronary Flow Reserve with Dynamic Positron Emission Tomography and $H_2{}^{15}O$," Journal of the American College of Cardiology, 9:160A, 1987 (abstract).

Wear, K. A., Milunski, M. R., Wickline, S. A., Perez, J. E., Sobel, B. E., and Miller, J. G., "Discrimination Between Acutely Ischemic Myocardium and Remote Infarct in Dogs on the Basis of Frequency Dependent Backscatter," Ultrasonic Imaging, 1988, in press (abstract).

Winslow, R. L., "Effects of Electrical Stimulation of the COCB on Auditory-Nerve Rate Responses to Tones in Noise," Abstracts of the 11th Midwinter Research Meeting, Association for Research in Otorhinolaryngology, p. 135, 1988 (abstract).

Winslow, R. L., Miller, R. F., and Ogden, T. E., "The Functional Role of Dendritic Spines in the Retinal Horizontal Cell Network," Investigative Ophthalmology and Visual Science, 29:297, 1988 (abstract).

Winslow, R. L., Miller, R. F., and Ogden, T. E., "The Functional Role of Spines in the Retinal Horizontal Cell Network," Proceedings of the National Academy of Sciences, USA, in press.

Winslow, R. L., and Sachs, M. B., "Single-Tone Intensity Discrimination Based on Auditory-Nerve Rate Responses in Backgrounds of Quiet, Noise, and with Stimulation of the Crossed Olivocochlear Bundle," Hearing Research, in press.

Wong, J. W., Slessinger, E. D., Hermes, R. E., Harms, W. B., Vannier, M. W., and Roy, T., "Investigation of an Approach to Quantitative Treatment Verification," Proceedings of the 9th International Conference on the Use of Computers in Radiation Therapy, Tilburg, The Netherlands, North Holland, The Netherlands, pp. 461-464, June 22-25, 1987.

Yamada, K. A., Heathers, G. P., Pogwizd, S. M., and Corr, P. B., "Sympathetic Influences on Arrhythmogenesis in the Ischemic Heart," in Heart and Brain, Brain and Heart, Springer-Verlag, New York, NY, in press.

Yamada, K. A., Saffitz, J. E., Sobel, B. E., Lange, L. G., and Corr, P. B., "Protective Effects of Alpha-Adrenergic Blockade on Feline Myocardium Subjected to Ischemia and Reperfusion," Journal of Clinical Investigation, in press.

VIII. MONOGRAPHS AND WORKING NOTES

The Biomedical Computer Laboratory's Monograph Series was established to systematize the many reports, reprints, program descriptions, and other documents written at BCL or supported in part by the Laboratory's facilities or staff.

A forum, much less formal than our monograph series, has been instituted to serve as a repository for materials such as: research notes, system and component documentation, technical survey notes and prepublication drafts. Working note files are maintained for access by anyone associated with the Institute for Biomedical Computing. Distribution for outside use can be made available with the consent of the contributing author.

Monographs

Following is a list of the monographs published by BCL during the past year. Copies of the complete index to the monograph series are available on request.

Monograph Number	Author(s)	Title	Date
482	Roysam, B.	A New Method for EM Auto-radiography: Validation and Comparison to Crossfire-Analysis	5/87
483	Miller, M. I. Roysam, B. Saffitz, J. E. Larson, K. B. Fuhrmann, D. Thomas, Jr., L. J.	A New Method for the Analysis of Electron Microscopic Autoradiographs	7/87
484	Smith, K. R.	Mapping the EM Algorithm for Time-of-Flight Positron Emission Tomography onto Parallel Architectures	7/87
485	Liu, S. K.	Efficient Computation of the EM Algorithm in Time-of-Flight Positron-Emission Tomography	7/87
486	Miller, M. I.	Strategies for the Representation of Broadband Stimuli in the Discharge Patterns of Auditory-Nerve Fibers	6/86
487	Miller, M. I. Barta, P. E. Sachs, M. B.	Strategies for the Representation of a Tone in Background Noise in the Temporal Aspects of the Discharge Patterns of Auditory-Nerve Fibers	3/87

Monograph Number	Author(s)	Title	Date
488	Larson, K. B. Markham, J. Raichle, M. E.	Tracer-Kinetic Models for Measuring Cerebral Blood Flow Using Externally Detected Radiotracers	3/87
489	Politte, D. G. Snyder, D. L.	The Use of Constraints to Eliminate Artifacts in Maximum-Likelihood Image Estimation for Emission Tomography	10/87
490	Ollinger, J. M.	Estimation Algorithms for Dynamic Tracer Studies Using Positron-Emission Tomography	6/87
491	Miller, M. I. Snyder, D. L.	The Role of Likelihood and Entropy in Incomplete-Data Problems: Applications to Estimating Point-Process Intensities and Toeplitz Constrained Covariances	7/87
492	Mead, C. N. Clark, K. W. Thomas, Jr., L. J.	An Annotated Clinical-Event Data-base for Evaluation of Ambulatory ECG-Analysis Systems	10/86
493	Fuhrmann, D. R. Brown, M. A. Miller, M. I. Roysam, B. Saffitz, J. E. Thomas, Jr., L. J.	Data Acquisition System for Maximum-Likelihood Analysis of Electron Microscopic Autoradiographs	5/87
494	Johnston, P. H.	Phase-Insensitive Detection and the Method of Moments for Ultrasonic Tissue Characterization	8/85
495	Broadstone, S. R.	Ultrasonic Reflection Tomography: An Off-Line, High Resolution Imaging System for Tissue Characterization	5/86
496	Tilton, R. G. Cole, P. A. Zions, J. D. Daugherty, A. Larson, K. B. Sutera, S. P. Kilo, C. Williamson, J. R.	Increased Ischemia-Reperfusion Injury to the Heart Associated with Short-Term, Diet-Induced Hypercholesterolemia in Rabbits	12/86

Monograph Number	Author(s)	Title	Date
497	Broadstone, S. R. Arthur, R. M.	An Approach to Real-Time Reflection Tomography Using the Complete Dataset	10/86
498	Rosenberger, F. Krippner, K. Stein, Jr., D. Wong, J.	Implementation of the Delta-Volume Dose Calculation Algorithm	9/84
499	Toga, A. W. Arnicar, T. L.	Image Analysis of Brain Physiology	12/85
500	Johnston, P. H. Miller, J. G.	A Comparison of Backscatter Measured by Phase-Sensitive and Phase-Insensitive Detection	1985
501	Wickline, S. A. Thomas, III, L. J. Miller, J. G. Sobel, B. E. Perez, J. E.	Sensitive Detection of the Effects of Reperfusion on Myocardium by Ultrasonic Tissue Characterization with Integrated Backscatter	4/86
502	Johnston, P. H. Miller, J. G.	Phase-Insensitive Detection for Measurement of Backscattered Ultrasound	2/86
503	Karamanos, N. A.	A New Method for Analyzing Auditory-Nerve Discharge Patterns	12/87
504	Skinner, B. Winslow, R. L.	Computing Depth Information from Stereo Image Pairs Using the Marr-Poggio Stereo Algorithm	5/87
505	McCarthy, A. Barrett, R. Miller, M. I.	Systolic Implementation of the EM Algorithm for Emission Tomography on Mesh-Connected Processors	3/88
506	Roysam, B. Shrauner, J. A. Miller, M. I.	Bayesian Imaging Using Good's Roughness Measure - Implementation on a Massively Parallel Processor	4/88

Working Notes

Following is an index of notes submitted during the current reporting period.

Working Note Number	Author(s)	Title	Date
77	Smith, K. R.	Preliminary Study of Three-Dimensional Image Reconstruction for Spherical Baby PET	3/87
78	Smith, K. R.	Spherical PET EM Algorithm Derivation	4/87
79	Smith, K. R.	Compton Scatter - A Closer Look	6/87
80	Garg, G. Moore, S.	The Datacopy Digital Reflectance Camera	5/88
81	Politte, D. G. Hoffman, G. R.	Reduced-Angle Image-Reconstruction for Super PETT II	6/88
82	Politte, D. G.	Constrained Maximum-Likelihood Image Estimation for Time-of-Flight PET via the EM Algorithm Implemented in a Rotated Coordinate System	6/88